
Intensity fluctuation spectroscopy with coherent X-rays

Eric Dufresne

Centre for the Physics of Materials
Department of Physics, McGill University
Montréal, Québec, Canada

A Thesis submitted to the
Faculty of Graduate Studies and Research
in partial fulfillment of the requirements for the degree of
Doctor of Philosophy

© Eric Dufresne, 1995

CONTENTS

LIST OF COMMON SYMBOLS	vii
RÉSUMÉ	viii
ABSTRACT	ix
ACKNOWLEDGMENTS	x
1 INTRODUCTION	1
2 COHERENT X-RAYS	7
2.1 Definitions of coherence	7
2.2 Properties of synchrotron radiation	9
2.3 X-ray scattering	11
2.4 X-ray scattering from Cu ₃ Au	15
2.5 Production of coherent X-rays: experimental method	19
2.5.1 Coherence volume	23
2.6 Structure factor with coherent X-rays	24
2.6.1 Coherent X-ray scattering for the study of isolated defects or artificially made structures	25
2.6.2 Scattering from a binary alloy in equilibrium	28
3 CHARACTERIZATION OF POSITION-SENSITIVE DETECTORS	40
3.0.3 Description of the technique	41
3.0.4 Characterization of a linear PSD	48
3.0.5 Characterization of a CCD array	53
3.0.6 Discussion	61
4 EXPERIMENTAL METHOD	63
4.1 Beamline characterization and optics	63
4.2 Sample preparation and sample furnace	65
4.3 Scattering geometry	66
4.4 Data treatment	67
4.5 Pinhole construction	68
4.6 Demonstration of coherence: Fraunhofer diffraction pattern of a pinhole.	69
4.7 Incident X-ray beam structure and stability	72
4.8 Temperature calibration and heat treatment	75
4.9 Setting the angle of incidence θ_i	76

5	RESULTS	78
5.1	Static speckle patterns	78
5.1.1	Measuring speckle size	83
5.1.2	Contrast	92
5.2	Ordering kinetics of an order-disorder phase transition	94
5.2.1	Numerical Simulations of model A	110
6	CONCLUSIONS	118
	APPENDICES	124
A.1	Some useful probability distributions	124
A.2	Error analysis	125
A.2.1	Uncertainty in the measured mean and variance	126
A.2.2	Correlation of the sample mean and variance	127
A.2.3	Evaluation of the error on a function of S^2 and $\langle x \rangle$	128
A.2.4	Including electronic noise for an X-ray detector	128
A.3	Derivation of the autocorrelation function for a Gaussian	130
A.4	Tools for time fluctuations analysis	130
	REFERENCES	133

FIGURES AND TABLES

FIGURES

2.1	Fraunhofer and Bragg condition	12
2.2	An order-disorder transition	16
2.3	Superlattice anisotropy	18
2.4	The experimental setup.	20
2.5	Energy dependence of scattering in Cu_3Au	23
2.6	Longitudinal coherence condition.	24
2.7	Structure factor of an edge dislocation	26
2.8	Structure factor with coherent illumination.	31
2.9	A slice of Fig 2.8.	32
2.10	The scattering amplitude for speckle	33
2.11	IFS on model A.	35
2.12	Probability density of $S(\vec{q})$	36
2.13	The statistic of the time-averaged intensity.	38
3.1	Ratio of variance over mean	50
3.2	Spatial correlation function $C(i, \Delta)$	51
3.3	Detector calibration setup	54
3.4	Ratio of variance over mean for CCD	55
3.5	Detector calibration curve	55
3.6	Variance of the linearized signal	56
3.7	Spatial uniformity of the row or column average	57
3.8	Time averaged variance	58
3.9	Slices of the time averaged variance	59
3.10	The spatial correlation function for the CCD	60
4.1	The X-ray oven	65
4.2	The scattering geometry	67
4.3	The CCD calibration at CHESS and X25	68
4.4	Fraunhofer diffraction patterns of a $7.5 \mu\text{m}$ pinhole along $2\Theta_{\parallel}$ and $2\Theta_{\perp}$	70
4.5	Fraunhofer diffraction measured with a CCD	73
4.6	Time fluctuations of the incident beam at X25	74
4.7	Horizontal and vertical structure of the incident beam at X25	75
4.8	Square of the order parameter versus temperature, and the quench profile for a typical quench	76
5.1	A typical static speckle pattern from Cu_3Au (100)	79
5.2	Speckle patterns dependence on X-ray optics.	82

5.3	Autocorrelation function for Cu ₃ Au (100)	84
5.4	Slices of $\Gamma(\vec{\Delta}q, t, 0)$	85
5.5	The detector crosscorrelation	86
5.6	Comparison of Eq. 5.7 and Eq. 5.8	87
5.7	The speckle size for different optical conditions	89
5.8	Variations of the correlation function maximum with pinhole diameter	90
5.9	The contrast for different optical conditions	93
5.10	$S(\vec{q}, t)$ for three different times in run 21	95
5.11	Slices of $S(\vec{q}, t)$ along $2\theta_{\perp}$ and $2\theta_{\parallel}$ in Fig. 5.10	97
5.12	Fit parameters for the data collected at X25 and CHESS	98
5.13	Time evolution of a single row of the CCD for run 21	101
5.14	Time evolution of a single row of the CCD for run 22 at $T = 300$ K .	102
5.15	Time series for run 24.	104
5.16	Time series for run 113 at CHESS	105
5.17	$S(\vec{q}, t)$ vs t for run 21	107
5.18	$S(\vec{q}, t)$ vs t for run 22	108
5.19	$S(\vec{q}, t)$ for three different times after the quench.	111
5.20	Slices of $S(\vec{q}, t)$ for $qx = 0$ in model A	112
5.21	Time dependence of the fit parameters for model A	113
5.22	Time series of $S(\vec{q}, t)$ for $\vec{q} = (qx, 0)$	115
5.23	$S(\vec{q}, t)$ vs t for several wavevectors.	116

TABLES

2.1	Experimental parameters	20
2.2	Brightness and coherence lengths for different sources	21
3.1	Characteristics of detectors	49
5.1	Experimental parameters for different quenches.	96

LIST OF COMMON SYMBOLS

R_s	distance source-sample.
R_{slit}	distance source-source x-y slits.
R_d	distance sample-detector.
R_c	distance sample-collimating pinhole.
D	collimating pinhole diameter.
l_z	longitudinal coherence length.
l_x	horizontal transverse coherence length.
l_y	vertical transverse coherence length.
l_s	typical speckle size.
d_{sx}, d_{sy}	horizontal and vertical source size.
d_{slit}	source x-y slits opening.
d_p	pixel size, $22.4\mu\text{m}$.
$\Delta q_p = \frac{2\pi d_p}{\lambda R_d}$	\vec{q} space increment.
τ	exposure time.
$V(\vec{r}, t)$	digital signal measured at position $\vec{r} = \vec{r}_{ij}$ between time t_k and $t_k + \tau$. \vec{r}_{ij} and t_k are discrete due to the nature of the detection process.
$n_i(\vec{r}, t)$	incident number of photons on the surface of a pixel \vec{r} at t as measured by a reference detector having near unit detective quantum efficiency.
$n_d(\vec{r}, t)$	detected number of photons.
$\alpha = \frac{\langle n_d \rangle_t}{\langle n_i \rangle_t}$	detective quantum efficiency of the detector.
$\langle V(\vec{r}, t) \rangle_t = \frac{1}{N} \sum_{i=1}^N V(\vec{r}, t_i)$	time average of signal V . It is measured by averaging a time sequence of N scans.
$S_{i,V}^2(\vec{r}) = \frac{1}{N-1} \sum_{i=1}^N (V(\vec{r}, t_i) - \langle V(\vec{r}, t) \rangle_t)^2$	estimator for the variance of V , measured with a time sequence of N scans.
$\langle V(\vec{r}, t) \rangle_{\vec{r}} = \frac{1}{N_p} \sum_{i=1}^{N_p} V(\vec{r}_i, t)$	spatial average of signal V . It is measured by averaging N_p pixels in a given scan at time t .
$S_{\vec{r},V}^2(t) = \frac{1}{N_p-1} \sum_{i=1}^{N_p} (V(\vec{r}_i, t) - \langle V(\vec{r}, t) \rangle_{\vec{r}})^2$	estimator for the variance of N_p pixels.
$2\theta_{\parallel}$	detector angle with respect to the incident beam direction, measured in the scattering plane
$2\theta_{\perp}$	detector angle measured perpendicular to the scattering plane.

RÉSUMÉ

Cette thèse est la première mesure de spectroscopie des fluctuations d'intensité (SFI) de la dynamique d'une transition de type ordre-désordre dans un alliage binaire, utilisant des rayons X cohérents. Des faisceaux intenses de rayons X cohérents de quelques μm de diamètre sont maintenant produits en filtrant spatialement et en fréquence des rayons X émis par une source synchrotron de troisième génération. Des patrons de diffraction tacheté de la surstructure (100) du Cu_3Au ont été mesurés avec un détecteur bi-dimensionnel de type CCD. Pour mesurer les fluctuations temporelles et spatiales du facteur de structure, la résolution spatiale et la réponse du détecteur furent mesurées.

Nous avons développé une technique d'application générale, basée sur une comparaison de la moyenne, variance et corrélation spatiale du signal avec des fluctuations d'intensité suivant une loi de Poisson. Les corrélations spatiales du signal réduisent les fluctuations du signal détecté par rapport au bruit de Poisson prévu. Cette technique permet de mesurer la fonction de résolution et l'efficacité quantique du détecteur. La largeur de la fonction d'autocorrélation spatiale des patrons de diffraction tachetés est en accord quantitatif avec la largeur d'un patron de diffraction de Fraunhofer des trous, élargi par la fonction de résolution du CCD. Le contraste du patron tacheté est plus faible que prévu. La grandeur caractéristique des taches et leur contraste dépendent des propriétés optiques du faisceau et de la taille du trou utilisé comme prévu.

Nous avons mesuré des patrons tachetés après une trempe de l'état désordonné fcc à l'état ordonné $L1_2$. Les taches dominantes apparaissent rapidement après la trempe, mais reste fixe dans l'espace réciproque. La croissance des domaines est mesurée par un accroissement de l'intensité moyenne et un rétrécissement de la largeur du pic. Cette dynamique est en accord avec des simulations numériques du modèle A. L'amplitude des fluctuations est faible et leur durée est très longue. Nous avons démontré que la SFI est réalisable dans une nouvelle bande d'énergie. La SFI est un nouvel outil pour l'étude des phénomènes hors d'équilibre dans les solides.

ABSTRACT

We extended Intensity Fluctuation Spectroscopy (IFS) to atomic scale fluctuations using coherent X-rays. Intense beams of coherent X-rays, with diameters of a few μm , are now easily produced by *spatial filtering* of *monochromatic* X-rays generated from synchrotron radiation insertion devices. This thesis is the first X-ray IFS measurement on the non-equilibrium dynamics of an order-disorder phase transition in a binary alloy. Speckle patterns of Cu_3Au (100) were measured with a two-dimensional Charge-Coupled Device detector. To quantify the spatial and temporal fluctuations of the speckle pattern, the spatial resolution and the noise of this detector were carefully characterized.

We developed a statistical technique for characterizing position-sensitive detectors (PSD), using estimators such as the average, variance, and *spatial correlation functions*. Spatial correlations between pixels reduce the fluctuations of the signal when compared to Poisson noise. Using this technique, the resolution function and quantum efficiency of two PSD's were measured. The widths of spatial correlation functions of static speckle patterns from Cu_3Au agree well with the widths of the Fraunhofer diffraction of the pinholes used, convolved with the detector resolution. The speckle pattern contrast is smaller than expected. The speckle size and contrast depend on the incident X-ray optics as expected for X-ray speckle.

We measure Cu_3Au speckle patterns after a quench from the fcc disordered phase to the L1_2 ordered phase. The dominant speckles appear after the quench, and remain *fixed* in reciprocal space. The domain coarsening is seen as an overall increase in intensity and a sharpening of the diffuse peak. These dynamics agree with numerical simulations of model A. Both experiments and simulations show that the time fluctuations of the intensity have small amplitudes and very long time scales. This differs from equilibrium IFS, where fluctuations amplitudes are as large as the signal. We have demonstrated the feasibility of XIFS in Cu_3Au . The use of coherent X-rays allows one to measure the ordering kinetics of binary alloys in new ranges of length and time scales.

ACKNOWLEDGMENTS

I wish to thank Prof. Mark Sutton for introducing me to a very exciting field of research. I had the privilege of participating in the first coherent X-ray experiments with a world leader in the field. I would like to thank Mark for his constant intellectual stimulation and technical support throughout my stay at McGill. He always anticipated my computational needs, and provided me with the tools that made the work possible. This thesis benefitted from his careful reading and constructive criticism. I would like to thank him especially for taking me on very nice trips around the world, in countries where the wine and cheeses were wonderful!

I wish to thank also Dr. Brian Stephenson whose vast synchrotron experience was invaluable for this project. I have always enjoyed participating in experiments with him, and his visits to Montreal were important for the data analysis. I am grateful to Dr Brian Rodricks for providing the CCD detector and the detector expertise. Just a few years ago, very few people had or even used CCD detectors for X-ray scattering. We were very fortunate to have him in the team. A superb team of scientists helped to perform these experiments: Dr. Lonnie Berman, Dr. Randy Headrick, Dr. Carol Thompson, Prof. Simon Mochrie, Dr. Glen Held and Dr. S.E. Nagler. Thank you all!

I wish to acknowledge the close collaboration of Dr Ralf Brüning on the detector calibration section. With Ralf's help, my writing skills have improved, and his constructive criticisms were always appreciated. I am eternally grateful to my dear friend Geoff Soga for the careful editing of the thesis, often done at very short notice! I wish to acknowledge the collaboration of Dr. Ken Elder and Dr. Bertrand Morin on the data analysis of numerical simulations of model A.

A special thank is addressed especially to my teachers at McGill. Teaching is an essential but thankless task. I benefitted from the courses I took from Profs. Martin Grant, Peter Grütter, Martin Zuckermann, John Ström-Olsen, and Hong Guo.

My work benefitted from the excellent computer administrators who did an outstanding job over the years with often limited resources. Thanks to Loki Jorgensen, Martin Lacasse, Geoff Soga, Paul Mercure and Juan Gallego. Thank you for all the computer tips you gave me, and for fixing the system so professionally. My data analysis benefitted from many excellent computer programs written by M. Lacasse and M. Sutton.

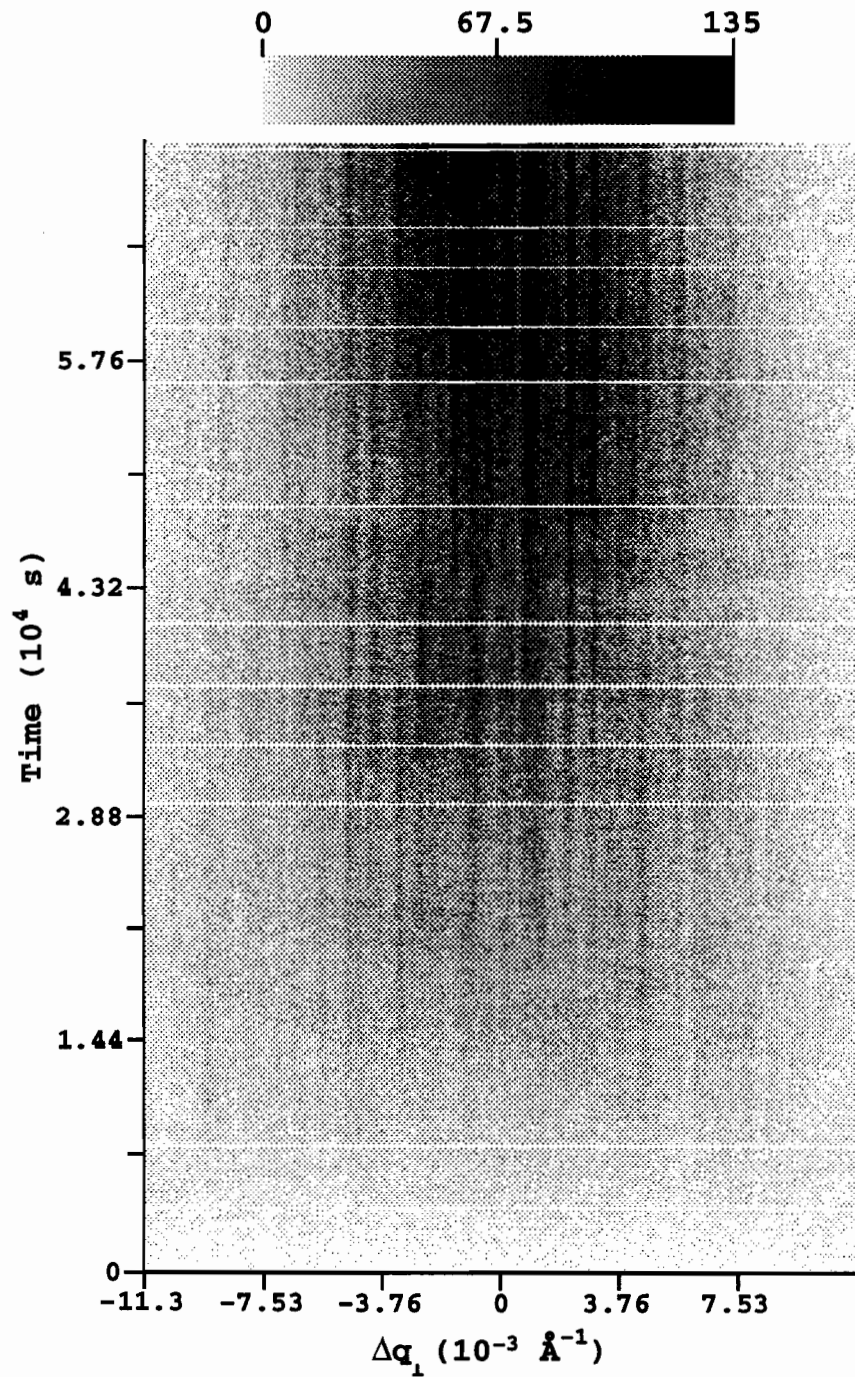
Special thanks goes to the technical staff of the department. John Egyed, Michel Champagne, Frank van Gils, Saviero Biunno, Mario della Neve and Michel Beauchamp helped me in many experiments. Many thanks also to Paula Domingues, Diane Koziol, Joanne Longo, Cynthia Thomas and Lynda Corkum for making dealings with the department both simple and always pleasant.

I have enjoyed the intellectual stimulation and the friendship of many people at McGill. Thanks to the old timers in my group, Jacques, Yushan, Tianqu, Steve, Ralf, Hank, and to my present colleagues, Randa, Biao Hao, and Matt for many very stimulating discussions where I always learned something. I also enjoyed discussions and good times with my office mates and friends of room 422: Bian, Ming Mao, Erol, Claude, Mohsen, Christine, Morten, Ningjia, Stéphane, James, Sajan, Ke Xin, Bertrand... During my stay at McGill, I had the pleasure to meet wonderful people who made my stay in Montreal, an experience to remember: Geoff, Brett, Joel, Ling, Nick, Martin L., Martin K., Pascal, Eugenia, Judith, Mikko, Nicolas, Mary D., Karim, Ross, Ian, Jian Hua, Benoit, Philip, Niri, Francois, Margerita, Mark S., Martin Z., Martin G., Peter, Louis... I will miss you all!

I would like to thank Mark Sutton for supporting me financially. I am also very grateful for the scholarships I received from the Natural Sciences and Engineering Council of Canada et le Fonds pour la Formation des Chercheurs et l'Aide à la Recherche du Québec. In these time of budgetary restraint, I feel sad that young people today who are starting their graduate degrees might not have the same opportunities as I had several years ago.

J'aimerais remercier mes parents pour m'avoir laissé choisir librement ma voie dans la vie. Merci aussi pour votre aide financière et votre support moral pendant toutes ces longues années à étudier. Finally, I wish to express my gratitude to Mary Mardon for totally supporting my decision to go into graduate studies and research. Watching her battling the demons of her own dissertation alone and without the many resources that are available to people in the sciences has both inspired me and made me more aware of the intellectual and moral support that I have been lucky enough to receive. I would especially like to thank her for putting her own dissertation on hold this summer and fall, so that I could complete mine. I hope to offer the same support to you that you offered to me. I could not have done it without you.

Intensity fluctuation spectroscopy with coherent
X-rays



INTRODUCTION

The development in the last 30 years of high energy synchrotron rings dedicated to the production of synchrotron radiation has made possible many exciting new fields of science and technology. This high energy physics *technology* is used today by molecular biologists, chemists, physicists, medical doctors and engineers to find solutions to both fundamental and applied problems. In the field of solid-state physics, these sources have made many X-ray spectroscopy or scattering techniques feasible or more powerful. Some examples include time-resolved X-ray scattering, nuclear X-ray scattering, surface X-ray scattering, resonant and non-resonant X-ray scattering, Diffraction Anomalous Fine Structure (DAFS), coherent X-ray scattering, as well as many more¹. This thesis will report on one of these recent developments which uses the high brilliance and transverse coherence of synchrotron radiation in X-ray scattering experiments. This transverse coherence greatly affects the observed X-ray diffraction patterns from disordered materials.

When coherent light illuminates a material with a random microstructure, a graininess in the scattered beam is observed, called speckle. Speckle is a general feature of scattered coherent light from a medium where some dielectric constant fluctuations are present. It was first observed over a century ago by Exner[3, 4] and Laue[5] on Fraunhofer diffraction rings produced by light scattered from small particles. It is seen in many experimental systems: in laser light reflected by a rough surface², in the

¹See the wide variety of scientific projects investigated in modern synchrotron radiation facilities like the European Synchrotron Radiation Facility or the National Synchrotron Light Source in their respective Annual Reports [1, 2].

²In this case, speckle is considered as a nuisance that must be minimized to reveal the surface profile [6].

scattered light from equilibrium density fluctuations in a fluid, and in electron microscope images from amorphous semiconductors¹. It is a characteristic of the *theoretical* structure factor of a random system where the fluctuations are caused by phasons in a quasi-crystal [8, 9, 10], phonons [11] and charge density waves in a perfect crystal, and in simple models of metallic glasses [10].

A speckle pattern is caused by coherent interference between all the scattered secondary waves randomly phase shifted by different regions of the material. If these regions move in time with characteristic time τ_c , then the intensity correlation function of the scattered light for a given scattering wave-vector \vec{q} , $\langle I(\vec{q}, t)I(\vec{q}, t + \delta t) \rangle_t$, will decay with a characteristic time related to τ_c . Understanding the functional dependence of the correlation time on the momentum transfer allows for the study of transport properties of a material.

For example, the equilibrium intensity fluctuations of dilute spherical particles in a simple liquid follow $\langle I(\vec{q}, t)I(\vec{q}, t + \delta t) \rangle_t \propto 1 + e^{-2Dq^2\tau}$, where D is the diffusion constant of the spheres in the liquid and q is the wavevector [12]. A plot of $1/\tau_c$ versus q^2 allows a measurement of the transport properties of the material. Using the Stokes approximation, $D = k_B T / (6\pi\eta a)$, where k_B is the Boltzmann constant, T the temperature, η the viscosity of the liquid, and a the sphere's average radius [12]. Thus by using spherical particles with a known radius a , one can measure the temperature dependence of the viscosity by measuring the temperature dependence of D , or by measuring the radius of some particle in a solution of known viscosity.

This time correlation technique, often called Dynamic Light Scattering (DLS), Intensity Fluctuation Spectroscopy (IFS), or Photon Correlation Spectroscopy (PCS)² has been used extensively with visible light to study the dynamics of very slow equilibrium and non-equilibrium fluctuations in *transparent* fluids, colloids and liquid crystals undergoing continuous phase transitions. This technique studies fluctuations with frequencies ranging from 10^{-3} to 10^8 Hz and length scales ranging between 2000 Å and 20 μm [14, 13]. It is complementary to inelastic light scattering tech-

¹See Ref. [7] and references within.

²For an introduction to IFS, see the book by B. Chu[13], and references within.

niques like Brillouin and Raman scattering, which study faster processes ($10^7 - 10^{14}$ Hz) involving respectively acoustic and optical waves in materials. This technique has been limited to length scales above 200 nm when using lasers with the shortest wavelength available. The largest wavevector observable with visible light scattering is $q_{max} = (4\pi/200) \text{ nm}^{-1}$, which corresponds to back scattered light. This technique has been recently extended to hard X-rays by using high brilliance second generation synchrotron radiation sources, thus improving the technique sensitivity to *atomic* length scales with $q_{max} \approx (4\pi/0.1) \text{ nm}^{-1}$.

Sutton et al.[15] demonstrated that by appropriately collimating an incoherent monochromatic source of X-rays like an X-ray insertion device¹, one can get sufficient coherent flux to perform IFS at atomic length scales, through *opaque* materials. This first demonstration showed time independent speckle patterns from antiphase domains in Cu_3Au (100) [15]. Since this first demonstration, static speckle patterns have been observed in different systems: in gold coated diblock copolymer films[16], in synthetic multilayers[17], in the superlattice peak of a charge density wave in the one-dimensional conductor $\text{K}_{0.3}\text{MoO}_4$ [18], and in another binary alloy Fe_3Al [19, 20].

Sutton et al. also demonstrated the feasibility of X-ray IFS (XIFS) in a study of the kinetics of an order-disorder phase transition in Cu_3Au after a quench from the high temperature disordered phase to the low temperature ordered phase by measuring the fluctuations of the scattered intensity with a scintillation counter [21]. Within the last year, XIFS experiments have been performed successfully on the equilibrium critical fluctuations of the binary alloy Fe_3Al [19] and in equilibrium fluctuations in gold colloids[22, 23]. Brauer et al. [19] performed XIFS at atomic length scales, observing intensity fluctuations when the Fe_3Al sample was heated above the critical temperature of the continuous phase transition. Dierker et al. [22] have measured exponential correlation functions, characteristic of the Brownian motion of gold particles in a colloid with excellent signal to noise ratio. Chu et al. [23] also observed XIFS on a gold colloid using X-ray produced by a bending magnet beamline, with

¹An insertion device is a periodic magnetic structure used to generate synchrotron radiation.

a coherent flux several orders of magnitude smaller than Ref. [22]. These recent experiments show the power and promise of this new field of X-ray scattering. This new technique promises to be quite helpful in studying the equilibrium and non-equilibrium dynamics in binary alloys, in amorphous materials and molten metals, in liquid crystals, in complex fluids like colloids and polymer blends, in gel networks, and in incommensurate systems like charge density wave or ferroelectric systems.

IFS is well understood for equilibrium fluctuations, but little experimental work has been performed using IFS on the non-equilibrium coarsening dynamics of a first order phase transition. One of the only other studies of coarsening in a first-order transition with dynamic light scattering was done on a binary fluid (conserved order parameter), where the intensity fluctuations were studied after quenches into the miscibility gap. Kim et al. [24] found that the power spectrum of the scattered intensity $P(f)$ measured after the quench was non-Lorentzian, following $P(f) \propto \exp(-|f|/f_0)$, with $f_0 < 0.1$ Hz. This power spectrum appeared to be stationary because it was present in the power spectrum of different consecutive subsets of their data. Hydrodynamic effects complicated the analysis of the intensity fluctuations in this system by increasing the droplet growth exponent by a factor of five, and causing oscillation in $P(f)$.

A simpler system for studying the intensity fluctuations due to the coarsening dynamics of a first order phase transition would be a system with a non-conserved order parameter (NCOP) like a binary alloy. Such a system would be free of hydrodynamic effects, and should be easier to understand because of the absence of conservation laws.

This thesis reports on the first study of the ordering kinetics of an order-disorder phase transition in a binary alloy with *coherent X-rays*. We measure the scattered intensity fluctuations from the superlattice peak (100) of Cu_3Au , after a quench from the equilibrium disordered state above the critical temperature T_c of the first order phase transition, to the degenerate ordered state below T_c . The speckle patterns of Cu_3Au generated by coherent illumination of the sample are measured with a

charge-coupled device (CCD) array. The main advantage of the CCD array is to record hundreds of two dimensional speckle patterns, with a spatial resolution which matches the fine speckle features, and with a time resolution of tens of seconds to a few minutes [25], which is sufficient to measure the speckle pattern dynamics.

The binary alloy Cu_3Au was chosen because it is a classical system for the study of a first-order phase transition. It has been studied for over half a century¹. The equilibrium properties of this system are analogous to a three dimensional Ising model with antiferromagnetic coupling. Furthermore, the non-equilibrium ordering kinetics of Cu_3Au has been studied extensively with incoherent illumination in recent years [28, 29, 30, 31, 32, 33]. After a quench through the order-disorder transition, nucleation and growth of ordered domains occur². After nucleation, the late stage dynamics is controlled by curvature driven growth with the average domain size $R_d \propto t^{1/2}$. The scaling properties of the incoherent structure factor are well established and are universal features of ordering. The spherically averaged structure factor scales as $S(q, t) = t^{d/2} f(qt^{1/2})$, where d is the dimensionality, and $f(x)$ is a universal scaling function.

The theoretical foundation of IFS with non-equilibrium phenomena is not as well understood as its equilibrium counterpart. Therefore, it is important both experimentally and theoretically to develop an understanding of these phenomena. Another motivation for this thesis is to investigate the non-self averaging behavior of first-order phase transitions[36]. Roland and Grant [36] predicted $1/f$ noise in the fluctuations around scaling for a macroscopic quantity like the average domain size, in analogy with self-organized criticality. This is believed to be a universal feature of first-order phase transitions.

In Chapter 2, we review some of the important concepts of coherence and scattering with coherent X-rays. Most of this terminology was developed in the last thirty years by light scatterers, but may be unfamiliar to scientists specialized in the fields of X-ray or neutron scattering. In Chapter 3, we develop statistical techniques for

¹The order-disorder transition in Cu_3Au is discussed in several X-ray scattering books [26, 27]

²Excellent reviews are given in Ref. [34, 35].

characterizing position-sensitive detectors (PSD) which were inspired from our data analysis of speckle patterns in Cu_3Au . In this work, it was essential to separate the noise due to counting statistics from genuine intensity fluctuations, and to develop an understanding of the inherent spatial correlations of the detected signal in a PSD in order to estimate the speckle size. This work has been published recently [37]. Chapter 4 discusses the experimental method used for this work, expanding points developed earlier in Chapter 2. In Chapter 5, results from static and time-dependent measurements are reported, and compared to numerical simulations.

COHERENT X-RAYS

2.1 Definitions of coherence

In coherence theory, two types of coherence are discussed: longitudinal and transverse coherence. Longitudinal coherence is a wave's property of interfering with a *time-delayed* copy of itself. Longitudinally coherent light will produce fringes in a Michelson interferometer until its two mirrors are separated from each other by a distance much larger than the longitudinal coherence length [38] given by

$$l_l \approx \lambda^2 / 2\delta\lambda, \quad (2.1)$$

where λ is the wavelength of the light, and $\delta\lambda/\lambda$ is the relative bandwidth of the source. Eq. 2.1 follows from the Heisenberg uncertainty principle $\delta\nu\tau_l \approx 1$, where $\delta\nu$ is the frequency bandwidth of the light and $c\tau_l = l_l$, where c is the speed of light in vacuum. Stated physically, the longitudinal coherence length is the characteristic length along the direction of propagation of a wave packet emitted by a given polychromatic source. For a monochromatic wave, l_l is infinite. For a constant relative bandwidth $\delta\lambda/\lambda$, l_l is proportional to the wavelength used.

A wave is called transversely coherent if it can produce fringes in a Young's double-slit experiment. The transverse coherence length l_t characterizes the loss of coherence or of fixed phase relationship between two points on a wavefront. In a Young's double-slit experiment, no interference fringes are seen [38] if the two slits are separated by a distance d much larger than the transverse coherence length

$$l_t = \lambda R_s / 2d_s = \lambda / 2\alpha, \quad (2.2)$$

where R_s is the source to observation point distance, d_s is the source size, and $\alpha = d_s/R_s$ is the opening angle subtended by the source at the point of observation. Stated in another fashion, if one places two pinholes separated by $d < l_t$ in front of an extended source, the interference patterns generated by each element of the source overlap each other, thus interference is visible. For a point source, the transverse coherence length diverges. For an extended source, l_t increases with increasing λ , making it easier to observe interference effects at longer wavelengths. The transverse coherence length is also inversely proportional to the opening angle subtended by the source at the point of observation.

Formally, a source is coherent when there is a non-zero statistical correlation between electric fields $\vec{E}(r_1, t_1)$ and $\vec{E}(r_2, t_2)$. The mutual coherence function is defined by

$$\Gamma_{12} = \langle \vec{E}^*(r_1, t_1) \vec{E}(r_2, t_2) \rangle_t, \quad (2.3)$$

where the average is taken over time.

It can be shown [39] that the mutual coherence function far away from an **incoherent source** made of independent radiators¹ simplifies to the spatial Fourier transform of the source intensity profile. Then the complex coherence factor

$$\mu(\vec{r}_1, \vec{r}_2) = \frac{e^{-\frac{\pi i(\vec{r}_2^2 - \vec{r}_1^2)}{\lambda R_s}} \int_{-\infty}^{\infty} \int_{-\infty}^{\infty} dx' dy' I(\vec{r}') \exp\left(\frac{2\pi i}{\lambda R_s} \vec{r}' \cdot (\vec{r}_2 - \vec{r}_1)\right)}{\int_{-\infty}^{\infty} \int_{-\infty}^{\infty} dx' dy' I(\vec{r}')}, \quad (2.4)$$

where the vector \vec{r}' is a small vector in the source plane, λ is the average wavelength of the source, and \vec{r}_1 and \vec{r}_2 are two vectors in the plane of observation perpendicular to the optical axis of the source and placed at a distance R_s from the source. This is called the Van Cittert-Zernicke theorem. It holds for small angles of observation such that the transverse distance $|\vec{r}_2 - \vec{r}_1| \ll R_s$, and under quasi-monochromatic conditions. This theorem is very useful because it can be used to calculate the fringe contrast in a Young's double-slit experiment [39] for most light sources.

¹This assumption characterizes nearly all optical sources other than a laser. It can be applied to synchrotron radiation.

Following Goodman [39], we define the coherence area by

$$A_c = \int_{-\infty}^{\infty} \int_{-\infty}^{\infty} dx' dy' |\mu(x', y')|^2. \quad (2.5)$$

For an incoherent source with a *spatially uniform* intensity profile, it can be shown [39] using the Van Cittert-Zernicke theorem that the coherence area in Eq. 2.5 reduces to the product of the two perpendicular transverse coherence lengths of the source defined in Eq. 2.2. Eq. 2.5 will be used in section 5.1.2 to calculate the observed contrast of our diffraction patterns.

2.2 Properties of synchrotron radiation

The use of synchrotron radiation over the past thirty years has revolutionized the field of X-ray scattering. Today's range of scientific activities in the X-ray scattering community would not be as rich and varied without the use of synchrotron radiation¹. This radiation has several properties which make it ideal for experiments in physics, chemistry, biology, medicine, engineering, material science and in the development of new drugs and technologies. The photon energy available at a synchrotron ranges from the infrared to gamma rays. No other single source is able to cover such a wide band of energies. This energy can be easily selected for a given system by the use of monochromators and gratings, with a wide range of energy bandpass, $\delta E/E$, typically between 10^{-2} to 10^{-4} . The major improvement over standard laboratory sources is the huge increase in intensity, allowing studies of time dependent dynamics and spectroscopies on a wide range of time scales (10^{-12} – 10^4 s), or studies of scattering from sample volumes as small as $1(\mu\text{m})^3$ (10^{11} atoms!), weak scatterers like light elements, surfaces and interfaces a few monolayers thick, nuclear charge, or magnetic moments. The source divergence is quite small due to the radiation cone which is shrunk to an opening angle of $1/\gamma$, where $\gamma = E/m_0c^2$, m_0c^2 is the rest mass of the electron or positron, and E is its total energy in the laboratory frame. Furthermore, the source size is small. These two properties yield a large coherent flux which can be

¹For an introduction to synchrotron radiation, the reader is referred to recent books on the subject [40, 41].

used in coherent X-ray scattering experiments and X-ray holography. The incident X-ray polarization can be controlled to produce linear, circular or elliptical polarizations. This allows for resonant and non-resonant magnetic X-ray scattering, or circular dichroism. Finally, the beam is pulsed, which allows for different spectroscopies and excitation modes to be studied.

The X-ray sources used in this work were insertion devices. An insertion device is a periodic magnetic structure inserted in a straight part of the synchrotron ring. These devices cause the electron orbit to oscillate as a sine wave. The X-rays generated by these oscillations are linearly polarized in the plane of the orbit. Most scattering experiments using synchrotron radiation use a vertical scattering plane to reduce polarization losses [26].

These sources are characterized by a large brilliance or brightness, B , defined as the flux of photons per unit of phase space, which is the flux of photons per unit of source area per unit of solid angle measured in photons/s/mm²/mrad²/0.1%BW, where BW stands for the X-ray bandwidth $\delta\lambda/\lambda$. For many optical transformations, the brightness is an invariant. For example, a mirror can be used to focus the X-ray beam to a small spot size, but the beam divergence is increased in proportion, thus the product of the spot size times the beam divergence is conserved. In practice, the brightness may be lost in absorption by windows, or in optical aberration on optical elements like mirrors and monochromators.

An insertion device is characterized by a deflection parameter

$$K = \alpha\gamma = eB\lambda_0/(2\pi m_0c^2) \approx 0.934B(T)\lambda_0(cm), \quad (2.6)$$

where α is the maximum deflection angle of the electron trajectory with respect to the axis of the insertion device. This angle characterizes the deflection of the electron trajectory by the periodic magnetic field B with laboratory frame period λ_0 [40]. An insertion device with $K > 1$ is called a wiggler while one with $K < 1$ is called an undulator.

A wiggler has a very broad energy spectrum similar to a bending magnet spectrum [41]. Because the angular deviation caused by a wiggler is quite large compared to

the angular cone of the emitted synchrotron radiation, the radiation emitted from different periods of the wiggler adds incoherently. Therefore, the peak intensity is proportional to the number of magnetic periods N . This device has more operational freedom than a bending magnet because the magnetic field can be made as large as necessary without changing the electron orbit.

The radiation emitted by an undulator is quite different from wiggler radiation because the radiation emitted from a given period adds coherently with the radiation generated at a later time at the subsequent period [41]. The brightness is proportional to N^2 , and its spectrum is peaked around well defined wavelengths called harmonics, functions of λ_0 [41]. The wavelengths of these harmonics along a direction parallel to the plane of the orbit are

$$\lambda_n = \frac{\lambda_0}{2n\gamma^2} \left(1 + \frac{K^2}{2}\right), \quad (2.7)$$

where $n = 1, 2, 3, \dots$ [41], and their relative wavelength spread is

$$\frac{\delta\lambda}{\lambda} = \frac{1}{nN}. \quad (2.8)$$

With current undulator designs, the relative bandwidth of a given undulator harmonic is typically in the range of a few percent.

2.3 X-ray scattering

In an X-ray scattering experiment, one measures the differential cross-section of X-rays coherently scattered by the electrons in the material. Using the first Born approximation, the X-ray differential cross-section

$$\frac{d\sigma}{d\Omega} = \Phi_s / I_i \propto S(\vec{q}, t), \quad (2.9)$$

where Φ_s is the scattering rate measured in a solid angle $d\Omega$ subtended by the detector, I_i is the incident intensity, and the structure factor is

$$S(\vec{q}, t) = |\rho(\vec{q}, t)|^2, \quad \text{where } \rho(\vec{q}, t) = \int d\vec{r} \rho(\vec{r}, t) e^{-i\vec{q}\cdot\vec{r}}. \quad (2.10)$$

Here $\rho(\vec{q}, t)$ is the Fourier transform of the electronic density, $\rho(\vec{r}, t)$, and $\vec{q} \equiv \vec{k}_f - \vec{k}_i$, where \vec{k}_f and \vec{k}_i are respectively the wavevectors of the scattered and incident X-rays

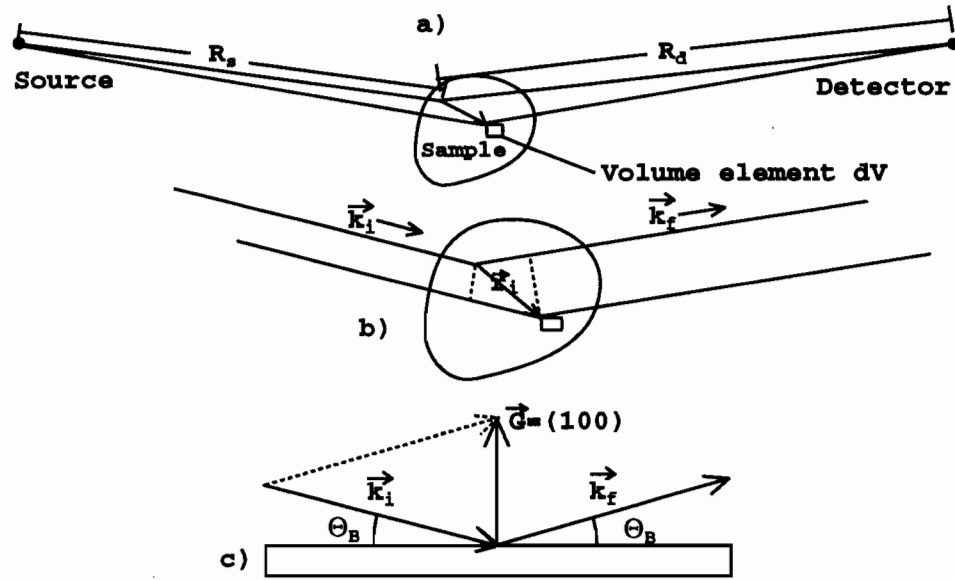


Figure 2.1: a) The Fraunhofer condition holds for plane wave illumination such that the distance source-sample R_s and the distance sample-detector R_d are much larger than the sample size. b) The phase difference, in the Fraunhofer condition. The phase difference $\delta = \vec{k}_f \cdot \vec{r}_i - \vec{k}_i \cdot \vec{r}_i$, where the magnitude of the incident and scattered wavevectors $|\vec{k}_i| = |\vec{k}_f| = 2\pi/\lambda$, and \vec{r}_i is the position of the volume element dV in the sample reference frame. c) The Bragg condition.

with magnitude $|\vec{k}_f| = |\vec{k}_i| = 2\pi/\lambda$. The electronic density may change in time. This dynamics can be tracked by the time dependence of the structure factor.

In scattering theory, the first Born approximation [27] assumes weak scattering or a small scattering volume. This approximation is also used for the kinematic theory of X-ray diffraction. In this treatment, the Fraunhofer diffraction condition is assumed which means that the sample is illuminated by plane waves originating from a point source, placed far away from the scattering center. It is important to stress that in a typical scattering experiment, this condition is not fully satisfied and one must correct for the finite source size and input divergence (see Fig. 2.1a). For synchrotron radiation, this condition can be more easily satisfied because of the small input divergence and source size. In this thesis, the experimental setup is close to the Fraunhofer condition. This will change qualitatively the structure factor observed. We will discuss this in more detail in section 2.6.

For a crystal, the electronic density is periodic and has translational symmetry, so

that

$$\rho(\vec{r}) = \rho(\vec{r} + \vec{T}), \quad \text{with } \vec{T} = x_1\vec{a}_1 + x_2\vec{a}_2 + x_3\vec{a}_3, \quad (2.11)$$

where \vec{T} is a translation vector obtained by a linear combination of the primitive translation vectors \vec{a}_i , and the integers x_i . The crystal electronic density is also periodic in Fourier space, with primitive translation vectors

$$\vec{G} = h\vec{b}_1 + k\vec{b}_2 + l\vec{b}_3, \quad \text{where} \quad (2.12)$$

$$\vec{b}_1 = 2\pi \frac{\vec{a}_2 \times \vec{a}_3}{\vec{a}_1 \cdot (\vec{a}_2 \times \vec{a}_3)}, \quad \vec{b}_2 = 2\pi \frac{\vec{a}_3 \times \vec{a}_1}{\vec{a}_1 \cdot (\vec{a}_2 \times \vec{a}_3)}, \quad \vec{b}_3 = 2\pi \frac{\vec{a}_1 \times \vec{a}_2}{\vec{a}_1 \cdot (\vec{a}_2 \times \vec{a}_3)}, \quad (2.13)$$

and h, k, l are integers called the Miller indices. Note that the vectors \vec{a} and \vec{b} are perpendicular, so $\vec{a}_i \cdot \vec{b}_j = 2\pi\delta_{ij}$, where $i, j = 1, 2, 3$. Using the fact that the Fourier transform of a crystal is also periodic in reciprocal space, it is easy to show¹ that scattering maxima occur in Eq. 2.10 when the scattering vector $\vec{q} \equiv \vec{G}$. These maxima are called Bragg peaks. The Bragg condition occurs when the phase difference between light scattered from parallel planes of atoms (see Fig. 2.1b) is a multiple of 2π . The scattering angle θ_B , shown in Fig 2.1c, is given by Bragg's formula

$$2d_{hkl} \sin \theta_B = \lambda, \quad (2.14)$$

where θ_B is the Bragg angle, and $d_{hkl} = 2\pi/|\vec{G}|$. For an infinite crystal, these Bragg peaks are Dirac delta functions in reciprocal space, but for a finite crystal of linear dimension D , their intrinsic width in reciprocal space is proportional to $1/D$. When some disorder with correlation length $\xi < D$ is present in the sample, the Bragg peak width becomes proportional to $1/\xi > 1/D$.

In a crystal, since the atomic positions are periodic, the structure factor $S(\vec{q})$ in Eq 2.10 can be rewritten as a sum of waves scattered by each lattice point in the crystal. Then, one finds

$$S(\vec{q}) \propto \left| \sum_i F \exp(-i\vec{q} \cdot \vec{r}_i) \right|^2, \quad (2.15)$$

¹This is derived for example in Chap. 2 in Kittel [42].

where \vec{r}_j are the positions of the lattice points in the scattering volume, and F is the form factor of all the atoms in the basis of the unit cell given by

$$F = \sum_j f_j \exp(-i\vec{q} \cdot \vec{r}_j), \quad (2.16)$$

where f_j and \vec{r}_j are respectively the usual atomic form factor and position in the unit cell for the j th atom in the basis. Note that f_j is complex, with $f_j = f_{1j} + if_{2j}$ ¹. For an orthorhombic lattice, it is easy to show [26], by evaluating the sums in Eq. 2.15, that the structure factor

$$S(\vec{q}) = |F|^2 \frac{\sin^2(N_1 a_1 q_x)}{\sin^2(q_x a_1)} \frac{\sin^2(N_2 a_2 q_y)}{\sin^2(q_y a_2)} \frac{\sin^2(N_3 a_3 q_z)}{\sin^2(q_z a_3)}, \quad (2.17)$$

where $\vec{q} = (q_x, q_y, q_z)$, and $N_1 a_1$, $N_2 a_2$, $N_3 a_3$ are the sample linear dimensions. Fig. 2.7 shows the structure factor of a two dimensional square lattice with lattice constant a with 100×100 atoms. The peak intensity in this approximation is proportional to the square of the sample volume, the width of the Bragg peak along q_i is the inverse of the sample linear size $\Delta q_i \propto \frac{1}{N_i a_i}$, and the scattered integrated intensity over all wavevectors is proportional to the sample volume (or the total number of atoms). The side lobes in Fig. 2.7 are the secondary maxima of Eq. 2.17.

Another important property of scattered X-rays is the change of state of polarization of the incident beam by the scattering process. X-rays polarized perpendicular to the scattering plane, the plane parallel to both incident and scattered wavevectors, suffer no loss of intensity while those polarized in the scattering plane suffer a $\cos^2(2\theta_B)$ loss [26]. This effect can be used to make an X-ray polarizer or analyzer by scattering from a crystal with $2\theta_B = \pi/2$. In the experiments reported here, the scattering plane was vertical, and perpendicular to the polarization vector.

Finally, in X-ray scattering experiments, one needs to select a narrow energy band of the incident polychromatic beam. In the hard X-ray region of the spectrum, this is done by using Bragg reflection from a nearly perfect single crystal, called a monochromator. To understand the wavelength dependence of l_i , one needs to understand the

¹The complex term is caused by absorption of the incident or scattered wave. For hard X-rays, $f_1 \approx Z$, where Z is the number of electrons in the atom and f_2 is related to the mass absorption coefficient, μ_m , by $f_2 = \mu_m \frac{A}{2N_A \lambda r_e}$ [43], where A is the atomic mass, N_A the Avogadro number and $r_e = e^2 / (4\pi\epsilon_0 m_0 c^2) = 2.82 \times 10^{-15}$ m the classical electron radius [41].

wavelength dependence of $\delta\lambda/\lambda$ for a single crystal monochromator. It is calculated by taking the derivative of Bragg's law in Eq. 2.14 with respect to λ . For a perfectly collimated polychromatic X-ray beam, it is easy to show [44] that the relative bandwidth

$$\delta\lambda/\lambda = \delta\theta/\tan\theta = r_e N \lambda^2 \text{Re}\{F\}/(\pi \sin 2\theta \tan\theta) \propto N \text{Re}\{F\} d_{hkl}^2. \quad (2.18)$$

Eq. 2.18 was simplified by replacing $\delta\theta$ by the Darwin width of an absorbing semi-infinite monochromator crystal with $\delta\theta = \frac{r_e N \lambda^2 \text{Re}\{F\}}{\pi \sin 2\theta}$ [26], where N is the electron density, r_e is the classical electron radius, $\text{Re}\{F\}$ is the real part of the form factor of the Bragg plane, and recalling that $\sin\theta = \lambda/2d_{hkl}$. One finds that $\delta\lambda/\lambda$ is weakly dependent on wavelength through the wavelength dependence of $\text{Re}\{F\}$. Brauer et al. [44] also consider the case where the incident X-ray beam has a finite divergence. Eq. 2.18 then becomes $\delta\lambda/\lambda = (\delta\theta + D_i)/\tan\theta$, where D_i is the input divergence. Then the relative bandwidth will be wavelength dependent through the wavelength dependence of θ .

2.4 X-ray scattering from Cu_3Au

The binary alloy Cu_3Au is a classical system for studying the properties of first order phase transitions. It has been studied for over half a century, and its equilibrium and non-equilibrium *incoherent* scattering is fairly well understood. Most of the earlier X-ray scattering work consisted of measuring the equilibrium properties of the alloy, like the equilibrium temperature dependence of the long range order, the anisotropy of the Bragg peak in reciprocal space due to the presence of antiphase domains, and the diffuse scattering from the short range order fluctuations. Several textbooks discuss the scattering from Cu_3Au [26, 27]. The focus of research on Cu_3Au has changed in recent years. For example, some of the work has been focused on studying the nature of the phase transition on the surface layers of Cu_3Au single crystals [45, 46, 47], while others have studied the non-equilibrium kinetics of Cu_3Au , after a quench from its disordered phase to the ordered phase [28, 29, 30, 31, 32, 33]. The latter work is motivated by a need to improve our understanding of non-equilibrium

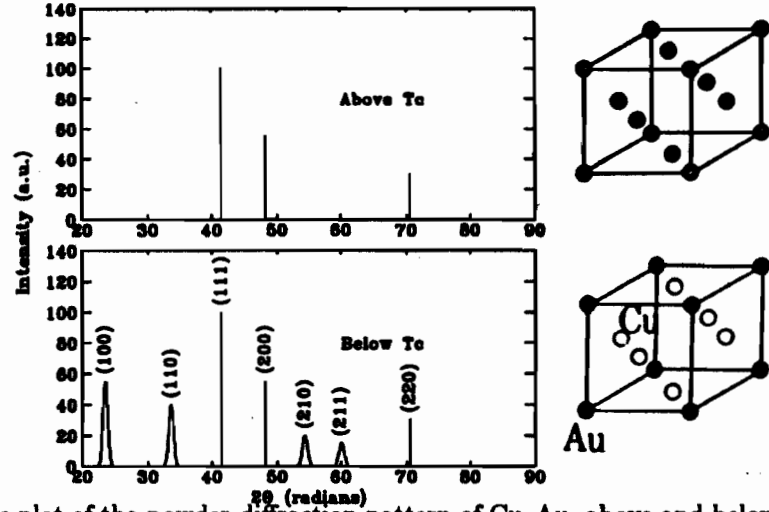


Figure 2.2: A schematic plot of the powder diffraction pattern of Cu_3Au , above and below T_c using $a = 3.771 \text{ \AA}$ [32], and $\lambda = 1.5405 \text{ \AA}$, with domains below T_c of 100 \AA . The equilibrium real space structure is shown beside. (From Ref. [27])

processes. These processes are important in the fabrication of many technologically relevant materials. Furthermore, since non-equilibrium processes are quite challenging conceptually, much work remains to be done to understand them.

Cu_3Au goes through an order-disorder transition at a critical temperature $T_c = 390^\circ\text{C}$ [26]. Fig 2.2 shows the structure factor for a powder sample and the real space equilibrium structure above and below T_c . Below T_c , the structure is $L1_2$ with a basis consisting of one Au atom occupying the corner position $(0, 0, 0)$ of the cubic lattice with 3 Cu neighbors on the neighboring face center sites $(1/2, 1/2, 0)$, $(0, 1/2, 1/2)$, $(1/2, 0, 1/2)$ of the unit cell. Above this transition temperature, the structure is fcc because each atomic species diffuses through the lattice randomly, yielding an effective atomic form factor for each site of the basis given by $\bar{f} = 1/4 f_{\text{Au}} + 3/4 f_{\text{Cu}}$, where f_{Au} and f_{Cu} are the form factors of Au and Cu respectively. The peaks in Fig. 2.2 which remain unchanged above T_c are called fundamental peaks and are not affected by the degree of long range order in the crystal. The peaks that disappear above T_c are called superlattice peaks. Following Warren [26], it is easy to show that the integrated scattered intensity

$$S(h, k, l) = \begin{cases} 16\left(\frac{3f_{\text{Cu}}}{4} + \frac{f_{\text{Au}}}{4}\right)^2 & \text{for } h, k, l \text{ all odd or even,} \\ \psi_{\text{BW}}^2 (f_{\text{Au}} - f_{\text{Cu}})^2 & \text{for mixed } h, k, l, \end{cases} \quad (2.19)$$

where ψ_{BW} is the Bragg Williams order parameter, ranging between zero in the disordered phase, to one in the fully ordered phase. The integrated intensity of a superlattice peak is proportional to the square of the order parameter, and to the square of the difference between the atomic form factors of Cu and Au. The fundamental peaks occur for unmixed h, k, l , and are independent of ψ_{BW} .

Although the long range order disappears above T_c , some weak scattering is still observable around the superlattice peak. It is due to the tendency of Au atoms, for example, to surround themselves with three Cu atoms as nearest neighbors, causing short range spatial correlations in the disordered states which are observable as diffuse scattering [27, 48].

The ordered state has a four fold degeneracy since the Au atom can occupy any of the four sites of the basic unit cell. This degeneracy leads to the formation of four competing phases forming large antiphase domains, separated by domain walls. There are two types of domain walls in Cu_3Au [30, 32]. Type I domains walls are formed by a half-diagonal glide in planes perpendicular to the cubic axes¹. They have low interfacial energy because they do not require a change of nearest neighbor coordination along the interface [32]. Type II walls are formed by a half-diagonal glide across planes perpendicular to the cubic axes². They have a higher interfacial energy because they require a change of nearest neighbor configuration. It is well known that these domain walls give rise to an anisotropy in the Bragg peaks of the ordered phase. Warren [26] derives the line shape of the superlattice peak, assuming that it is caused only by Type I walls, where domains forming along the three crystallographic axes are independent of each other, and the probability of crossing a domain wall, γ , is small. The scattered intensity for planes with Miller index (hkl) , where h, k are indexes with the *same parity* is

$$S(hkl) = |F|^2 \frac{N_1 \gamma}{\gamma^2 + (\pi h)^2} \frac{N_2 \gamma}{\gamma^2 + (\pi k)^2} \frac{\sin^2(\pi N_3 l)}{(\pi l)^2}, \quad (2.20)$$

where the N_i are proportional to the sample linear size. This peculiar line shape gives

¹In the [001] direction, this corresponds to displacing a domain with respect to another by $1/2[110]$

²In the [001] direction, this corresponds to displacing a domain with respect to another by $1/2[101]$

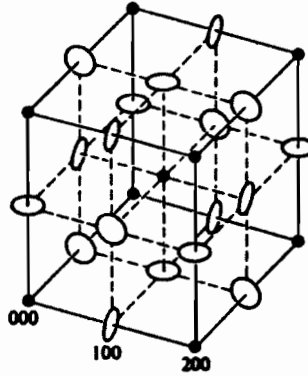


Figure 2.3: The superlattice peak in reciprocal space from Ref. [26]. It is anisotropic because Type I walls form in the three crystallographical direction. The fundamental reflections are shown with solid circles.

rise to disks in reciprocal space shown in Fig 2.3. For the (100) superlattice peak for example, this gives a disk oriented in a plane parallel to the (011), with the narrower dimension along the (100). A more detailed lineshape is given in Ref. [30].

Recent time-resolved studies of the ordering kinetics of Cu_3Au have revealed quite rich dynamical features of the ordering and coarsening process. Noda et al. [29] found that the structure factors in the later stage can be rescaled by a simultaneous renormalization of time and space, with the characteristic length $L(t) \propto t^{1/2}$. They found that a Lorentzian-square function was a good scaling function for all quench depths. They found evidence of an incubation time for the formation of a critical droplet size, which later grows to macroscopic size. This incubation time diverges as the temperature approaches the critical point.

Ludwig et al. [30] studied the early stage of the nucleation and growth process with a fraction of a second time resolution. They found evidence that the early kinetics of the short range order fluctuations for quench temperatures just below T_c is a relaxation to a metastable state, which then slowly decays by nucleation and growth. For lower temperatures, the time scales of the two processes become comparable, and for $T_c - T > 34$ K, they found evidence for continuous ordering at a temperature well above the classical spinodal temperature.

Nagler, Shannon et al. [31, 32, 33] identified three distinct kinematic regimes: nucleation, ordering and coarsening. A delay in the growth of the integrated intensity

was attributed to an incubation time for nucleation like in Ref. [29]. It was found that the structure factor crosses over from having a Gaussian line shape during the early stage of the ordering process, where the ordered nuclei are small and embedded in a disordered matrix, to a Lorentzian-square line shape during the late time coarsening process. They found that the anisotropic disk shape reflection sharpens in time with the same exponents along the disk plane and through the disk axis. They showed that the scaling exponent in the coarsening regime is consistent with the non-conserved order parameter (NCOP) exponent $n = \frac{1}{2}$ for curvature driven growth.

We will study the late stage of the ordering kinetics of the phase transition after a quench from the high temperature fcc phase to the low temperature phase, and record the scattered intensity of the Cu_3Au (100) super-lattice peak with a CCD array (see Fig. 2.2).

2.5 Production of coherent X-rays: experimental method

Before the invention of lasers, incoherent thermal sources were used to produce coherent illumination. By collimating an incoherent source like a mercury arc lamp [49] with a small aperture, a coherent light source can be obtained. The first speckle patterns measured with hard X-rays were observed with an *incoherent* source! This was demonstrated by Sutton et al. [15] for an incoherent source of X-rays by limiting the beam size to dimensions comparable to its horizontal and vertical transverse coherent lengths, l_x, l_y , given by rewriting Eq. 2.2 as

$$l_x = \frac{\lambda R_s}{2d_{sx}}, \quad l_y = \frac{\lambda R_s}{2d_{sy}}, \quad (2.21)$$

where R_s is the distance between the source and the point of observation, while d_{sx} and d_{sy} are the horizontal and vertical source size. Fig. 2.4 shows a typical experimental set up for such an experiment. Common symbols are defined on page IX for convenience, and the particular experimental parameters for the two runs where we collected data are shown in Table 2.1. Typical values at wavelength $\lambda = 1.24 \text{ \AA}$ are given in Table 2.2.

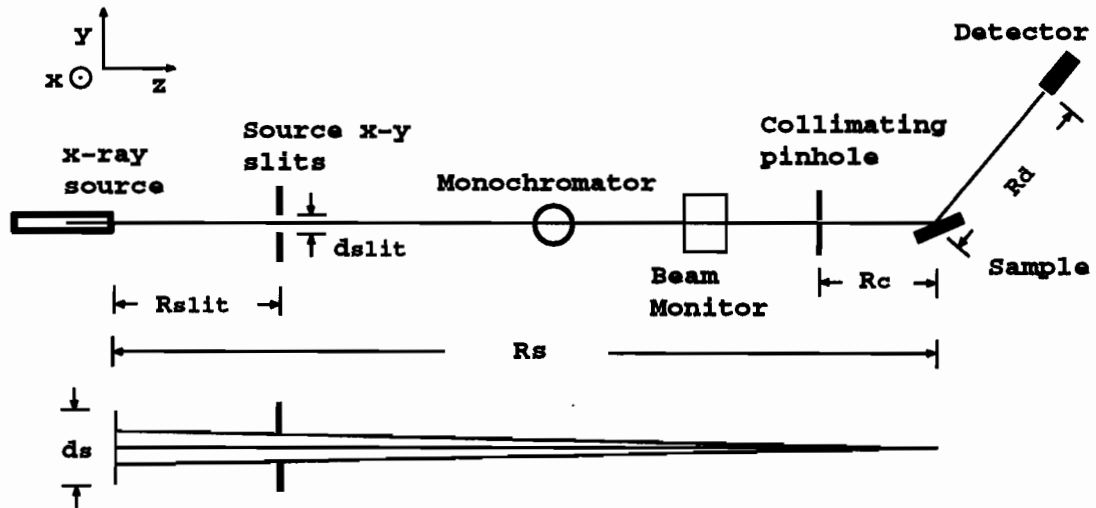


Figure 2.4: The experimental setup. All variables are defined on page IX for convenience, and their typical values are given in Table (2.1). The X-rays are generated by a wiggler or an undulator. The source x-y slits allow for a change of the coherence lengths by reducing the effective source size. A double Si (111) monochromator is set near 7.0 keV to prevent Cu fluorescence. The incident beam intensity is monitored by an ion chamber. The collimating pinhole is used to limit the beam size to a dimension comparable to the transverse coherence lengths. One of two detectors is normally used: a CCD array, or a scintillator masked by a micron size pinhole which is mounted on an x-y translation stage.

Table 2.1: Experimental parameters for the two experimental setups. The horizontal and vertical source sizes d_{sx} and d_{sy} are given by their full widths at half maximum (FWHM). The effective source size can be reduced by closing some upstream slits placed at a distance R_{slit} from the source.

Beamline	CHES	NSLS X25
Source type	undulator	Wiggler
E keV	7.0	6.9
R_s m	25.8	27.8
R_{slit} m	17.8	10.5
d_{sx} mm	2.55	1.46
d_{sy} mm	0.167	0.068
R_c cm	6.7	6.75
R_d m	0.95	1.04

In a typical incoherent X-ray scattering experiment with a laboratory source, $\lambda = 1.54 \text{ \AA}$, $d_s \approx 1-10\text{mm}$, $R_s \approx 1\text{m}$ resulting in $l_t \approx 80-800 \text{ \AA}$. Limiting the beam size to such small length scales would not give any useful coherent flux. Since the beam size at the sample position is also a few mm, the speckle pattern is washed out by incoherent averaging [10]. Because of the high collimation of third-generation X-ray sources and the large source-sample distances, typical coherence lengths are between 1-10 μm . Since these sources are several orders of magnitude brighter than conventional sources, one can obtain a coherent beam with sufficient flux by collimating the incident beam with pinholes of diameter comparable to $l_{x,y}$ (typically 4 – 7 μm).

The coherent flux, Φ_c , is calculated from the integrated flux going through a rectangular aperture with height l_y and length l_x , which accepts the full source divergence α_x, α_y . It is easy to show that

$$\Phi_c = \frac{\lambda^2 B(\lambda) \delta\lambda}{4 \lambda}, \quad (2.22)$$

where $B(\lambda)$ is the brightness of the source. The relative bandwidth $\delta\lambda/\lambda$ selected by the monochromator is only weakly dependent on wavelength as shown in Eq. 2.18. Therefore the presence of the λ^2 term makes these experiments easier to perform at longer wavelengths. Typical values of this flux at X25 and CHESS are given in Table 2.2. With 1.2×10^6 photons/s, X25 gives a coherent flux comparable to a laboratory source. An increase of a factor 500 should be gained by performing experiments at the Advanced Photon Source (APS).

Past and current coherent X-ray experiments can be limited by this small coherent

Beamline	l_t μm	l_t μm	B	Φ ph/s
X25 NSLS	1-25	0.44	3×10^{14}	1.2×10^6
CHESS Undulator	0.6-10	0.44	3×10^{15}	1.2×10^7
APS Undulator	10-10	0.44	1.5×10^{17}	6×10^8

Table 2.2: Brightness and coherence lengths for different sources at 1.24 \AA . Brightness measured in $ph/s/mm^2/mrad^2/0.01\%BW$.

flux. A currently active area of research is investigating ways to improve the flux going through the collimating pinhole, by sacrificing some vertical coherence with focusing X-ray optics like a mirror [50, 51] or asymmetrically-cut crystals [44, 52]. The idea originated from the fact that l_y is typically an order of magnitude larger than l_x for synchrotron radiation, so that if one focuses the X-ray beam in the vertical direction until the vertical divergence matches the horizontal divergence, then $l_y = l_x$, and the coherent flux is increased through the pinhole because of the focusing. These techniques are important since they will make it possible to tailor the coherence volume $l_x l_y l_z$ for a given experiment requiring, for example, a much smaller beam size than the smallest of the transverse coherence lengths, or requiring equal horizontal and vertical transverse coherence lengths [44].

Another approach for improving the scattered intensity is by optimization of the product of the coherent flux, Φ_c , and the fraction of scattered X-rays with respect to energy. One can show¹ that the integrated scattered intensity for Cu_3Au

$$I_s \approx B(\lambda) \lambda^2 \frac{\delta\lambda}{\lambda} \psi^2 \mu_{\text{Cu}_3\text{Au}} |f_{\text{Au}} - f_{\text{Cu}}|^2, \quad (2.23)$$

where ψ is the order parameter, f_{Cu} is the complex atomic form factor for Cu, and $\mu_{\text{Cu}_3\text{Au}}$ is the absorption length in Cu_3Au . Eq. 2.23 depends on the X-ray contrast of the two elements Cu and Au. One way to increase the scattered intensity for the study of order-disorder transitions is to choose the material with the largest difference in atomic number. For the sake of simplicity, let us assume a fully ordered material, with $\psi = 1$, and assume that one can tune the insertion device in such a way that B is constant over the wavelength range of interest. Fig. 2.5 shows the approximate scattered intensity integrated in q over the (100). The energy in this experiment was set to 7 KeV, which is close to the optimal condition for Cu_3Au . In a real experiment, windows and monochromators may complicate this relationship; thus, it is often simpler to measure the scattered intensity in order to optimize it.

¹One needs to combine absorption effects and the integrated intensity of a superlattice peak in a binary alloy found in Eq. 2.19, assuming no polarization losses.

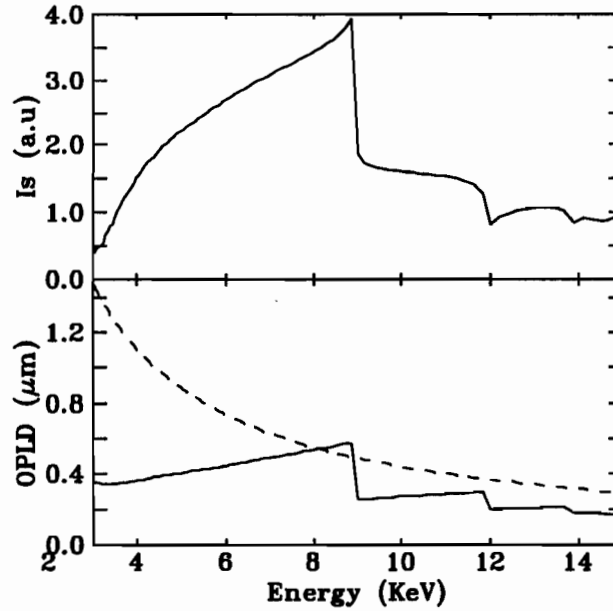


Figure 2.5: The energy dependence of the scattered intensity I_s , calculated from Eq. 2.23. The atomic form factors for Cu and Au were taken from Ref. [53], and the mass absorption coefficients were calculated from these form factors. The discontinuities are the absorption edges for Cu (near 9 keV) and Au (near 12 and 13.7 keV). Below, the optical path length difference in Cu_3Au $2\mu \sin^2 \theta_B$ (solid line) and the longitudinal coherence length l_l (dashed line). Here l_l is calculated from Eq. 2.1 and 2.18, neglecting the weak energy dependence of $\text{Re}\{F\}$ for the Si (111) monochromator (only 1.5 % change over the energy range shown).

2.5.1 Coherence volume

The other condition for coherent scattering is that the optical path length differences (OPLD) in the sample be smaller than the longitudinal coherence length of the source, l_z , such that

$$\text{OPLD} < l_z = \frac{\lambda^2}{2\delta\lambda}, \quad (2.24)$$

where $\delta\lambda/\lambda$ is the relative wavelength bandwidth of the source of radiation [38]. For 7.0 keV X-rays, filtered with a Si_{111} monochromator, $\delta\lambda/\lambda = 1.4 \times 10^{-4}$, giving $l_z \approx 0.6 \mu\text{m}$. This coherence condition is achieved by using a thin sample, or a sample with large enough absorption, or by scattering with a grazing angle of incidence [16, 17]. Specialized monochromators can also be used to change the longitudinal coherence length. For example, Dierker et al. [22] have used a wide bandpass X-ray multilayer monochromator to select the smallest l_l possible in order to maximize the available coherent flux. It is also possible to increase l_l by using higher order reflections of Si, or by using high resolution monochromators like those used for

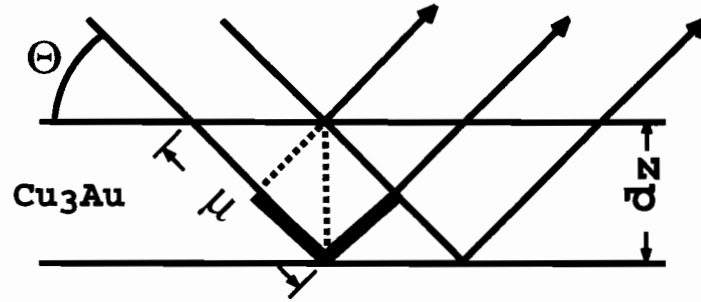


Figure 2.6: The condition for longitudinal coherence. It is satisfied because the optical path difference (wider line), $2d_z \sin \theta$, is smaller than the longitudinal coherence length. The X-ray penetration depth perpendicular to the surface is $d_z = \mu \sin \theta$, where μ is the sample X-ray absorption length. Therefore, the longitudinal coherence condition is rewritten as $l_l < 2\mu \sin^2 \theta$.

Mössbauer scattering or high energy inelastic scattering [54].

For Cu_3Au , the absorption length at 1.77 \AA is $\mu = 4.2 \mu\text{m}$ [55]. The difference in optical path is illustrated in Fig. 2.6 for a symmetric Bragg reflection. The Bragg angle $\theta = 13.67^\circ$, and d_z is the X-ray penetration depth in the material perpendicular to the surface. The longitudinal coherence condition is fulfilled because the path length difference, $2d_z \sin \theta = 2\mu \sin^2 \theta = 0.47 \mu\text{m}$, is smaller than l_z . Note also that for Cu_3Au , the OPLD is smaller than l_l for all energies below 8.1 KeV or above 9.0 KeV as seen in Fig. 2.5.

The longitudinal coherence condition depends on the angle θ of the reflection. Pindak et al. [18] have clearly demonstrated this effect by observing the contrast of speckle patterns on superlattice reflections of a charge density wave in $\text{K}_{0.3}\text{MoO}_3$. For this material, the longitudinal coherence condition is valid for $\theta < 9.5^\circ$ [18]. They demonstrated that speckle is observable for low order reflection with $\theta < 11^\circ$, but disappears for reflections with $\theta = 22.5^\circ$.

2.6 Structure factor with coherent X-rays

Here two models are presented which give the reader a few examples on the present and possible uses of coherent X-ray beams.

2.6.1 Coherent X-ray scattering for the study of isolated defects or artificially made structures

It is important to realize that the definition of the structure factor must be slightly modified to take into account the coherence of the beam. The measured structure factor is typically an *ensemble average* of the coherent structure factor calculated over the coherence volume of the source. This ensemble average is typically performed over the illuminated volume $V \gg l_x l_y l_z$, where the coherence volume is the product of the coherence lengths. Mathematically formulated, the structure factor observed in a typical X-ray experiment is

$$S(\vec{q}, t) = \langle \left| \int_{l_x l_y l_z} d\vec{r} \rho(\vec{r}) e^{-i\vec{q} \cdot \vec{r}} \right|^2 \rangle_V. \quad (2.25)$$

When the illuminated volume is comparable to the coherence lengths of the source, the structure factor becomes sensitive to individual realizations of the ensemble, thus becoming sensitive to the exact position of the atoms in the illuminated volume.

The first *theoretical* model shown here was suggested in the original demonstration of speckle by Sutton et al. [15]. It consists of isolating single defects in a few μm diameter beam to study the detailed microstructure of the material and to improve our structural understanding of defects in condensed matter. In typical X-ray experiments, one illuminates millions of defects *incoherently*, since the illuminated area is typically $1 \text{ mm} \times 1 \text{ mm}$ but the X-ray beam transverse coherence lengths are on the order of 1000 \AA . Since the characteristic length scale of a defect ranges between a few \AA to a few μm , the presence of defects is seen only in slight changes of the line shape of the Bragg peak which can be hard to interpret as a given defect type.

As opposed to incoherent experiments, coherent X-ray scattering techniques are more sensitive to the exact position of atoms in the scattering volume. It gives a structure factor that is very different depending on the type of defects illuminated. An example of this sensitivity to disorder is shown in Fig. 2.7. The structure factor of a two dimensional perfect crystal with a square lattice calculated using Eq. 2.17 is shown. The calculation is shown for a crystal of 100×100 atoms. The peak height

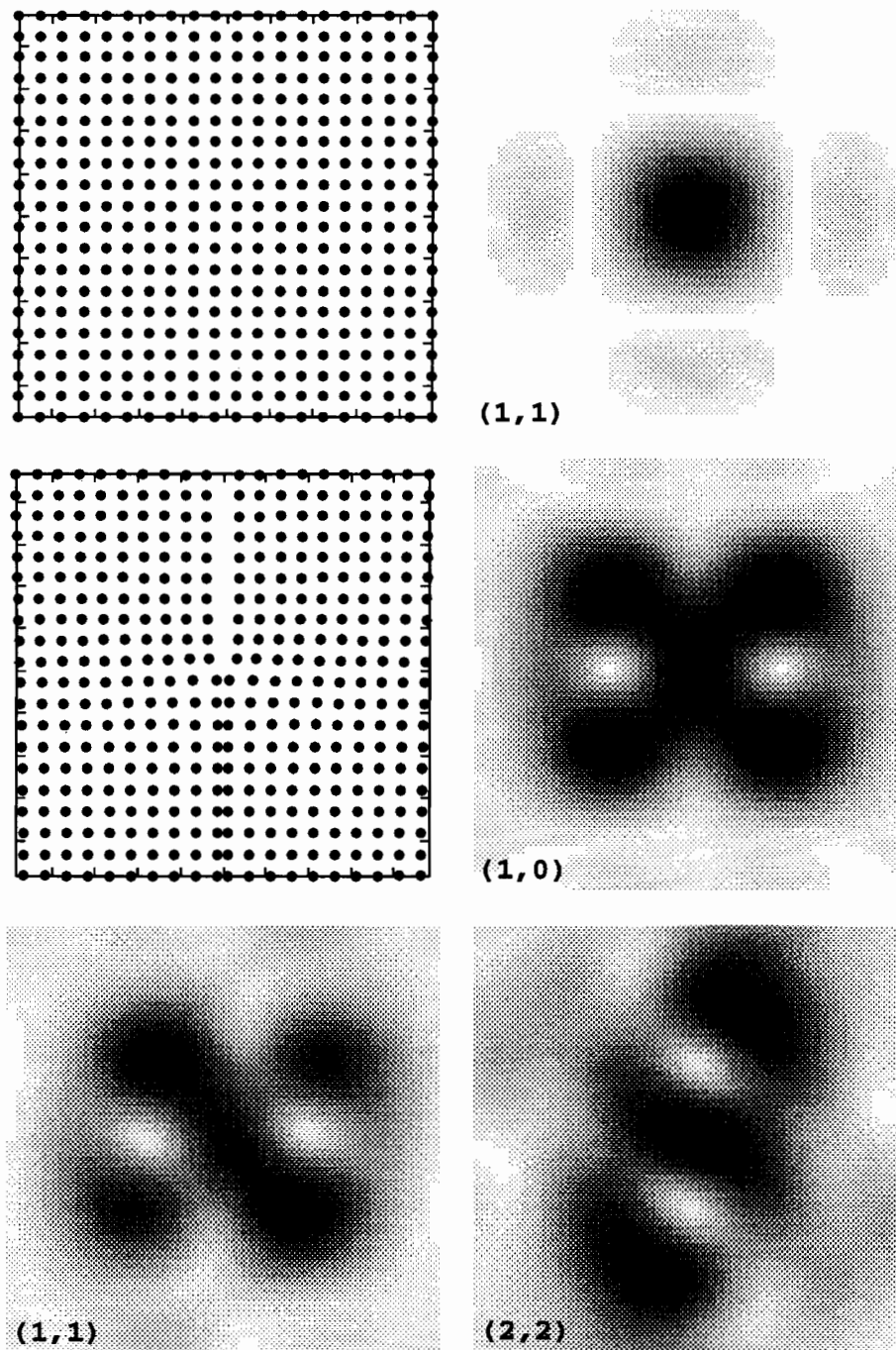


Figure 2.7: (Top left) The central 20×20 atoms in a real space square lattice with lattice parameter a , and $S(\vec{q})$ centered on the $(1,1)$ (top right). A linear grey scale from 0 to 10^8 is used to display the $(1,1)$. The wave vector range shown from the $(1,1)$ centered on the middle of the image is $(2\pi/a \pm 4\pi/L, 2\pi/a \pm 4\pi/L)$, where the sample size $L = 100a$. (Middle) The central 20×20 atoms of a real space two dimensional lattice distorted by an edge dislocation, and $S(\vec{q})$ centered around the $(1,0)$ using the same range as the top image. (Bottom) $S(\vec{q})$ centered around the $(1,1)$ and $(2,2)$. The Bragg peaks split into several satellites. The structure factor varies depending on the position in reciprocal space.

goes as the square of the number of atoms, and its width as the inverse of the sample size. The middle image in Fig. 2.7 shows the real space lattice of a crystal distorted by an edge dislocation¹. The structure factor calculated from Eq. 2.15 is also shown for the (1,0), (1,1) and (2,2). The original structure factor of the perfect lattice is split into satellites of comparable magnitude but weaker intensity than the perfect crystal. The splitting of the satellites is on the order of the FWHM of the perfect square lattice. In order to look at defects on a quasi-perfect single crystal of Si, one would look for structure on an angular scale comparable to the Darwin width of Si. By using a high resolution set up, this experiment could be feasible.

One should note that some experiments have already been done on simple structures, such as two-dimensional gratings and multilayers. Recently, Robinson et al. [17] observed speckle from a multilayer of $\text{GaAs}_x\text{AlGaAs}_{1-x}$. They developed several theoretical approaches which could fit the observed random speckles. They found that coherent X-ray scattering can be quite a sensitive tool for studying the disorder of the lattice orientation on the surface of their multilayers. It appears that it can give additional information which cannot be obtained from other experimental techniques.

Shen et al. [57] studied the structure of a two dimensional grating, using X-rays with a transverse coherence length of the order of one μm . They did not match the illuminated volume with the transverse coherence length of the source, thus some ensemble average was performed. The measured X-ray scattering was modeled adequately with the kinematic theory using a sample size given by the transverse coherence length of the source. They found that the added transverse coherence gives microscopic as well as additional mesoscopic information on the grating structure, such as its period, width and shape, atomic registry with the substrate, and crystal lattice strain. Recently, Tanaka et al. [58] have used the technique demonstrated above to measure surface diffusion and strain in the same oxidized grating as in

¹The displacements $d\vec{r} = (dx, dy)$ for all atoms were calculated by a simple model of an edge dislocation, given by Eq. 30.6 in Christian [56]. Here the displacement of the atom at position $\vec{r} = (x, y)$ in the crystal is $dx = b/4\pi(1 - \nu)[2(1 - \nu) \arctan(y/x) + xy/(x^2 + y^2)]$, and $dy = -b/4\pi(1 - \nu)[(1 - 2\nu) \ln(x^2 + y^2) - x^2/(x^2 + y^2)]$, using a Poisson Ratio $\nu = 1/3$, and a Burgers vector $b = a$, where a is the lattice parameter.

Ref. [57].

2.6.2 Scattering from a binary alloy in equilibrium

We derive next some of the properties of the structure factor $S(\vec{q}, t)$ obtained with coherent light incident on a typical binary alloy like Cu_3Au and Fe_3Al , in thermal equilibrium below the critical temperature, T_c , of a first order or a continuous phase transition. This section is motivated by the need to understand the equilibrium short range order fluctuations in equilibrium and non-equilibrium experiments which occur within large antiphase domains. This section serves also as a good demonstration of equilibrium IFS. The results derived below are valid for a large class of systems like magnetic systems and binary alloys belonging to the non-conserved Ising universality class. The discussion is limited to the region well above or well below a continuous phase transition, outside the critical region¹. The properties of the $S(\vec{q}, t)$ for a system in the conserved Ising universality class will be qualitatively consistent with those of the non-conserved order parameter, although the exact dynamical properties will have a different wavevector dependence due to the conservation laws.

The *theoretical model* used for this demonstration is a time-dependent Landau-Ginzburg field theory model called model A in the Hohenberg and Halperin classification scheme [59]. This model describes well the equilibrium and non-equilibrium properties of a binary alloy with a non-conserved order parameter [60, 61], where the order parameter is proportional to the sublattice concentration of one of the atomic species. The equilibrium dynamics of the order parameter is obtained by minimizing a coarse-grained free energy F and solving

$$\frac{\delta\psi(\vec{r}, t)}{\delta t} = -M \frac{\delta F}{\delta\psi} + \eta(\vec{r}, t), \quad (2.26)$$

where $\psi(\vec{r}, t)$ is the order parameter measured at discrete position \vec{r} on a square lattice and at discrete time t , M is the mobility, and $\eta(\vec{r}, t)$ is a noise term which takes into account the coupling of the system to the thermal bath by fast variables. Here, the

¹For a review of critical dynamics, see Hohenberg and Halperin [59].

noise term is Gaussian and uncorrelated in space and time with

$$\langle \eta(\vec{r}, t) \eta(\vec{r}', t') \rangle = 2k_B T M \delta(\vec{r} - \vec{r}') \delta(t - t'), \text{ and } \langle \eta(\vec{r}, t) \rangle = 0, \quad (2.27)$$

where k_B is the Boltzmann constant, $\delta(x)$ is the Dirac delta function, and the brackets refer to an ensemble average. The free energy functional used is

$$F = \int d\vec{r} \left(\frac{\kappa}{2} |\nabla \psi(\vec{r}, t)|^2 + \frac{r}{2} \psi^2(\vec{r}, t) + \frac{w}{4} \psi^4(\vec{r}, t) \right), \quad (2.28)$$

where κ , r , and w are phenomenological constants, with $w > 0$, and $r = r_0(T/T_c - 1)$, such that $r > 0$ in the disordered phase above T_c , and $r < 0$ when two ordered phases are stable below T_c , and $r = 0$ at T_c . The gradient term is used to model the interfacial free energy between two different phases. In the single phase equilibrium above T_c , F has a single well centered at the equilibrium value $\langle \psi \rangle = 0$. Below T_c , F has a double well, with symmetric minima at $\psi = \pm \sqrt{\frac{-r}{w}}$.

Eq. 2.26 can be rewritten as

$$\frac{\delta \psi(\vec{r}, t)}{\delta t} = -M \left(r \psi(\vec{r}, t) + w \psi^3(\vec{r}, t) - \kappa \nabla^2 \psi(\vec{r}, t) \right) + \eta(\vec{r}, t). \quad (2.29)$$

Eq. 2.29 was solved numerically using Euler's method to discretize time and a nearest-neighbor approximation was used for ∇^2 [60]. The simulations were performed in two dimensions using periodic boundary conditions, and system sizes of 128^2 , 256^2 , or 512^2 . For this simulation, the thermodynamic constants were set to one such that $\kappa = -r = w = M = 1$. To simulate the equilibrium dynamics, one of the phases was selected by setting the initial condition $\psi = \sqrt{\frac{-r}{w}}$, after which ψ was updated until the system reached equilibrium. After reaching equilibrium, the structure factor was simulated with time steps ranging between $dt = 0.005 - 0.05$.

To understand the static and dynamic properties of the equilibrium order parameter, let us study the disordered state. Above T_c , one can neglect the cubic non-linear term in Eq. 2.29. Then, the dynamics of the order parameter is given by a stochastic linear equation, which can be easily solved. Taking the Fourier transform of Eq. 2.29, one finds

$$\frac{\delta \psi(\vec{q}, t)}{\delta t} = -M(r + \kappa q^2) \psi(\vec{q}, t) + \eta(\vec{q}, t). \quad (2.30)$$

From this equation, one sees clearly that large time fluctuations of the order parameter will be exponentially damped with correlation time

$$\tau_c = \frac{1}{M(r + \kappa q^2)}. \quad (2.31)$$

Long wavelength fluctuations of the order parameter have slower decay rates than shorter wavelength fluctuations. This will be important for understanding the time correlation of the structure factor discussed later. Below T_c , a similar treatment can be done by a Taylor expansion of ψ in Eq. 2.29 around its equilibrium value $\psi = \pm\sqrt{-r/w}$. Then one finds $\tau_c = \frac{1/M}{\kappa q^2 - 2r}$. Note that for a conserved order parameter, the long range diffusion yields an extra q^2 dependence in the denominator, thus τ_c diverges at low \vec{q} [12].

Following Eq. 2.10, the structure factor $S(\vec{q}, t) = \psi(\vec{q}, t)\psi^*(\vec{q}, t)$, where $\psi(\vec{q}, t)$ is the Fourier transform of the order parameter. The *time independent* ensemble averaged structure factor is the well known Ornstein-Zernicke structure factor given by

$$S(\vec{q}) = \begin{cases} \frac{I_{SR}}{r + \kappa q^2} & \text{for } T > T_c, \\ I_{LR}\delta(\vec{q}) + \frac{I_{sr}}{\kappa q^2 - 2r} & \text{for } T < T_c, \end{cases} \quad (2.32)$$

where I_{LR} and I_{SR} are respectively the peak intensities of the long range order and short range order.

Note that to obtain Eq. 2.32, an ensemble average over *all possible configurations* was done. If one looks at the structure factor of the instantaneous atomic configuration $S(\vec{q}, t)$, one does not simply observe a Lorentzian. Fig 2.8 shows $S(\vec{q}, t)$ for a typical binary alloy in equilibrium below T_c , numerically simulated with model A. Regions with large intensity are next to regions with low intensity, with a characteristic size of one pixel in the image, corresponding to

$$\Delta q = 2\pi/L, \quad (2.33)$$

where L is the sample linear dimension. The equilibrium fluctuations of the scalar order parameter add a random modulation to the ensemble averaged structure factor in Eq. 2.32. A slice through the structure factor is shown next in Fig 2.9 for $q_y = 0$.

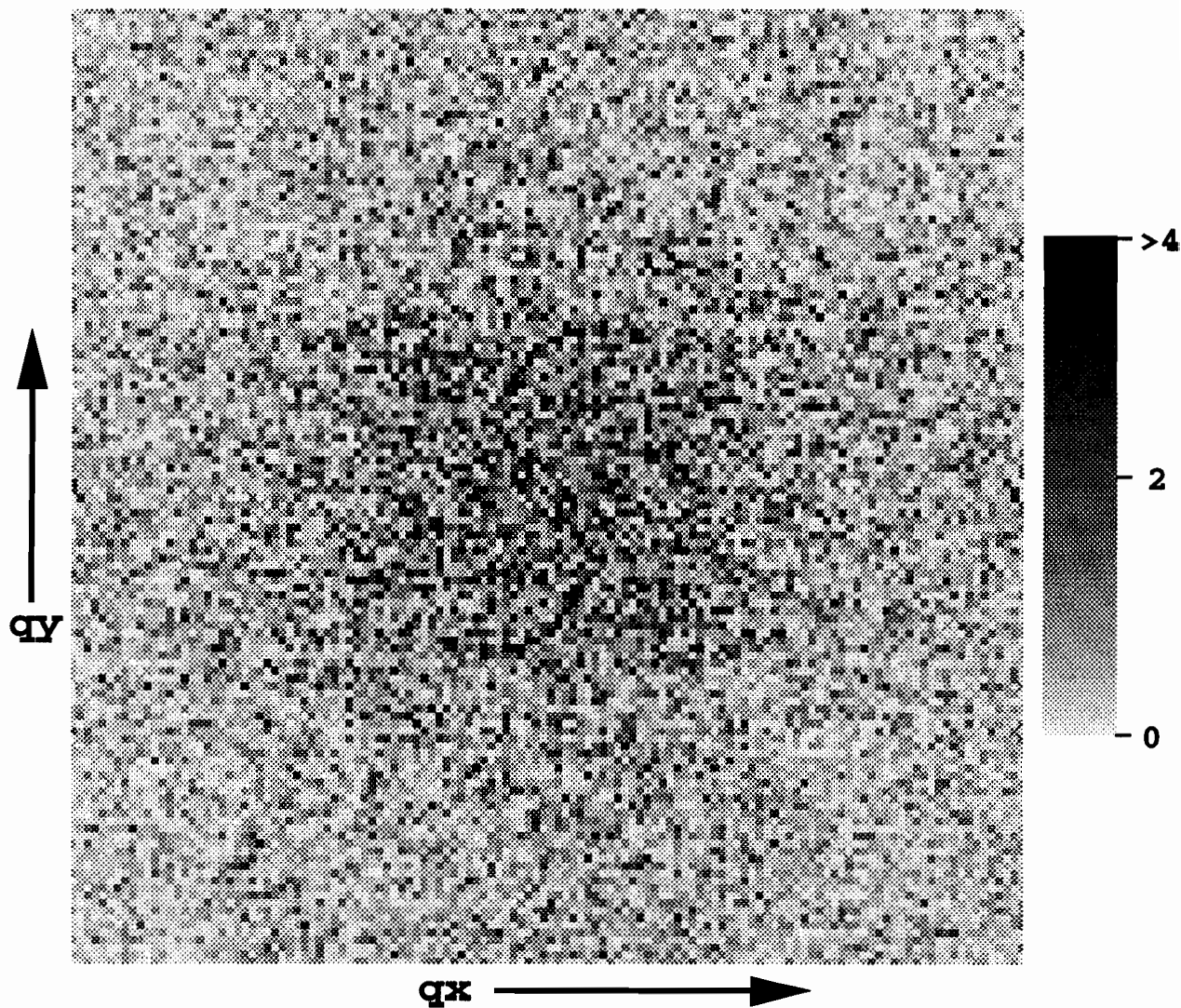


Figure 2.8: The instantaneous structure factor $S(\vec{q}, t)$ for a typical binary alloy below T_c for a given time t . A linear grey scale between 0 and 4 is used to display $S(\vec{q}, t)$. A slice through the origin of reciprocal space is shown in Fig. 2.9. The large spatial fluctuations with a characteristic length of 1 pixel are speckles, caused by the short range order equilibrium fluctuations. In a typical incoherent scattering experiment, the large spatial fluctuations disappear, and one observes that $S(\vec{q})$ is a smoothly varying function of \vec{q} , independent of the exact atomic arrangement. The coherent illumination allows one to measure the time fluctuations of the structure factor in equilibrium by studying the time fluctuations of the speckle pattern.

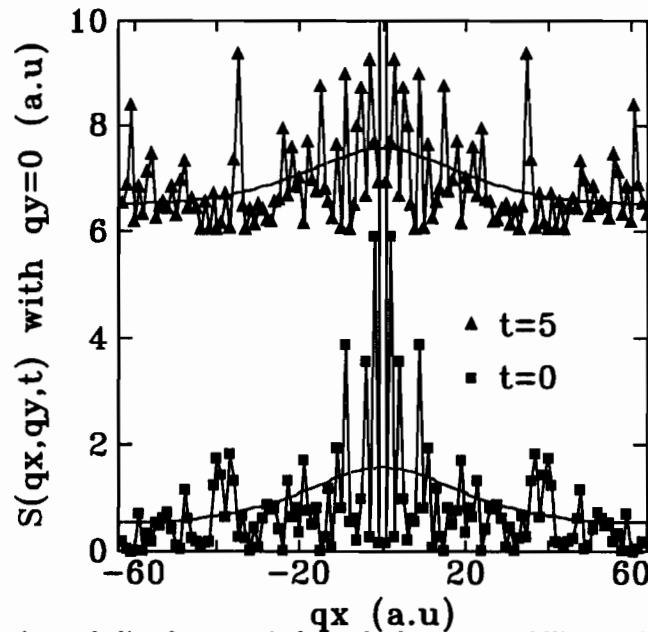


Figure 2.9: An horizontal slice for $q_y = 0$ through the center of Fig. 2.8 is shown with squares. The ensemble averaged structure factor defined in Eq. 2.32, observed in a typical incoherent experiment, is shown for comparison. The Bragg peak corresponding to the long range order is not seen because it is four orders of magnitude larger than the short range order diffuse peak. The structure factor at a later time $t = 5$ is also shown with triangles. A constant of 6 was added to the second slice for clarity. The speckle patterns shown differ because they depend on the exact arrangement of the atoms in the scattering volume which changes in time.

Note the large contrast in the structure factor. The most probable value is zero! The spatial fluctuations of $S(\vec{q}, t)$ are as large as the ensemble averaged structure factor shown with a smooth solid line.

Fig. 2.8 and 2.9 show that the structure factor of a material with a random atomic configuration is also *random*! It is a well known property of the structure factor¹ in Eq. 2.10. For many people, this may come as a surprise, but this is observed regularly in light scattering experiments, and was first observed more than a century ago in the light scattering from small particles [3, 4, 5]! This effect is the same one that causes laser speckle from reflected or transmitted light on the rough surfaces of optical elements [6]. It is not observed in standard X-ray or neutron scattering experiments because the beam is incoherent. In general, the speckle contrast is lost because the sample is illuminated by many coherence volumes, or because the detector

¹For example, on page 552 of Numerical Recipes [62], it is shown that the standard deviation of the power spectrum is equal to its average. Since the structure factor is the power spectrum for spatial fluctuations, the fluctuations in the structure factor are as large as their average! Crystallographers have also derived an exponential probability distribution of $S(\vec{q})$ for random reciprocal vectors [63].

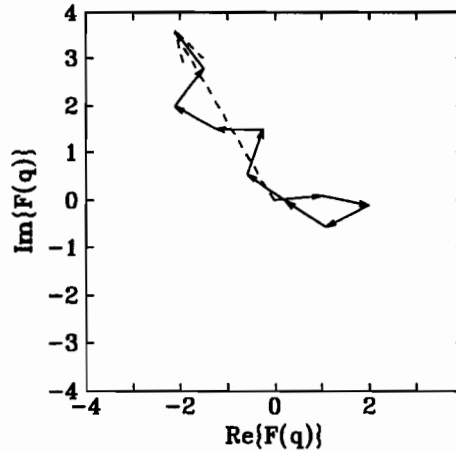


Figure 2.10: The complex scattering amplitude $F(\vec{q}) = \sum_i f_i e^{-\vec{q} \cdot \vec{r}_i}$ for ten atoms for a given \vec{q} , based on Fig. 4.2 in Ref [39]. As the number of atoms goes to infinity, the real and imaginary parts of $F(\vec{q})$ become independent Gaussian random variables. The dashed line is the resulting scattering amplitude, and the square of its magnitude is the structure factor $S(\vec{q})$.

resolution is insufficient to see the phenomena.

A speckle pattern is caused by coherent diffraction from random inhomogeneities in the material adding constructively or destructively, yielding a random structure factor. The speckle pattern is associated with the exact spatial arrangement of atoms in the scattering volume. This makes the structure factor sensitive to the individual realizations of a given statistical ensemble of atomic arrangements. This sensitivity is shown clearly in Fig. 2.9 since the speckle pattern for time $t = 0$ completely differs from the speckle pattern at later time $t = 5$.

Note also that if the crystal is perfectly ordered, the scattering is narrow and strong but only one speckle is observed. If the scattering is broad, many speckles are observed but the intensity of each speckle is small. For example, Fig. 2.9 is a sum of a narrow and broad component. The Bragg peak at $\vec{q} = 0$ subtends only one speckle. The scattering from the short range order fluctuations subtends many speckles, but its structure factor is four orders of magnitude smaller than the Bragg peak.

A speckle pattern is characterized by large spatial fluctuations from the ensemble average. This property follows from the definition of the structure factor in Eq. 2.15. We can represent Eq. 2.15 as a sum of random vectors in the complex plane. This is shown in Fig. 2.10 using ten atoms. Assuming that the phase factor $\vec{q} \cdot \vec{r}_i$ samples

uniformly a range of phase difference from 0 to 2π , one can show [64], by invoking the central limit theorem, that the real and imaginary part of the complex scattering amplitude are *independent* Gaussian random variables. Since $S(\vec{q})$ is the sum of the squares of the real and imaginary scattering amplitudes, which are two independent Gaussian random variables, it can be shown¹ that $\rho(S)$ follows a negative exponential probability distribution

$$\rho(S(\vec{q})) = \frac{\exp(-S/\overline{S(\vec{q})})}{\overline{S(\vec{q})}}. \quad (2.34)$$

This distribution has a large *contrast*² defined as the ratio of its rms fluctuations over its average, $\sigma_S/\overline{S} = 1$.

By observing the structure factor at a given wavevector, one can measure the equilibrium fluctuations of the alloy. This is shown in Fig 2.11(a). Note the large fluctuations of the structure factor as a function of time. The amplitudes of the time fluctuations are as large as the average scattering. The structure factor fluctuates in time with a characteristic time scale which can be determined by the time correlation function of the time dependent structure factor. By calculating the time correlation function of $S(\vec{q}, t)$,

$$g_2(\vec{q}, \tau) - 1 = \frac{\langle S(\vec{q}, t)S(\vec{q}, t + \tau) \rangle_t - \langle S(\vec{q}, t) \rangle_t^2}{\langle S(\vec{q}, t) \rangle_t^2}, \quad (2.35)$$

we can measure the characteristic time of the fluctuations.

Fig 2.11(b) shows g_2 for four given wavevectors. The time correlation function decays faster for larger $|\vec{q}|$, because short length scale fluctuations are intrinsically faster than long length scale fluctuations. The correlation functions shown in Fig. 2.11(b) were fitted to exponential decays $g_2(\tau) - 1 = \exp(-\tau/\tau_c)$. The inverse of the fitted correlation time is shown in Fig. 2.11(c), where $1/\tau_c = 4 + 2q^2$. One expects the structure factor fluctuations to decay with $1/\tau_c = M(2q^2 - 4r)$ below T_c , and $1/\tau_c = M(2q^2 + 2r)$ above T_c . The factor two comes from the fact that we are measuring intensity fluctuations and not amplitude fluctuations³. This is the expected result for light with a

¹See section A.1 for more details on the probability distribution of speckle.

²See for example section 4.2 in Goodman [39] or section 5.9 in Frieden [64].

³This factor of two is present in *homodyne* scattering. Homodyne refers to a scattering condition where the scattered beam interferes with itself. See Ref. [12], page 60 for more detail.

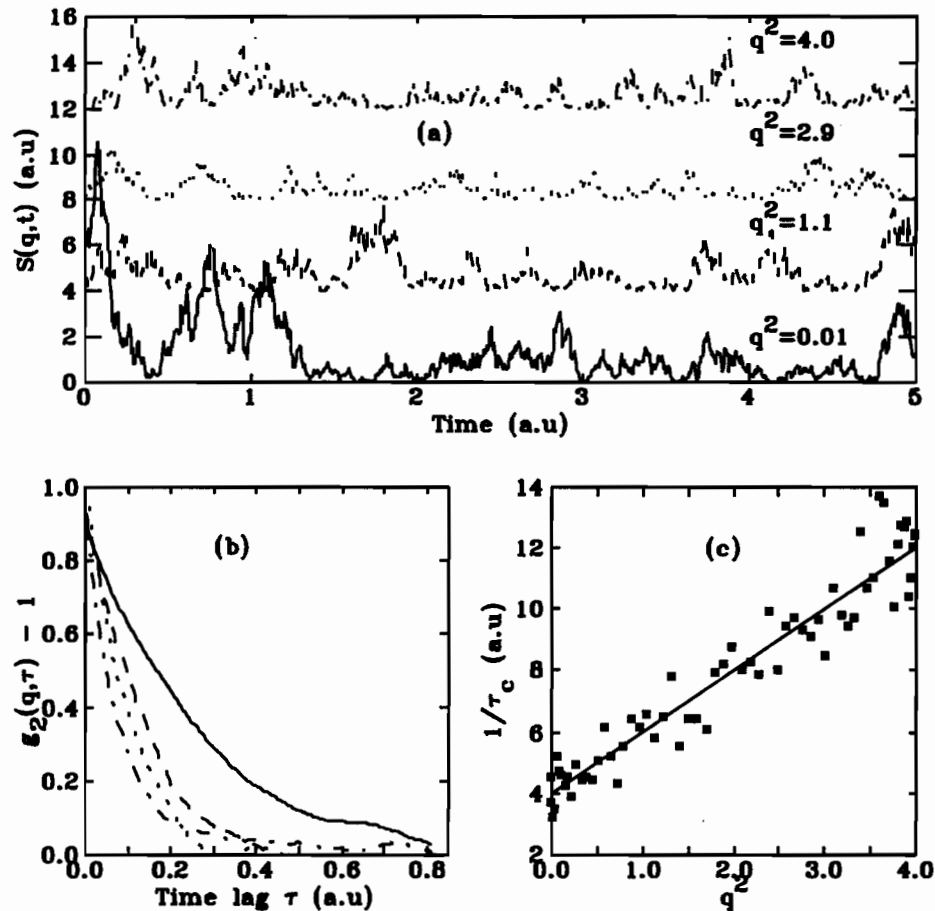


Figure 2.11: (a) The time fluctuation of the equilibrium structure factor displayed for four different wavevectors. The simulation was performed with the thermodynamic constants $\kappa = -r = w = M = 1$. In order to distinguish each wavevector, a constant (4,8,12) was added to the slices at increasing wavevectors. In an incoherent experiment, only the ensemble average is observed, thus the structure factor is constant in time. With coherent illumination, the structure factor at the four chosen wavevectors fluctuates in time with a characteristic time τ_c , which can be measured by a time correlation function defined in the text, and shown in (b). The characteristic time for the smallest wavevector (solid line) is 0.255, while it is 0.07 for the largest wavevector (dot-dashed line). The early decay of g_2 was fitted to $g_2(\tau) - 1 = \exp(-\tau/\tau_c)$. (c) The inverse of the least-squares fit correlation time $1/\tau_c$ versus q^2 . As discussed in the text, it clearly fits $4 + 2q^2$.

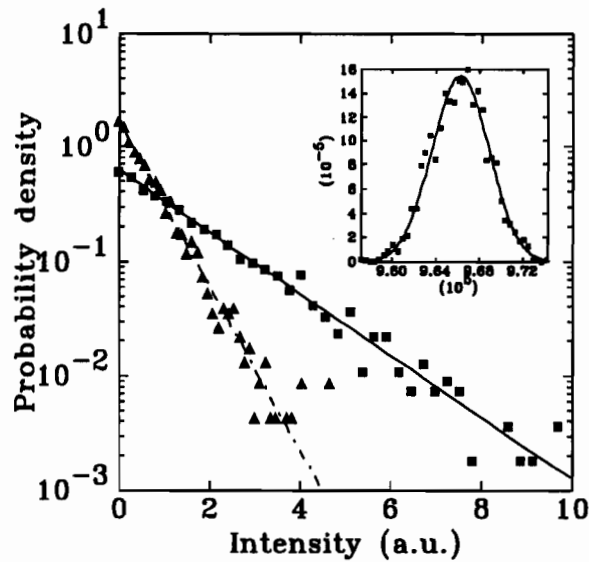


Figure 2.12: The probability density of the scattered intensity $S(\vec{q})$ for a binary alloy in equilibrium below T_c . $S(\vec{q})$ was simulated with model A. The squares and triangles are respectively the probability density of $S(\vec{q})$ for the smallest and largest \vec{q} in Fig 2.11. The simulation results are in perfect agreement with the exponential distributions drawn with solid and dot-dashed lines, discussed in the text. An exponential distribution implies that $S(\vec{q})$ is non-self-averaging. The inset shows that the probability density of $S(\vec{q} = 0)$ is nearly Gaussian, showing the scattered intensity self-averages for $\vec{q} = 0$.

Lorentzian spectrum. Here $r = -1$, $M = 1$, $\kappa = 1$, in agreement with the fits. For systems with a conserved order parameter where the intensity fluctuations are caused by diffusion, the inverse of the correlation time $1/\tau_c = 2q^2 M(r + \kappa q^2)$ above T_c . The extra q^2 dependence comes from the added conservation law.

Fig 2.12 shows the equilibrium probability density of the scattered intensity, $\rho(S)$, calculated for model A below T_c . The probability density of $S(\vec{q})$ for two wavevectors is shown. The solid lines are $\rho(S) = \frac{\exp(-S/\langle S \rangle)}{\langle S \rangle}$, where $\rho(S)$ and the ensemble average of the equilibrium intensity, $\langle S \rangle$, are calculated over 2^{14} independent measurements of $S(\vec{q}, t)$, separated from each other by several correlation times. As discussed above, the scattered intensity in equilibrium is non-self-averaging¹ for $\vec{q} \neq 0$. Note that although the order parameter in equilibrium is self-averaging [65], the scattered intensity is not.

As shown in the inset of Fig 2.12, the probability density of $S(\vec{q} = 0)$ is well

¹A thermodynamic variable whose relative fluctuations vanish in the thermodynamic limit is called self-averaging. Here the time fluctuations of $S(q, t)$ are as large as the time average of $S(\vec{q})$ even in the thermodynamic limit.

fitted to a Gaussian, with $\rho(S) = \frac{\exp(-0.5(S - \langle S \rangle)^2 / \sigma_S^2)}{\sqrt{2\pi\sigma_S^2}}$, where the standard deviation of the scattered intensity $\sigma_S = 2583$, and the average intensity $\langle S \rangle = 96622$ is calculated from the data. Recall that $S(\vec{q} = 0) = (\int \psi(\vec{r}) d\vec{r})^2 = M^2$, where M is the magnetization of the system. The magnetization is an extensive quantity that self-averages [65]. In equilibrium, once the system has chosen one of its two possible phases, the relative fluctuations of the magnetization are quite small, and vanish in the thermodynamic limit. This explains the sharp probability density of $S(\vec{q} = 0)$.

In thermal equilibrium above T_c , where the average magnetization is zero, it can be shown relatively easily that

$$\rho(S) = \begin{cases} \frac{1}{\bar{S}} \exp(-\frac{S}{\bar{S}}), & \text{for } \vec{q} \neq 0 \\ \frac{1}{\sqrt{2\pi S \bar{S}}} \exp(-\frac{S}{2\bar{S}}), & \text{for } \vec{q} = 0, \end{cases} \quad (2.36)$$

where \bar{S} is the equilibrium structure factor found in Eq. 2.32. In the derivation of Eq. 2.36 for $\vec{q} = 0$, one uses the facts that the probability density of M is a Gaussian centered at zero, and that $\int_0^\infty \rho(S) dS = \int_{-\infty}^\infty \rho(M) dM$. At $\vec{q} = 0$, this probability distribution has an average \bar{S} , and a standard deviation $\sqrt{2\bar{S}}$. Above T_c , the fluctuations of $S(\vec{q})$ do not vanish in the thermodynamic limit.

The previous figures in this section have shown the statistics of the instantaneous scattered intensity, $S(\vec{q}, t)$. In all scattering experiments, the structure factor must be integrated over some exposure time τ , and over some volume in reciprocal space. Both spatial and temporal resolution affect the statistics of the measured intensity.

Let us first study the effect of integrating the scattered intensity over some arbitrary exposure time. The time-averaged structure factor is defined by

$$\overline{S(\vec{q}, t)} = \int_0^\tau S(\vec{q}, t + t') dt'. \quad (2.37)$$

Fig 2.13 shows the ratio of the rms fluctuations of \bar{S} , $\sigma_{t, \bar{S}}$, over the ensemble average of \bar{S} , $\langle \overline{S(\vec{q}, t)} \rangle_t$, as a function of q^2 for several τ 's. Here the ensemble average of \bar{S} is calculated by

$$\langle \overline{S(\vec{q}, t)} \rangle_t = \frac{1}{N} \sum_{i=1}^N \overline{S(\vec{q}, t_i)}, \quad (2.38)$$

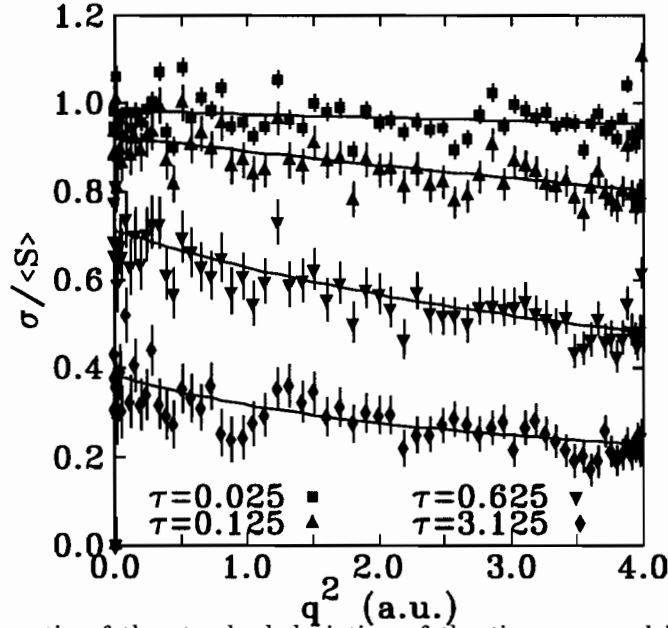


Figure 2.13: The ratio of the standard deviation of the time-averaged intensity \bar{S} over the ensemble average. The data in Fig 2.11b were integrated over different exposure times $\tau = 0.025, 0.125, 0.625, 3.125$. Then \bar{S} was ensemble averaged to calculate its mean and variance. The error bars were calculated with Eq. A.32, derived from standard error analysis.

and the variance of \bar{S} , by

$$\sigma_{t,\bar{S}}^2 = \frac{1}{N-1} \sum_{i=1}^N \left(\overline{S(\vec{q}, t_i)} - \langle \overline{S(\vec{q}, t)} \rangle_t \right)^2, \quad (2.39)$$

where $i = 1, 2, 3, \dots, N$, and $t_{i+1} - t_i = \tau$. In Fig 2.13, the integration times used to calculate $\overline{S(\vec{q}, t)}$ are $\tau = 0.025, 0.125, 0.625, 3.125$.

For small exposure times, $\tau \ll \tau_c$, the probability density of \bar{S} is nearly equal to the probability density of the instantaneous intensity $S(t)$. This is shown in Fig. 2.13, since $\sigma_{\bar{S}} / \langle \bar{S} \rangle$ is nearly equal to the ratio for the instantaneous intensity $\sigma_S / \langle S \rangle = 1$ for the data with $\tau = 0.025$. For larger exposure times the ratio departs from unity, and one can show¹ asymptotically for $\tau \gg \tau_c$ that

$$\sigma_{t,\bar{S}} / \langle \bar{S} \rangle_t \approx \sqrt{2\tau_c / \tau}. \quad (2.40)$$

Note that the ratio $\tau / \tau_c = N_c$, the number of coherence times in one exposure time. Eq. 2.40 states that the second moment of the integrated intensity follows the central limit theorem for large τ , since $\sigma_{t,\bar{S}} / \langle \bar{S} \rangle_t \propto 1 / \sqrt{N_c}$. The solid line in Fig 2.13 is the

¹The treatment in this section follows closely section 6.1 in Goodman [39]. The factor two in Eq. 2.40 and 2.41 is due to our definition of the correlation time in Fig. 2.11.

exact treatment found in Goodman [39] for a Lorentzian spectrum, valid for any τ , where

$$\frac{\sigma_{t,\bar{S}}}{\langle S(\vec{q}, t) \rangle_t} = \left(\frac{2\tau_c}{\tau} + \frac{1}{2} \left(\frac{2\tau_c}{\tau} \right)^2 [\exp(-\tau/\tau_c) - 1] \right)^{\frac{1}{2}}. \quad (2.41)$$

The agreement between the simulation results and Eq. 2.41 is excellent and well within error¹. The wavevector dependence is due to the q -dependence of the correlation time, which ranges from 0.25 to 0.125 for q^2 between 0 and 4 (see Fig 2.11). Finally, note that the point at the origin is due to the long range order peak which is self-averaging, thus $\sigma/\langle S \rangle = 0.0$.

Finally, in any coherent scattering experiment, the detector area may average several speckles. This averaging reduces the spatial contrast of the speckle pattern. In section A.1, it is shown that the probability distribution of the spatially averaged scattered intensity sharpens when N speckles are averaged in a given detector area. The resulting spatial contrast of the scattered intensity is reduced from one, for perfect resolution, to $1/\sqrt{N}$ for poorer resolution. Spatial averaging is often used in optics to remove speckle from images obtained by the reflection of light on a rough surface.

¹Some approximate expressions are derived in the first appendix on how to calculate the error bars for different functions of the estimated mean and variance. Here, the error bars were derived in Eq. A.32. The error bars calculated in Eq. A.32 represent quite accurately the random error caused by evaluating the average and variance with a finite N .

CHARACTERIZATION OF POSITION-SENSITIVE DETECTORS

The advent of high intensity X-ray synchrotron sources coupled with the development of X-ray position-sensitive detectors (PSD) has allowed us to study time-resolved non-equilibrium dynamics in solid-state systems. For example, one-dimensional PSD have been used to study the isothermal crystallization of metallic glasses by measuring structure factors with a time resolution of a few milliseconds [66], and to study the early stage dynamics of order-disorder transitions in Fe_3Al [67] and Cu_3Au [10]. Two-dimensional PSD have been used to study the dynamics of a first order phase transition in Cu_3Au with coherent X-rays [15, 21, 25] and to determine strain kinetics in $\text{In}_x\text{Ga}_{1-x}\text{As}$ quantum wells [68].

To obtain meaningful quantitative data from a PSD, one must know whether the response of the detector is linear with respect to the number of incident photons, measure the uniformity of response over the detector area, and determine the noise, the resolution function, and the detective quantum efficiency. For coherent diffraction experiments [15, 25], the full spatial resolution of the detector is required, and spatial and temporal correlation of the signal are the quantities to be measured. Thus correlations inherent to the detector have to be exactly known.

In this chapter, we show how the response of a PSD can be characterized by comparing measured averages, variances and pixel-to-pixel correlation functions to the expected statistical estimators for Poisson counting statistics. Similar techniques have been used previously to measure the detective quantum efficiency of a detector [69, 70], or to evaluate the linearity constant between the PSD signal and the number of detected photons [71, 72]. Significant spatial correlation exists between neighboring

pixels for a typical PSD (see Fig. 3.2 and 3.10). We show how to extract the resolution from the measured correlation function. The effect of a finite detector resolution, which induces spatial correlations between neighboring pixels of a PSD, reduces the noise of the PSD when compared to expected Poisson noise. This must be taken into account in the evaluation of the detective quantum efficiency.

In section 3.0.3, we first discuss the case where each pixel of the detector is independent of its neighbors. Then, we generalize this technique to include the spatial correlation that may be present in a real one- or two-dimensional detector. Finally, two examples are given: section 3.0.4 gives the characterization of a X-ray sensitive linear photodiode array similar to the one used previously in our group [10, 66, 67], and section 3.0.5 describes a more general treatment for the two-dimensional charge coupled device (CCD) used in this work. This section is the first detailed study of the spatial resolution function of position-sensitive detectors (PSD) in our group. It was published recently [37].

3.0.3 *Description of the technique*

Description of the detection process

Solid-state PSD are typically made of an array of Si photodiodes or MOS capacitors, which can be used as integrating detectors for X-rays. Two modes of operation of solid-state X-ray detectors are generally used: direct X-ray illumination or optical coupling using light produced in an X-ray fluorescent material. Direct illumination of the detector gives the full spatial resolution of the pixels, while optical coupling increases the detective quantum efficiency for harder X-rays and allows for changes in the effective detector area by appropriate lenses. In this thesis, we use direct illumination of the PSD. For silicon, 3.6 eV are required to create an electron-hole pair [73]. A photon in the range of 5-20 keV will generate thousands of electron-hole pairs, some of which are then collected on the Si diode capacitance. After a preset exposure time τ , the collected charge is measured, amplified, digitized and finally cleared for the next integration. The digitized signal $V(\vec{r}, t)$ is an integer

number measured in analog-to-digital units (ADU). Here \vec{r} is a discrete one- or two-dimensional vector pointing to the center of a given pixel of the PSD, and t refers to the integration between time t and $t + \tau$. The variables used are summarized on page IX. The number of ADU per detected photon is determined by the gain of the digitizer circuit. A so-called dark pattern must be taken without illumination to subtract an offset signal from the data, which may vary from pixel to pixel. To relate the detected signal to the incident intensity, one has to measure the detector linearity, uniformity, noise, resolution and detective quantum efficiency.

Illuminating the detector with a spatially uniform source of light or X-rays allows one to test the uniformity of the detector response. To generate this uniform source, we scatter a beam of monochromatic X-rays from an amorphous sample (e.g. a piece of polyimide[71, 74] or polystyrene) and place the detector far away from the sample.

To test linearity, one varies the incident flux of photons and the integration time independently to see whether the number of photons incident on the surface of pixel \vec{r} , integrated between t and $t + \tau$, $n_i(\vec{r}, t)$, is the only relevant quantity. One must find a function that relates the detected signal V to n_i so that $V = f(n_i)$. In general, f may not be linear. Therefore to linearize the detector's signal, one would apply the inverse of f to V . Details of this treatment are given in section 3.0.5.

We assume that the noise in the signal V has two sources: counting statistics of the photons and an "electronic" noise from the detection process. Naturally, the noise due to counting statistics depends on n_d , the number of detected photons, rather than on n_i . In general $\langle n_d(\vec{r}, t) \rangle_t = \alpha(\vec{r}) \langle n_i(\vec{r}, t) \rangle_t$, where $\alpha(\vec{r})$ is called the detective quantum efficiency of a pixel centered at \vec{r} , as defined in Ref. [69, 70]. Here the brackets refer to a time average. One finds that $\alpha < 1$ because photons are absorbed or reflected before they reach the detection volume, or because they pass the detection volume without detection. We show how $n_d(\vec{r}, t)$ may be determined by analyzing the fluctuations in the signal $V(\vec{r}, t)$ for equivalent exposures.

Technique for characterizing independent linear detectors

The detector characterization technique is based on the following idea. Due to the nature of the detection process, n_d obeys Poisson statistics, so the mean and variance of n_d are equal. (see Appendix A.1) If we assume linearity and neglect any electronic noise contribution from the detector electronics, the signal in a detector is given by $V = kn_d$, where k is the calibration constant, equal to the average number of ADU per detected photon. By measuring N patterns, we can calculate the signal mean and variance from their definitions on page IX. $\langle V \rangle_t = k \langle n_d \rangle_t$ is the mean signal. The variance of V , $S_{t,V}^2$, is equal to $k^2 S_{t,n_d}^2$, and for Poisson noise, $S_{t,n_d}^2 = \langle n_d \rangle_t$. So the ratio $S_{t,V}^2 / \langle V \rangle_t = k$ allows us to measure the calibration constant. Unless otherwise stated, the terms mean and variance used in this paper refer to the unbiased estimators of the true mean and variance of a given variable. Here we assumed that the signal V in a given pixel is independent of the signal in its nearest neighbors, and that the standard deviation of the number of photo-electrons created per detected photon is much smaller than its average [71]. What follows is a generalization of this idea by considering other noise sources and couplings between detectors.

For a real PSD, we found that the ratio k increases as $\langle V \rangle_t$ approaches zero, due to electronic noise contributions to the variance. This intensity dependence can be removed by including in V the detected photons and the electronic noise contributions so that

$$V(\vec{r}, t) = k(\vec{r})n_d(\vec{r}, t) + V_e(\vec{r}, t), \quad (3.1)$$

and on average

$$\langle V(\vec{r}, t) \rangle_t = k(\vec{r}) \langle n_d(\vec{r}, t) \rangle_t. \quad (3.2)$$

Note that here the value of k may vary between different pixels. V_e is the electronic noise signal, and we assumed $\langle V_e \rangle_t \approx 0$, which is assured by the subtraction of the dark pattern described earlier. We assume both V_e and n_d are independent random variables. The physics of this noise is discussed in detail elsewhere [70]. Here we are only interested in the mean and variance of the noise, which are measured separately

with the source of X-rays turned off. The time averaged variance of $V(\vec{r}, t)$ is

$$S_{t,V}^2(\vec{r}) = k^2(\vec{r})S_{t,n_d}^2(\vec{r}) + S_{t,V_e}^2(\vec{r}) + 2k(\vec{r})\text{cov}_t(n_d(\vec{r}, t), V_e(\vec{r}, t)), \quad \text{where} \quad (3.3)$$

$$\text{cov}_t(A, B) = \frac{1}{N-1} \sum_{i=1}^N (A(t_i) - \langle A \rangle_t)(B(t_i) - \langle B \rangle_t) \quad (3.4)$$

is the covariance of two random variables A and B . From the assumption of independence, $\text{cov}_t(n_d, V_e) \approx 0$. Dividing Eq. (3.3) by Eq. (3.2), and recalling that $S_{t,n_d}^2(\vec{r}) = \langle n_d(\vec{r}, t) \rangle_t$ for a Poisson distribution (see Appendix A.1), one finds that

$$k(\vec{r}) = \frac{S_{t,V}^2(\vec{r}) - S_{t,V_e}^2(\vec{r})}{\langle V(\vec{r}, t) \rangle_t}. \quad (3.5)$$

To determine an estimate of the ratio of ADU to detected photons for each pixel, one evaluates the mean and variance for each pixel based on N scans, subtracting a measured dark variance S_{t,V_e}^2 from the signal variance. The subtraction of S_{t,V_e}^2 in Eq. (3.5) makes the ratio k intensity independent for a real PSD, as the average signal goes to zero. Once $k(\vec{r})$ is known, $\alpha(\vec{r})$ can be calculated after measuring $n_i(\vec{r}, t)$ with a detector with near unit quantum efficiency. The detective quantum efficiency may then be calculated as

$$\alpha(\vec{r}) = \frac{\langle V(\vec{r}, t) \rangle_t}{k(\vec{r}) \langle n_i(\vec{r}, t) \rangle_t}. \quad (3.6)$$

The spatial variations of the detector array appear as variations in $k(\vec{r})$, or detector to detector variations. In order to determine whether these fluctuations are significant, the error in $k(\vec{r})$ expected from Poisson and electronic noise has to be considered. The uncertainty in the determination of $k(\vec{r})$ depends on the number of measurements N . From standard error propagation analysis (see the derivation in the Appendix), we estimate the expected error in k , $\sigma_k(\vec{r})$, by

$$\frac{\sigma_k^2(\vec{r})}{k^2(\vec{r})} \approx \frac{2}{N-1} \left(1 + \frac{S_{t,V_e}^4(\vec{r})}{k^2(\vec{r}) \langle V(\vec{r}, t) \rangle_t^2} \right) + \frac{S_{t,V_e}^2(\vec{r})}{\langle V(\vec{r}, t) \rangle_t^2} \left(\frac{1}{N} + \frac{1}{N_d} \right). \quad (3.7)$$

Here, we used $S_{t,V}^2 - S_{t,V_e}^2 = k \langle V \rangle_t$ to simplify Eq. (A.30). N_d is the number of scans used to determine the average dark pattern. Eq. (3.7) is made of four terms: the first term $2/(N-1)$ is the error due to counting statistics (see Eq. (A.27)) and the last three terms containing S_{t,V_e}^2 and S_{t,V_e}^4 are due to the electronic noise.

To minimize the error, one should take N as large as possible to reduce the error due to counting statistics. This is achieved by taking a small exposure time τ . As τ and V approaches zero, the minimum error is reached when both noise contributions to σ_k are equal. For smaller τ , σ_k increases due to the electronic noise. As a rule of thumb, one should measure $N_d = N$ dark patterns, so that the average dark pattern is measured precisely. To get a relative precision $\epsilon = \sigma_k/k$, one should choose τ such that the detected signal $V \approx \sqrt{S_{t,V_e}^2 \{1 + S_{t,V_e}^2/k^2\}}$, and measure $N \approx 4/\epsilon^2$ scans with and without X-rays.

For count rates available at synchrotron sources, one may find that the signal obtained for the finest time resolution τ is always much larger than the dark noise. Then fewer dark patterns need to be measured. For large signals $\langle V \rangle_t \gg \sqrt{S_{V_e}^2}$ and for $N \gg N_d$, $\sigma_k \approx k\sqrt{2/(N-1) + S_{V_e}^2/(N_d\langle V \rangle_t^2)}$. When $\langle V \rangle_t \gg V_m = \sqrt{S_{V_e}^2 N/(2N_d)}$, $\sigma_k \approx k\sqrt{2/(N-1)}$, and counting statistics is the dominant contribution to the error. In Fig. 3.1b for example, the signal in the central pixels of the array is within this limit since $V_m = 66$ ADU. For $V < V_m$, σ_k is dominated by the detector electronic noise.

As mentioned above, this treatment assumed that each pixel is independent of its neighbors. If this is not true, this correlation reduces the variance, and $k(\vec{r})$ is not the number of ADU per detected photon. This case is discussed next.

Treatment including pixel-to-pixel correlations

To understand the effect of couplings between detectors, we consider first a toy model for a one-dimensional PSD, where two neighboring pixels share some fraction x of their signals. Following the previous notation, replacing \vec{r} by an integer index i , the signal in the i th pixel, $V(i, t)$, is defined by

$$V(i, t) = (1 - x)kn_d(i, t) + xkn_d(i + 1, t), \quad (3.8)$$

where k is the number of ADU per detected photon, and $n_d(i, t)$ is the number of photons measured by an independent detector if x was zero, and it is assumed that $0 \leq x \leq 0.5$. The case for $x \neq 0$ occurs in real PSD because the charge created by

photons is shared by adjacent pixels. This coupling affects the statistics of the signal. For a spatially uniform exposure, $\langle n_d(i, t) \rangle_t$ and $\langle n_d(i+1, t) \rangle_t$ are the same within counting statistics, and $\langle V(i, t) \rangle_t$ equals on average $k\bar{n}_d$, where \bar{n}_d is the mean of the probability density of n_d . For two independent Poisson distributed random variables, $n_d(i, t)$ and $n_d(i+1, t)$, with $\langle n_d(i, t)n_d(i+1, t) \rangle_t = \langle n_d(i, t) \rangle_t \langle n_d(i+1, t) \rangle_t = \bar{n}_d^2$, the variance of $V(i, t)$ is

$$S_{i,V}^2(i) = \langle V(i, t)^2 \rangle_t - \langle V(i, t) \rangle_t^2 = k^2 \{ (1-x)^2 + x^2 \} \bar{n}_d. \quad (3.9)$$

By letting $x = 0$, we recover the case discussed in section 3.0.3. For a finite x , the variance is always smaller than the variance of uncoupled detectors as $(1-x)^2 + x^2 \leq 1$ for $0 \leq x \leq 0.5$. Now $S_{i,V}^2(i)/\langle V(i, t) \rangle_t = k\{(1-x)^2 + x^2\}$, so that from a measurement of this ratio alone, k cannot be extracted. A second measurement is needed in order to solve for k and x .

The resolution function could be measured to determine x , by illuminating only one pixel with a source which is smaller than the pixel size. For a PSD, this requires collimating the X-ray beam through a pinhole with a diameter of only a few micrometers, and scanning the pinhole over the detector area. This technique may be difficult to apply, because one needs an intense X-ray source to generate a usable micrometer beam and a translation system with micrometer resolution. The measurements of pixel-to-pixel correlation offer a useful alternative for measuring the resolution function. In this model, the measured covariance of $V(i, t)$ and $V(i+1, t)$ is given by

$$\begin{aligned} \text{cov}_t(V(i, t), V(i+1, t)) &= \langle V(i, t)V(i+1, t) \rangle_t - \langle V(i, t) \rangle_t \langle V(i+1, t) \rangle_t \\ &= x(1-x)k^2\bar{n}_d, \end{aligned} \quad (3.10)$$

which gives $k = (2\text{cov}_t + S_{i,V}^2)/\langle V \rangle_t$ and $x = 1/2 - 1/2\sqrt{(S_{i,V}^2 - 2\text{cov}_t)/(S_{i,V}^2 + 2\text{cov}_t)}$.

Next nearest neighbor pixels can also be coupled due to the diffusion of photoelectrons far away from the absorption site. To measure these distant correlations, a

general correlation function between $V(\vec{r}, t)$ and $V(\vec{r} + \vec{\Delta}, t)$ is defined as

$$C(\vec{r}, \vec{\Delta}) = \frac{\text{cov}_t(V(\vec{r}, t), V(\vec{r} + \vec{\Delta}, t))}{\sqrt{S_{i,V}^2(\vec{r})S_{i,V}^2(\vec{r} + \vec{\Delta})}}, \quad (3.11)$$

where the averages and variances are defined on page IX, and $\vec{\Delta}$ is the relative displacement between the pixels. Two limiting cases in this definition may be calculated easily. For large $\vec{\Delta}$, $V(\vec{r}, t)$ and $V(\vec{r} + \vec{\Delta}, t)$ are independent, and $C(\vec{r}, \vec{\Delta}) = 0$. For $\vec{\Delta} = 0$, $C(\vec{r}, 0) = 1$ since the numerator becomes identical to $S_{i,V}^2$. If the signal between neighbors is not independent, one finds in general $-1 < C(\vec{r}, \vec{\Delta}) < 1$.

To estimate the resolution function and its effect on the measured noise, we now include all pixel-to-pixel couplings. Developed for shot noise processes [64], the model describes a stochastic process created by random superposition of a constant response function $h(\vec{r}')$ for each photon¹. The function $h(\vec{r}')$ describes the spread of the signal in the detector. The measured signal at pixel \vec{r} , $V(\vec{r}, t)$, is a sum of disturbances which hit the detector at random positions \vec{r}_i ,

$$V(\vec{r}, t) = \sum_{i=1}^{n_d} h(\vec{r}_i - \vec{r}). \quad (3.12)$$

In our case, n_d is the number of detected photons between time t and $t + \tau$, sampled from a Poisson distribution. The \vec{r}_i are chosen from a uniform distribution since the signal is assumed to be spatially uniform. The model can be generalized to include spatial variations in the incident signal [64], and the results will not depend on the fact that h may vary with each photon if the variance of h is small enough. The model further assumes that $h(\vec{r}')$ is the same for each pixel and that the signal in a given detector is not correlated in time. A complete derivation of the moments of V is given in detail in Ref. [64]. It is shown that

$$\langle V(\vec{r}, t) \rangle_t = \langle n_d(\vec{r}, t) \rangle_t 1/L^d \int h(\vec{r}') d\vec{r}'^d, \quad (3.13)$$

¹In a real PSD, h may depend on where the photon is absorbed on the area of the pixel, and on how deep it is absorbed. Furthermore, the probability for a photon of being absorbed varies exponentially with depth. Here we assume the response h independent of the exact position of the photon absorption. This is the simplest model for describing the spread of the signal to several pixels. It could be generalized in a straightforward manner.

$$S_{t,V}^2 = \langle V^2(\vec{r}, t) \rangle_t - \langle V(\vec{r}, t) \rangle_t^2 = \langle n_d(\vec{r}, t) \rangle_t 1/L^d \int h^2(\vec{r}') d\vec{r}'^d, \quad (3.14)$$

$$C(\vec{r}, \vec{\Delta}) = \frac{\langle V(\vec{r}, t)V(\vec{r} + \vec{\Delta}, t) \rangle_t - \langle V(\vec{r}, t) \rangle_t^2}{S_{t,V}^2} = \frac{\int h(\vec{r}')h(\vec{r}' + \vec{\Delta}) d\vec{r}'^d}{\int h^2(\vec{r}') d\vec{r}'^d}, \quad (3.15)$$

where L^d is the linear size or area of a detector in $d = 1, 2$ dimensions. $\langle V(\vec{r}, t) \rangle_t$, $S_{t,V}^2$ and $C(\vec{r}, \vec{\Delta})$ can be estimated from repeated measurements, and $\langle n_d \rangle_t$ can be solved from these equations with an appropriate model for $h(\vec{r}')$. Choosing $h(\vec{r}') = k\delta(\vec{r}')$, we recover Eq. (3.5) from the ratio of Eq. (3.14) and (3.13). Here, the model is further simplified by assuming that $h(\vec{r}')$ is discrete, and replacing integrals by sums. To recover Eq. (3.9,3.10) from Eq. (3.13-3.15), let $h(0) = k(1 - x)$, $h(1) = kx$, and $h(\vec{r}') = 0$, for $|\vec{r}'| > 1$. Using the measured spatial autocorrelation function, one can often evaluate the resolution function $h(\vec{r}')$ by inverting Eq. (3.15). From Eq. (3.13), one can calculate n_d from $\langle V(\vec{r}, t) \rangle_t$. Then Eq. (3.6) becomes

$$\alpha = \frac{L^d \langle V \rangle_t}{\langle n_i \rangle_t \int h(\vec{r}') d\vec{r}'^d}. \quad (3.16)$$

Good statistics for the measured autocorrelation functions can be in principle obtained by correlating the signal from thousands of scans. If no time correlation exists and one expects the detectors to be almost identical, one can save this effort by taking a spatial average and variance over detectors of a single uniform scattering pattern instead of time averages. One can get excellent statistics from a single scan of a 500×500 CCD array by averaging over the 250000 pixels. In the two examples discussed next, direct measurements showed no time correlation of the signals. For our detectors, we found that a time average and a spatial average are quantitatively similar, both for means and variances. Time averages or spatial averages can thus be interchanged for convenience.

3.0.4 Characterization of a linear PSD

The photodiode array used contains 2048 rectangular pixels with $25\mu\text{m}$ wide and 2.0mm high active areas. The resolution is specified as 1.5 pixels wide so there will be some correlation between pixels. It is operated at -40°C , cooled by a Peltier stage, to reduce the electronic noise. The array is operated by a Princeton Instrument

	EG&G Reticon 2048SAU-822.	TI 4849 CCD.
Array size	2048 pixels.	390 by 584 pixels.
Pixel dimension	25 μ m wide, 2.0mm high.	22.4 \times 22.4 μ m.
Specified resolution	1.5 pixels.	2 pixels.
Characteristic length	diffusion length 50 μ m.	depletion layer 12 μ m.
Window	250 μ m Be window, 1 μ m SiO ₂ overcoat.	250 μ m Be window.
Amplifier gain	1 ADU/1300 electrons.	adjustable.
Readout time	4 μ s/pixel, 8ms for the array.	6 μ s/pixel, 1 s for the array.
Readout noise	< 1.2 ADU rms.	20 electrons/pixel.
Integration time	8ms to two hours.	a few μ s to minutes.

Table 3.1: Position-sensitive detector characteristics

ST1000 controller and the data were transferred to a IBM PC 386-AT through a custom designed I/O board from PI. Software is provided with the package to control the data acquisition parameters, store the data and visualize the data. Scans can be accumulated by a 32 bit register and pixels can be grouped to increase the scan rate while sacrificing the spatial resolution. Further characteristics of the detector are summarized in Table 3.1.

Fig. 3.1 shows some experimental data obtained for the linear array. As defined on page IX and Eq. (3.5), the mean, variance and ratio of variance over mean of V are plotted for every 20th pixels of the array at two different X-ray energies, 6.93 and 8.05 keV. The first data set was obtained by scattering 6.93 keV X-rays onto a Bragg peak of Fe₃Al, constant in time. 100 scattering patterns were averaged. Note that the mean is quite smooth (i.e well defined to within 0.3%) but that the fluctuations on the variance are substantial (14%). For $N = 100$ measurements, the relative error on the mean is $\frac{1}{\sqrt{Nn_d}}$ with $n_d \approx 1000$, while the relative error on the variance is $\sqrt{\frac{2}{N-1}}$. The error bars on the ratio were calculated from Eq. (3.7). A least squares fit of $k(\vec{r})$ to a constant, weighted with error bars calculated from Eq. (3.7), yields $k = 0.682$ and a χ^2 of 1.1.

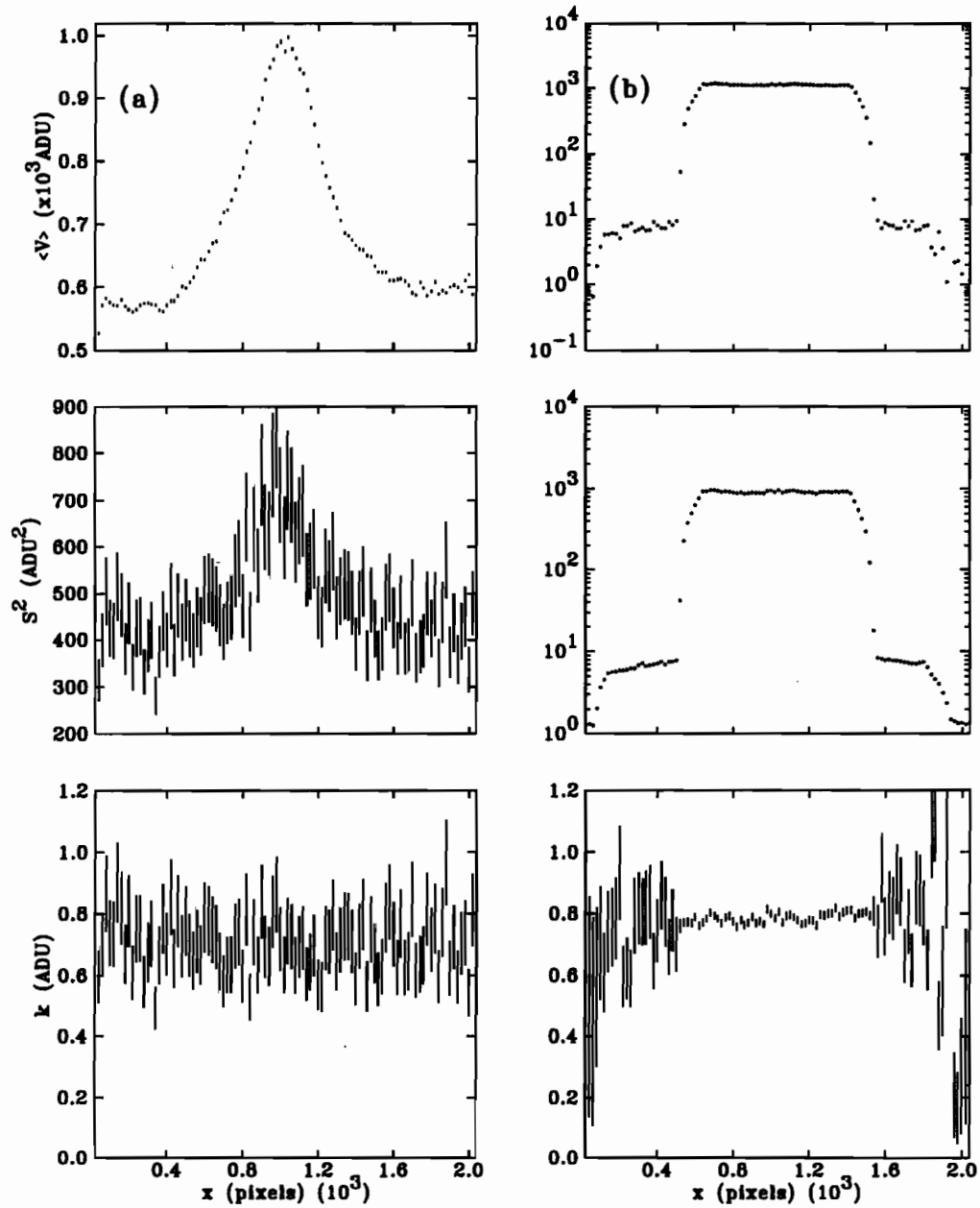


Figure 3.1: a) time averaged signal $\langle V(\vec{r}) \rangle_t$, variance $S_{t,V}^2(\vec{r})$, and calibration constant $k = S_{t,V}^2 / \langle V(\vec{r}) \rangle_t$ versus pixel number for 6.93 keV X-rays, $N = 100$, $N_d = 1$. The error bars for the mean, variance and ratio are calculated from formulas discussed in section 3.0.3 and the appendix. b) same as above, but with 8.05 keV X-rays, $N = 8000$, $N_d = 1$.

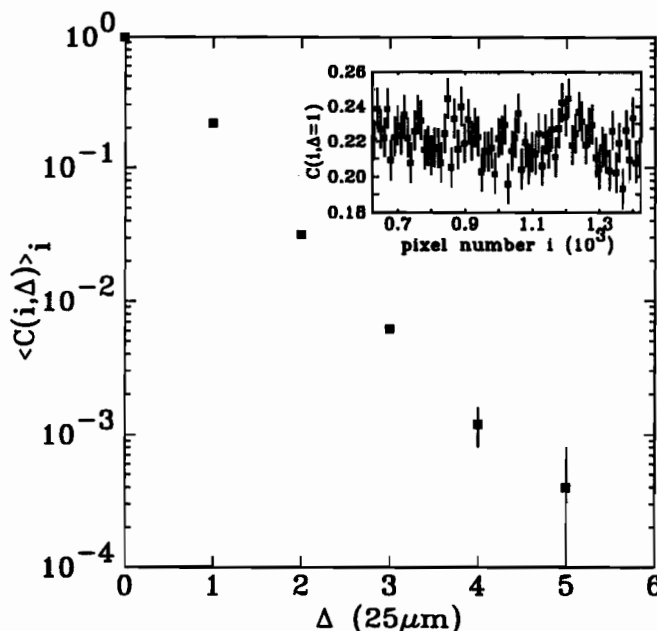


Figure 3.2: Spatial average of $C(i, \Delta)$, as defined in Eq. 3.11, versus Δ . Each point was calculated from an average over all pixels of $C(i, \Delta)$, shown in the inset for $\Delta = 1$.

To determine the uniformity of $k(\vec{r})$, 8000 patterns were measured and analyzed. Fig. 3.1b was obtained by scattering 8.05 keV X-rays, coming from of an X-ray tube with a Cu target and a Ge (111) monochromator set on Cu K_α . The beam covered approximately half of the array. The small tails on the average are due to diffuse scattering. Note the logarithmic axes for the mean and the variance; the signal varies over three orders of magnitude but the ratio is essentially independent of signal level. A dark variance of 1.1 ADU² causes the large fluctuations in $k(\vec{r})$ when the X-ray signal is comparable to the electronic noise signal. Measuring more dark patterns (larger N_d) would reduce the error on k . A least-square fit of the ratio to a constant between pixel 650 to 1400 gives $k=0.792$ and a χ^2 of 2, indicating the possibility of systematic variations in pixels with an rms amplitude of 2%. Note that a large number of identical exposures have to be analyzed to detect fluctuations this small. If signal variations between pixels of the order of a few percent are important, then these fluctuations have to be taken into account by using a different calibration constant for each pixel. Note that the number of electron-hole pairs created is proportional to the photon energy. This is reflected in the two different values of k , 0.682 and 0.792, at 6.93 and 8.05 keV respectively.

The inset of Fig. 3.2 shows the autocorrelation function of $V(\vec{r}, t)$ as calculated from Eq. (3.11) for nearest neighbor coupling ($\Delta = 1$). Here \vec{r} has been replaced by an integer index for the one dimensional detector. The spatial average of the correlation function, $\langle C(i, 1) \rangle_i = 0.2201 \pm 0.0004$. The spatial variance of the correlation function, $S_{i,C}^2 = (1.21 \pm 0.06) \times 10^{-4}$, agrees well with the expected variance (see [62] p 626) of $1/N$, where N is the number of scans averaged. Within error, $C(i, 1)$ is equal for all pixels. For larger Δ , we found $\langle C(i, 2) \rangle_i = 0.0319$, $\langle C(i, 3) \rangle_i = 0.0062$, $\langle C(i, 4) \rangle_i = 0.0012$ and $\langle C(i, 5) \rangle_i = 0.0004$, all measured within ± 0.0004 . The technique is very sensitive, since we can measure very small correlations between pixels separated by $100 \mu\text{m}$. Fig. 3.2 shows $\langle C(i, \Delta) \rangle_i$ versus Δ . The decay of the correlation function is approximately exponential, which is consistent with the diffusion of the electric charge to neighboring pixels [75].

As discussed in section 3.0.3, the resolution function $h(i')$ is evaluated from Eq. (3.13-3.15), based on the assumption that only $h(0)$, $h(-1)$ and $h(1)$ are non-zero, and that $h(-1) = h(1) = h_1$. Replacing the integrals by sums in Eq. (3.13-3.15), one finds that

$$k = \frac{S_{i,V}^2}{\langle V \rangle_i} = \frac{(h_0^2 + 2h_1^2)}{(h_0 + 2h_1)} = 0.792, \text{ and} \quad (3.17)$$

$$\langle C(i, \Delta = 1) \rangle_i = \frac{(2h_0h_1)}{(h_0^2 + 2h_1^2)} = 0.2201, \quad (3.18)$$

which gives $h_0 = 0.947$ and $h_1 = 0.107$. To transform the signal V to detected photons, one must divide V by $\int h(\vec{r}) d\vec{r} = h_0 + 2h_1 = 1.16$ instead of by k . The above model reproduces the essential features but does not give the next nearest neighbor correlation correctly. With this model, $\langle C(i, 2) \rangle_i = h_1^2 / (h_0^2 + 2h_1^2) = 0.012$, which is lower than the observed correlation. This can be fixed by extending the range of the response function to the third neighbor ¹.

The detective quantum efficiency was evaluated by measuring n_i with a scintillation

¹The simplest model fitting all data points requires four parameters. By including h_2 and h_3 in the model, we can solve simultaneously the equations for the ratio and for the five correlation functions using a non-linear least squares fit program. Eq. (3.17) becomes $k = \frac{S_{i,V}^2}{\langle V \rangle_i} = \frac{h_0^2 + 2h_1^2 + 2h_2^2 + 2h_3^2}{h_0 + 2h_1 + 2h_2 + 2h_3} = 0.792$, Eq. (3.18) is rewritten $\langle C(i, \Delta = 1) \rangle_i = \frac{2h_0h_1 + 2h_1h_2 + 2h_2h_3}{h_0^2 + 2h_1^2 + 2h_2^2 + 2h_3^2} = 0.2201$, and so on. One then finds $h_0 = 0.964$, $h_1 = 0.108$, $h_2 = 0.0095$ and $h_3 = 0.002$.

counter masked by a 1.3 mm hole, and then $\langle V \rangle_{\vec{r}}$ was measured by centering the height of the PSD behind this hole. Using Eq. (3.16), we find $\alpha = 37 \pm 2 \%$ for 8.05 keV X-rays. This can be compared to the expected detective quantum efficiency estimated for transmission through the 250 μm Be window of the detector, transmission through an additional 1 μm SiO₂ overcoat and the fraction of absorbed X-rays in the electron diffusion length of the Si, t_{Si} ,

$$\alpha = \exp(-\mu_{Be}\rho_{Be}t_{Be}) \exp(-\mu_{SiO_2}\rho_{SiO_2}t_{SiO_2}) [1 - \exp(-\mu_{Si}\rho_{Si}t_{Si})]. \quad (3.19)$$

Using the mass absorption coefficients¹ 1.1, 36.4, 64.7 cm²/g for Be, Si and SiO₂ respectively at 8.05 keV, and densities of 1.85, 2.32, 2.21 g/cm³, and a diffusion length $t_{Si} = 50\mu\text{m}$ as specified by the manufacturer², this estimate gives $\alpha = 50\%$, and agrees reasonably well with the measured value.

3.0.5 Characterization of a CCD array

The principle of photon detection of a CCD is similar to the linear array described in section 3.0.3. In a CCD, the detected charge is stored in MOS capacitors and read by a series of parallel row transfers and serial pixel-to-pixel transfers. For coherent X-ray experiments [15, 25], we used a virtual phase architecture TI 4849 chip, with 390 × 584 22.4 μm wide square pixels. The depletion depth of the chip is 12 μm , which gives a sufficient detective quantum efficiency for direct X-ray illumination. Further detail is given in Table 3.1 and elsewhere [76, 77, 78, 79]. To characterize the detector, measurements were made at the high brilliance wiggler beamline X25 at NSLS with a Si (111) monochromator set at 7.0 keV. Fig. 3.3 shows the experimental set up.

The ratio $k = S_{\vec{r},V}^2 / \langle V \rangle_{\vec{r}}$ is shown in Fig. 3.4 as a function of $\langle n_i \rangle_{\vec{r}}$. For a detector with a linear response, k is a constant, independent of n_i . We were quite surprised to see a non-linear relationship for k because the response to visible light

¹The constants were obtained from an online database called the Nuclear Data Center, at Brookhaven National Laboratory. To get data, telnet to bnlnd2.dne.bnl.gov, username `nndc`, and search the X-ray absorption database.

²See the technical information sheet on the RL2048S Solid State Line Scanner 2048 Elements, EG&G Reticon, 345 Potrero Avenue, Sunnyvale, California 94086-4197

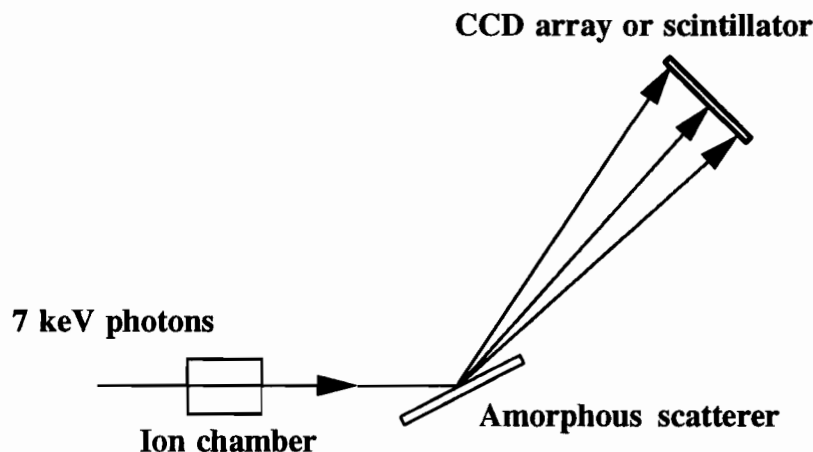


Figure 3.3: Experimental set up for the characterization of the CCD array. The X-ray beam was scattered with a piece of polystyrene to produce a spatially uniform exposure [71, 74]. The detector was centered at a scattering angle of $2\Theta = 23^\circ$ and placed 1.04 m from the center of rotation. n_i could be varied by detuning the monochromator, and therefore modifying the incident flux, or by varying the integration time τ from 1 to 240 s. An ion chamber was used to monitor the incident intensity on the sample, and a scintillation detector, masked with a 4 mm circular aperture, was placed at the CCD position and allowed us to determine n_i . This way, the scintillator signal was used to calibrate the ion chamber signal (I_{mon}). Using the ratio of areas and counts, the count rate per pixel was obtained, based on I_{mon} . The highest count rate was $1 \text{ photon}/(22.4 \mu\text{m})^2/\text{sec}$.

had been measured to be linear to within 0.5 % [76, 77, 78, 79]. It was later discovered that an inappropriate amplifier was responsible for the non-linearity. When recently tested with the correct operating electronics, the response to X-rays was linear. Since the model used in section 3.0.3 assumes linearity, it will be generalized below to include a non-linear response.

A treatment for non linear detectors

In many X-ray scattering experiments, one needs to determine n_i instead of n_d . This is done by calibrating the response of the PSD, V , for different n_i . Fig. 3.5 shows the mean of the CCD response over a region of 100×100 pixels, $\langle V \rangle_\tau$, versus n_i . The calibration was checked ten days later and remained mostly unchanged. The response of the detector depends only on n_i , since all the data points with an equal integrated flux $I_{\text{mon}}\tau$ fall on the same line in Fig. 3.5 although they differ widely in exposure times and incident flux. Several functions were tried to obtain an analytic relation

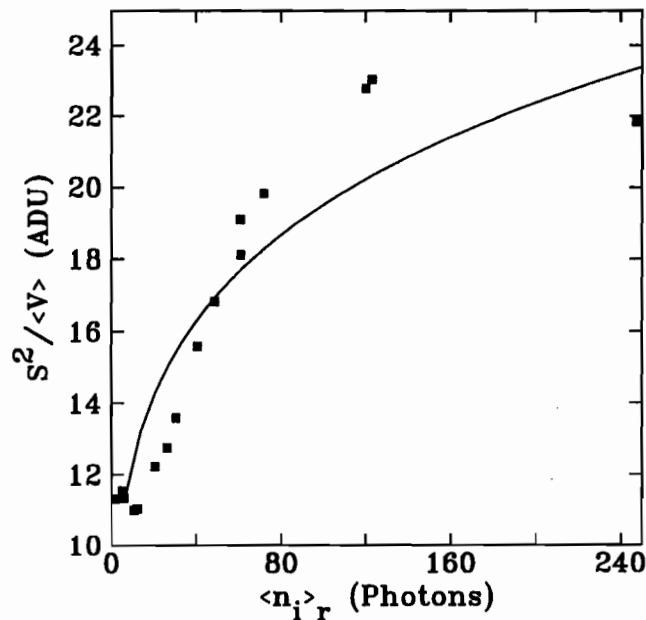


Figure 3.4: $k = S_{\vec{r},V}^2 / \langle V \rangle_{\vec{r}}$ versus the incident integrated intensity on the detector $\langle n_i \rangle_{\vec{r}}$. The average and variance were calculated over a region of 100 by 100 pixels. The solid line is a least squares fit.

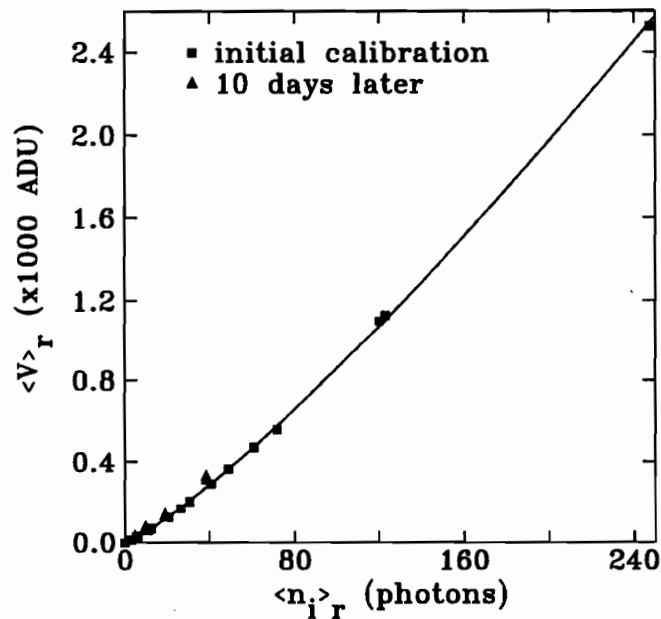


Figure 3.5: Spatial average of the signal $V(\vec{r}, t)$ over a region of 100 by 100 pixels versus the number of photons incident on the surface of a pixel $\langle n_i \rangle_{\vec{r}}$. Two data sets taken ten days apart (squares and triangles) are shown. The solid line is a least squares fit to the first calibration with $n_i = 0.35V^{0.84}$. This function is applied to the measured signal to linearize it. V was less than 75% of the saturation value for all points.

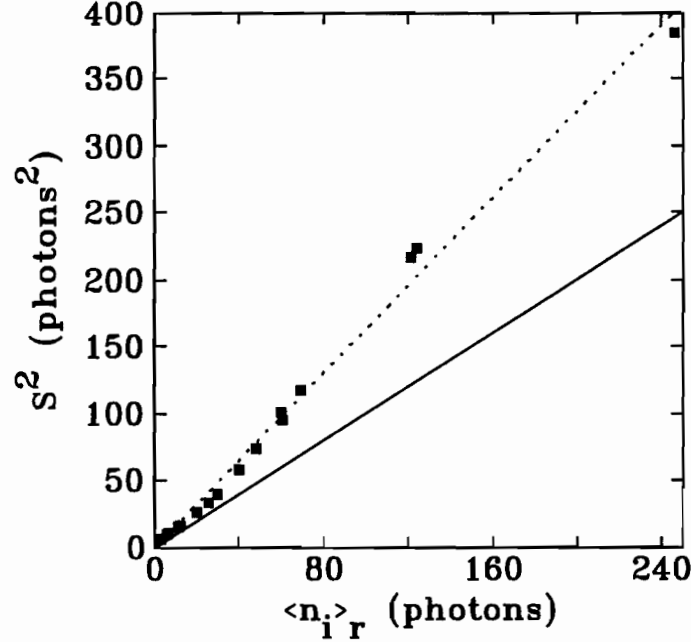


Figure 3.6: The spatial variance of the linearized data measured in a region of 100 by 100 pixels versus the linearized signal. One would expect the variance $S_{\vec{r},v^*}^2$ to go as $\langle n_i \rangle_{\vec{r}}$ in the case of a simple Poisson law (solid line). The dotted line is $1.63\langle n_i \rangle_{\vec{r}}$.

for the CCD response. The solid line in Fig. 3.5,

$$n_i = f^{-1}(V) = 0.35V^{0.84}, \quad (3.20)$$

is the best least squares fit found. This function allows one to linearize the measured signal V with sufficient accuracy.

The linearized signal, v^* , is defined by $v^* = f^{-1}(V)$. It has the same units as n_i , but its statistic is different from the Poisson statistic of n_i . In order to determine the noise in the linearized signal, we evaluated the spatial variance of v^* , $S_{\vec{r},v^*}^2$, in a region of 100×100 pixels versus n_i (see Fig. 3.6). The solid line is the relation expected for a Poisson distribution ($S_{\vec{r},v^*}^2 = \langle n_i \rangle_{\vec{r}}$), while the dotted line is $S_{\vec{r},v^*}^2 = 1.63\langle n_i \rangle_{\vec{r}}$. The variance is larger because the spatial resolution of the CCD is larger than the area of a pixel, and α is smaller than one.

Fig. 3.7 shows averages of a single exposure of $V(\vec{r}, t)$ taken over columns and rows of the detector. Pixels which are in the rows 110 to 480 and columns 10 to 380, which represent most of the detector area, are used for the averages. The mean is uniform in both directions with rms fluctuations of 2 %. Fig. 3.8 shows a bitmap of the

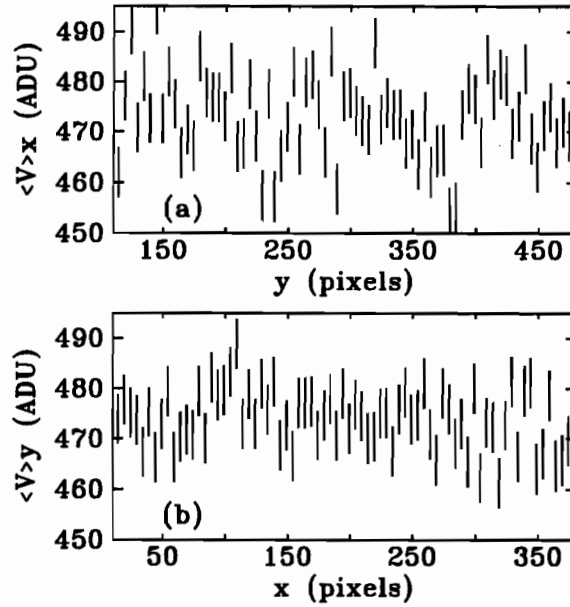


Figure 3.7: (a) Signals summed over 370 rows (top) and 370 columns.

variance $S_{t,V}^2$, calculated from 23 frames, each exposed for 1 s. The variance is uniform over the whole detector area, except for a few bad columns in the parallel transfer direction (y axis), where the variance is significantly lower. Pixels in columns 26-28, 72-73, 181-182, 208-209, have 40 to 80% less than average variance. This is shown in Fig. 3.9, where the average of $S_{t,V}^2$ over row 420 to 520 is displayed as a function of the horizontal position. A similar average of $\langle V \rangle_t$ is shown for comparison. The mean only fluctuates by a few percent. It is important to measure the noise of each pixel to fully characterize the detector.

The resolution function is extracted from the spatial correlation $C(\vec{\Delta})$, defined by

$$C(\vec{\Delta}) = \frac{\langle (v^*(\vec{r}, t)v^*(\vec{r} + \vec{\Delta}, t)) \rangle_{\vec{r}} - \langle (v^*(\vec{r}, t)) \rangle_{\vec{r}}^2}{S_{\vec{r},v^*}^2(t)}, \quad (3.21)$$

where the displacement $\vec{\Delta}$ is measured in units of pixels. This definition is similar to Eq. 3.11. Sufficiently good statistics can be achieved based on a single exposure of the CCD. A fast calculation algorithm may be used¹. Knowledge of $C(\vec{\Delta})$ is necessary for coherent X-ray experiments, where one is interested in the speckle size, which is of the order of the pixel dimensions [25]. Fig. 3.10 shows two slices of $C(\Delta x, \Delta y)$, where

¹We use a standard fast Fourier transform (fft) algorithm to calculate the spatial autocorrelation function, described in Ref. [62], Chapter 12. $C(\vec{\Delta}) = \text{fft}^{-1}(\text{fft}(v^*)\text{fft}^*(v^*))$, where $\text{fft}(v^*)$ is the complex fft of v^* .

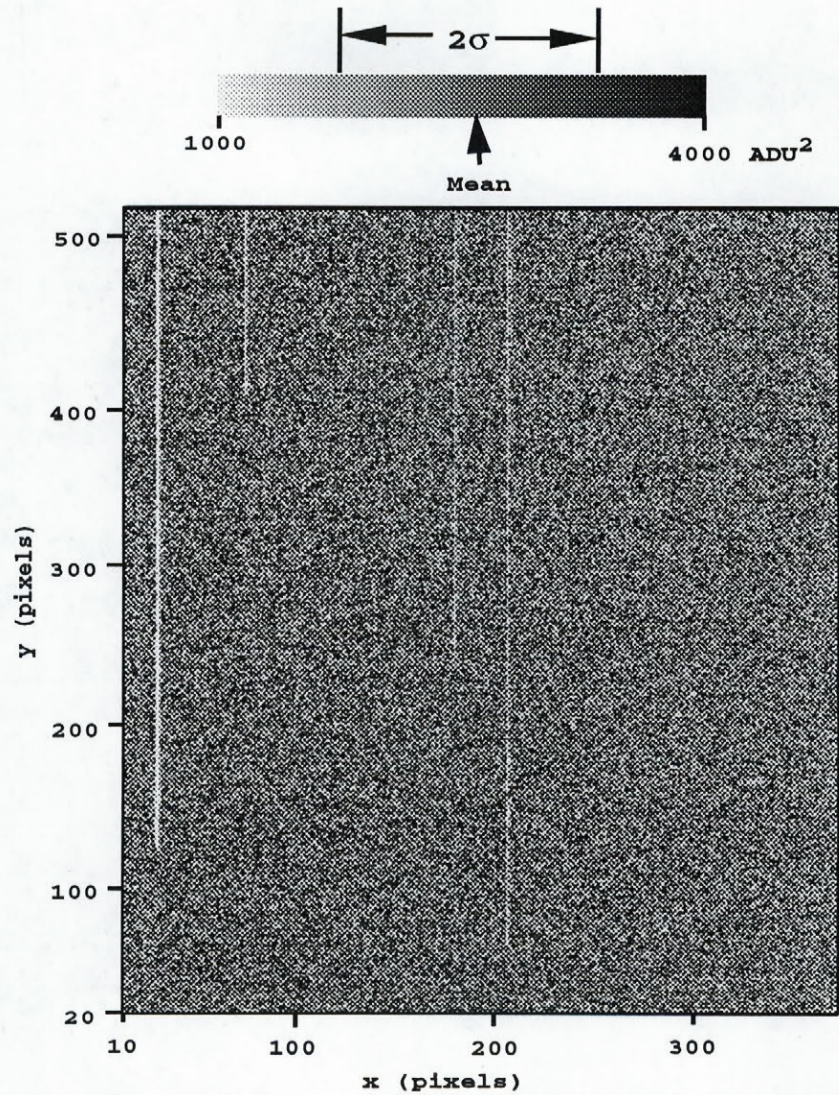


Figure 3.8: Time averaged variance $S_{t,V}^2(\vec{r})$ of the pixels in row 20 to 520 and column 10 to 380. 23 exposures of one seconds each were averaged. An inverted grey scale is used to display the data. On the top scale, the spatial average and the standard deviation of $S_{t,V}^2(\vec{r})$ are marked. Note that the variance is relatively uniform except for pixels in certain columns, where the variance is much lower.

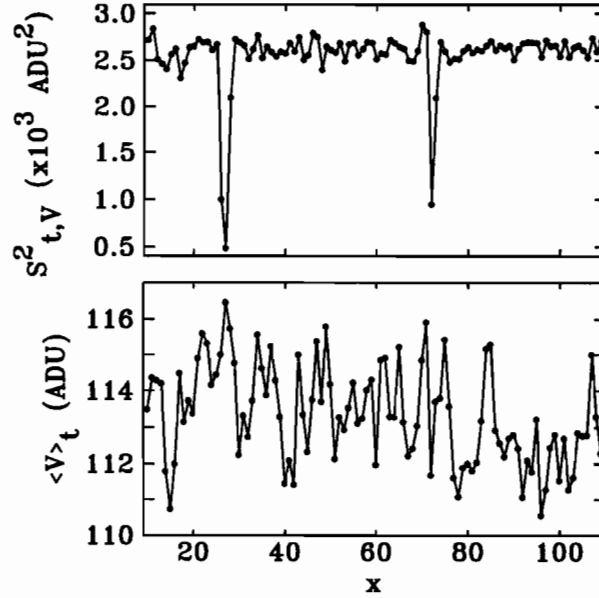


Figure 3.9: Average of $S^2_{t,v}(\vec{r})$, calculated over a column between row 420 and 520 of the CCD, shown versus the index of the column. The pixels in columns 26 to 28, 72 to 73, have much lower variance than other pixels. $\langle V \rangle_t$ is shown for comparison. The mean shows typical behavior for these columns. It is important to measure the variance of the signal of each pixel when one performs intensity fluctuation spectroscopy with a CCD.

the first index refers to the columns and the second to the rows of the CCD array. The correlation function $C(\Delta, 0)$ decays more slowly than $C(0, \Delta)$, i.e the resolution is worse along the serial transfer direction than along the parallel transfer direction.

The correlation coefficients are non-zero for the nearest and next nearest neighbors of $C(0, 0)$, with $C(1, 0) = 0.52 \pm 0.05$, $C(0, 1) = 0.12 \pm 0.01$ and $C(1, 1) = C(-1, 1) = 0.07 \pm 0.02$. Note that $C(\vec{\Delta}) = C(-\vec{\Delta})$, based on Eq. (3.21). Thus the resolution function has a range of one to two pixels. Using the simplest model, we choose $h(\vec{r})$ to be non zero only for the nearest neighbors, i.e. $h(0, 0) = h_{00}$, $h(1, 0) = h(-1, 0) = h_{10}$ and $h(0, 1) = h(0, -1) = h_{01}$. We choose to normalize the integral of $h(\vec{r})$ to unity, assuming that one photon will be distributed amongst several pixels so that

$$h_{00} + 2h_{10} + 2h_{01} = 1. \quad (3.22)$$

From Eq. (3.15), the correlation function of this disturbance gives

$$C(1, 0) = \frac{2h_{00}h_{10}}{h_{00}^2 + 2h_{10}^2 + 2h_{01}^2} = 0.52, \text{ and} \quad (3.23)$$

$$C(0, 1) = \frac{2h_{00}h_{01}}{h_{00}^2 + 2h_{10}^2 + 2h_{01}^2} = 0.12. \quad (3.24)$$

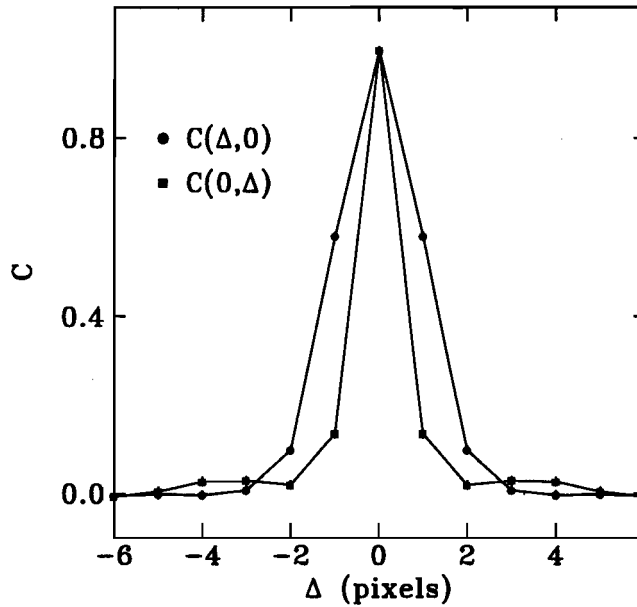


Figure 3.10: Two perpendicular slices of the space autocorrelation function, defined by Eq. (3.21), for uniform scattering data. $C(\Delta, 0)$ for the serial transfer direction (circles) and $C(0, \Delta)$ for the parallel transfer direction (squares) are shown versus Δ . The error bars are slightly larger than the size of the squares. The correlation decays to 0 in about two pixels along x , the serial transfer direction, and in one pixel perpendicular to it.

Solving Eq. (3.22-3.24), we find $h_{00} = 0.563, h_{01} = 0.042, h_{10} = 0.177$. A larger fraction of the signal leaks to the nearest neighbors along the serial transfer direction.

The resolution function alters the variance of the number of detected photons. From Eq. (3.13,3.14), one finds

$$K_s \equiv \frac{S_{\vec{r}, n_d}^2}{\langle n_d \rangle_{\vec{r}}} = h_{00}^2 + 2h_{10}^2 + 2h_{01}^2 = 0.38. \quad (3.25)$$

Without leakage, $K_s = 1$, so that the variance is smaller than what one expects from Poisson noise by a factor K_s . Using $\langle n_d(\vec{r}) \rangle_{\vec{r}} = \alpha \langle v^*(\vec{r}) \rangle_{\vec{r}}$, assuming that α is the same for each pixels, one gets

$$S_{\vec{r}, n_d}^2 = \alpha^2 S_{\vec{r}, v^*}^2 = K_s \alpha \langle v^* \rangle_{\vec{r}}. \quad (3.26)$$

From a Taylor expansion of the linearization function, $v^* = f^{-1}(V)$, one obtains

$$S_{\vec{r}, v^*}^2 = S_{\vec{r}, V}^2 (dv^*/dV)^2, \quad (3.27)$$

where $S_{\vec{r}, v^*}^2$ is the variance of the linearized data. Recalling that for the linearization function, $dv^*/dV = B \langle v^* \rangle_{\vec{r}} / \langle V \rangle_{\vec{r}}$ and substituting Eq. (3.27) into Eq. (3.26), one

gets

$$\frac{S_{r,V}^2}{\langle V \rangle_r} = \frac{K_s \langle v^* \rangle_r}{\alpha \langle V \rangle_r (dv^*/dV)^2} = \frac{K_s \langle V \rangle_r}{\alpha \langle v^* \rangle_r B^2}, \quad (3.28)$$

where B is the exponent of the power law fit in Fig. 3.5 equal to 0.84. This equation includes three different contributions in the ratio: the smearing from the finite resolution, the non-linear behavior and the detective quantum efficiency. For a linear detector ($B = 1$), with a resolution of one pixel area ($K_s = 1$), Eq. (3.28) becomes equivalent to Eq. (3.6). Therefore $\frac{S_{r,V}^2}{\langle V \rangle_r}$ is not constant (see Fig. 3.4), since $\frac{\langle V \rangle_r}{\langle n_i \rangle_r}$ is non-linear. Fitting the measured CCD response in Fig. 3.4 to Eq. (3.28) gives a detective quantum efficiency $\alpha = 0.22$. Eq. (3.19), with the values $\mu_{Si} = 94.9 \text{ cm}^2/\text{g}$, $\mu_{Be} = 1.6 \text{ cm}^2/\text{g}$, $t_{SiO_2} = 0 \text{ }\mu\text{m}$ and $t_{Si} = 12 \text{ }\mu\text{m}$, gives $\alpha = 0.22$, which agrees well with the measurement. Furthermore, Eq. (3.26) gives $K_s/\alpha = 1.5$, which corresponds to the ratio of $S_{r,v^*}^2/\langle v^* \rangle_r$ in Fig. 3.6.

3.0.6 Discussion

One must carefully characterize the response of a current state-of-the-art PSD to obtain quantitative information. For example, in the intensity fluctuation spectroscopy experiments reported in this thesis, it is essential to distinguish the noise of the detector from measured scattered intensity fluctuations, and we must know the spatial correlations of the detector's resolution function quite accurately. We have shown that we can characterize a PSD by measuring means, variances, and spatial auto-correlation functions and comparing these measurements to the statistical estimators expected for a Poisson distribution. The technique can measure the resolution function, and gives an estimate of the detective quantum efficiency. It is easy to implement and can be very sensitive when enough scans are averaged. The mean and variance arrays are easily calculable in real time by storing only three arrays in memory¹.

The technique can also handle detector non-linearities. Before this study, previous

¹Only three arrays are required. Storing the first pattern as an offset array $V(t_0)$, we store in two arrays the difference $A_1 = \sum_{i=0}^{i=N} (V(t_i) - V(t_0))$ and the square of the difference $A_2 = \sum_{i=0}^{i=N} (V(t_i) - V(t_0))^2$. Then, the mean $\langle V \rangle_t = A_1/N + V(t_0)$ and the variance $S_{t,V}^2 = (A_2 - A_1^2/N)/(N-1)$. This algorithm minimizes the roundoff error (see Ref. [62] p 613), and minimizes the disk space required for the calibration. Similar sums can be taken for calculating the correlation function in Eq. 3.11.

work in our group assumed that linear PSD have a resolution of one pixel. In future high resolution experiments, the finite resolution of the detector should be taken into account.

A simple extension of the technique would be to measure the decay of the time correlation function of the CCD signal, when the detector is optically coupled to an X-ray fluorescent material. The advantage of using the correlation function here is that no special hardware, such as a fast shutter, is required for the experiment.

EXPERIMENTAL METHOD

4.1 *Beamline characterization and optics*

The experiments reported in this thesis were performed at the National Synchrotron Light Source (NSLS) at Brookhaven National Laboratory and at the Cornell High Energy Synchrotron Source (CHESS) during a test of the Advanced Photon Source (APS) undulator. Fig 2.4 shows a typical experimental setup.

The X25 beamline has been described in detail elsewhere [80, 81]. In short, the X-rays are generated by a 27 pole hybrid wiggler with a peak field of 1 T, installed on a straight section of the 2.5 GeV NSLS storage ring. This wiggler source is characterized by a deflection parameter $K = 12.3$, a characteristic opening angle $K/\gamma = 2.5$ mrad, and a critical energy of 4.6 keV. With a ring current of 230 mA, this source generates a total power of 1.8 kW. For our experiment, the gap was set at 24 mm.

The characteristic distances at X25 are shown in Table 2.1. To control the coherence lengths, two sets of upstream slits at 10.5 m from the source could be closed to reduce the effective source size. A double Si(111) monochromator was used to select 6.9 keV X-rays. The monochromator was slightly detuned from the Bragg condition to filter the third harmonic out. Two types of incident intensity monitors were used: an air filled ion chamber and a film of polyimide oriented at 45° from the incident beam, which scatters X-rays into a scintillation counter. Since the absorption length of 6.9 KeV X-rays in air is of the order of 0.5 m, vacuum flight paths were used to reduce X-ray absorption.

To ensure that the beam incident on the sample remained approximately defined

by the pinhole diameter, we placed the sample in the near field diffraction region of the pinhole [82] such that the pinhole to center of rotation distance

$$R_c < D^2/\lambda, \quad (4.1)$$

where D is the pinhole diameter. For the smallest pinhole used, $D = 3.5 \mu\text{m}$ and $\lambda = 1.797 \text{ \AA}$, which gives the condition $R_c < 6.8 \text{ cm}$. The input pinholes were placed at $R_c = 6.75 \text{ cm}$, which is well within the near field of the pinhole diffraction pattern for the measurements done with the 7.5, 15, 33 μm pinholes, but is on the edge of this region for the 3.5 μm pinhole. This is the closest distance achievable for our X-ray oven.

To determine and control the transverse coherence lengths, one must know the source size accurately. At X-25 the source size was measured by scanning the upstream x-y slits (see Fig. 2.4) to cut the beam totally while recording the intensity at the sample position behind a 3.5 μm pinhole. The beam profile is obtained by taking a derivative of the signal. The beam profile is then least-squared fitted using a Gaussian at the slit position, 10.5 m from the source. The horizontal and vertical fitted widths¹ are respectively $\sigma_x = 0.386 \text{ mm}$, $\sigma_y = 0.0179 \text{ mm}$ at 6.9 keV. Since the point of observation is 27.8 m from the source, the source size near the wiggler is $\sigma_x = 0.62$ and $\sigma_y = 0.0288 \text{ mm}$.

The CHESS synchrotron ring was operated at 5.437 GeV, with a maximum current of 100 mA [83]. The undulator was a prototype of the APS undulators. This undulator is made of 123 magnetic poles with 3.3 cm periods, and its fundamental energy can be tuned from 4.3 to 7.9 keV [83]. The undulator gap was set at 2.3 cm in order to tune to the 7 keV fundamental. The double Si (111) monochromator was set to diffract 7.0 keV X-rays. Since the source horizontal size $d_{sx} = 2.55 \text{ mm}$ is approximately twice larger at CHESS compared with X25, a 0.4 mm horizontal slit was placed 17.8 m from the source to limit the horizontal source size.

¹The Gaussian fit used was $I(x) = I_0 \exp(-.5(x - x_0)^2/\sigma_x^2)$, where x_0 is the peak center, σ_x the width, and I_0 the peak intensity.

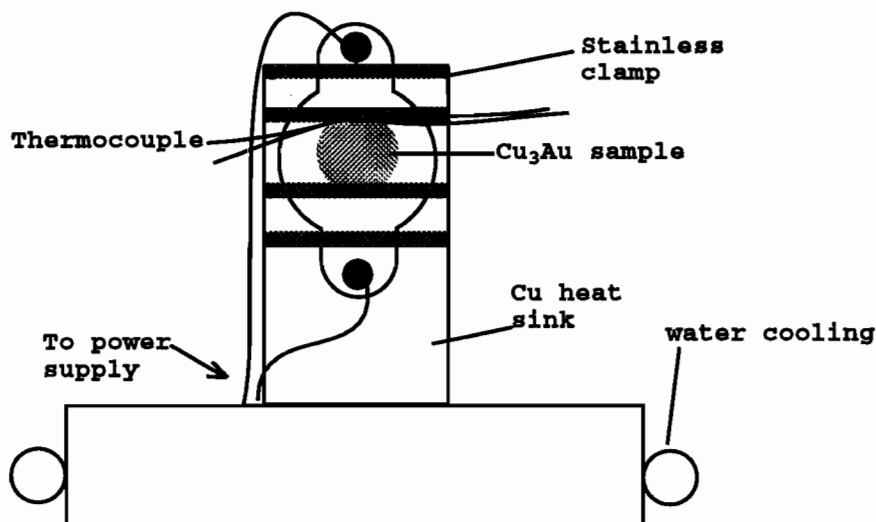


Figure 4.1: The X-ray oven.

4.2 Sample preparation and sample furnace

The sample preparation at the Oak Ridge National Laboratories has been previously described in detail [31, 32]. The sample surface normal is oriented along the [100]. A vacuum sample chamber was designed to heat the sample to elevated temperatures and to prevent its oxidation. The sample furnace essential element is a 6Ω pyrolytic Boron Nitride coated pyrolytic graphite heater¹ mounted on a water cooled Cu heat sink which gives sufficient cooling power to quench the sample rapidly. The sample was mounted on the heater using stainless steel clamps screwed on the Cu block. With this design, quench rates of a few Kelvin per second could be easily attained. The maximum temperature reached by this oven could be adjusted by thermally insulating the back of the heater and the Cu heat sink with varying thicknesses of mica. The mica limits the heat flow to the heat sink and increases the temperature difference between the heater and Cu block. A commercial proportional temperature controller (Omega CN8031) was used to maintain the set point temperature constant to within 0.1°C using a standard proportional, integral and differential control loop. Two type-K thermocouples recorded the sample temperature and the control temperature. A

¹The heater is a 2 cm diameter BoralectricTM PBN/PG resistance heating element, purchased from Union Carbide Coatings Service Corporation, P.O. Box 94924, Cleveland, OH, USA, 44101-4924.

standard cold junction compensator (Omega-CJ-K) was used to set the ice point reference of the sample thermocouple. The thermocouples were held in contact with the sample by the clamps. The X-rays could penetrate the sample chamber through a 180 degree Be window, 0.015 inch thick¹. A DC power supply, controlled by the temperature controller through an operational amplifier input, generated a current from zero to six A which is required because of the small heater resistance.

4.3 Scattering geometry

Fig. 4.2 shows the scattering geometry for this experiment. The CCD or the scintillator is mounted on a standard 4 circle Huber diffractometer, computer controlled to scan the three sample angles θ , ϕ , and χ , and the central detector angle 2θ , which defines, with the incoming beam direction, the scattering plane. The scattering plane is vertical. The sample is mounted on the ϕ circle of the diffractometer, and the four angles are set for the (100) reflection.

Because the CCD is able to measure outgoing wavevectors in two directions, we use the central pixel to define a scattering plane. Thus, $2\theta_{\perp}$ is the angle perpendicular to the plane, and $2\theta_{\parallel}$ is in the plane. Here $2\theta_{\parallel}$ is like the usual detector angle. In Fig. 4.2, θ_i is the angle of incidence of the X-ray beam with respect to the surface. Following Ref [16], one can show that the components of the scattering wavevector $\vec{q} = \vec{k}_f - \vec{k}_i$ in the sample coordinates are

$$\begin{aligned} q_x &= k \sin 2\theta_{\perp} \approx kx'/R_d, \\ q_y &= k(\cos 2\theta_{\perp} \cos(2\theta_{\parallel} - \theta_i) - \cos \theta_i) \approx k(\cos(2\theta_B + y'/R_d - \theta_i) - \cos \theta_i), \\ q_z &= k(\cos 2\theta_{\perp} \sin(2\theta_{\parallel} - \theta_i) + \sin \theta_i) \approx k(\sin(2\theta_B + y'/R_d - \theta_i) + \sin \theta_i), \end{aligned} \quad (4.2)$$

where $k = 2\pi/\lambda$. The sample x-axis is oriented along the theta axis of rotation, while the z-axis is oriented along the surface normal. The x' and y' axes are the pixel coordinates in the detector plane, centered on the Bragg angle $2\theta_B$.

¹This Be thickness absorbs 11 % of the 7 KeV X-rays.

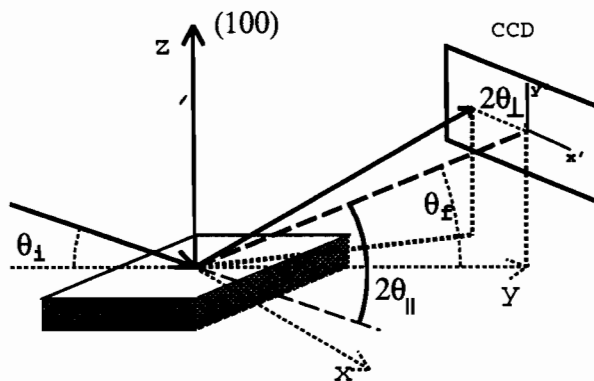


Figure 4.2: The scattering geometry. The Cu_3Au (100) is along the z -axis. The angle of incidence θ_i and the scattered angle θ_f are measured with respect to the sample surface. The angle $2\theta_{\parallel}$ is the usual detector angle.

4.4 Data treatment

The scattered X-rays were measured with the CCD described in Chapter 3. The data acquisition was stopped regularly to record a dark pattern without X-rays. This dark pattern slowly drifted in time over several hours and was monitored regularly. For the data acquired at X-25, this drift was correlated with an NSLS lab cooling water temperature drift¹, which affected the CCD chip temperature because this water cooled the CCD Peltier stage². This drift was of the order of one or two X-ray photons, but could easily be corrected by subtracting the most recent dark pattern. Furthermore, the four corners of the CCD were masked by lead to absorb all incident X-rays, so these areas were used to keep track of the drift in the dark pattern.

At X25, the detector signal was calibrated against a scintillation detector with a quantum efficiency of nearly 100%, in order to correct the detector non-linearity. After a dark signal subtraction, the detected signal was rescaled with this calibration using Eq. 3.20.

During the CHESS experiment, one of the CCD amplifiers was different than during the X25 experiment. For a given incident count rate and exposure time, if one assumes that the raw data measured at CHESS only differs from the X25 calibration

¹For example, it has been shown that the temperature drift in the cooling water at NSLS affects the bending magnet alignment causing orbit motion[84].

²This problem has since been fixed by cooling the Peltier stage with a recirculating temperature-controlled water bath.

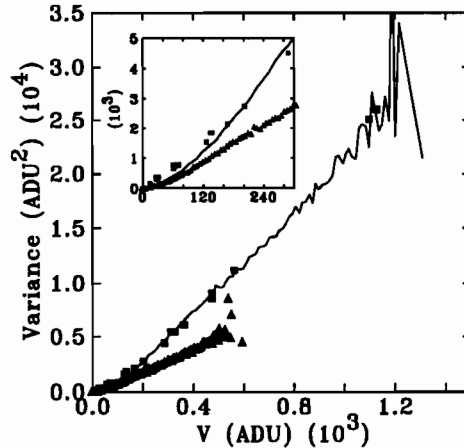


Figure 4.3: The measured CCD signal variance versus the mean. The calibration at X25 and CHES are respectively shown with squares and triangles. The solid line represents the CHES data rescaled by a factor 2.2 for the mean and $(2.2)^2$ for the variance.

by a multiplicative constant, one can use Eq. 3.20 to rescale the CHES data into photons. It is shown in Fig. 4.3 that this constant is $a = 2.2$ so that the signal at X25, V_X , is equal to aV_C , where V_C is the signal at CHES, and the variance at X25, S_X^2 is equal to $a^2S_C^2$. This rescaling is excellent for count rates above 160 ADU. As shown in the inset, some difference is seen for small count rates.

To compensate for the slow decay of the incident synchrotron radiation intensity, the signal was scaled to the incident beam intensity measured by an air filled ion chamber beam monitor¹. After linearization and normalization to the incident intensity, the floating point signal was multiplied by a factor 100 and then saved into a two byte short integer array for further analysis.

4.5 Pinhole construction

The pinholes were made by laser drilling through 50 μm thick Pt foils². The pinholes used are really *pinhole tunnels* because their diameters are smaller than their 50 μm thickness. The foils were glued on a 1.0 mm thick Ta mount, pierced with a hole of diameter $D_m = 0.5$ mm. The ratio of transmitted intensity through a pinhole of diam-

¹This detector measures the ionized current between two high voltage electrodes due to the photoionization of gas molecules. This signal is proportional to the incident intensity when there is no dielectric breakdown of the gas.

²The pinholes were manufactured by Optimization Hole division, 123 Nashua Rd, suite 172, Londonderry, NH 03053, USA, (603)623-2800

eter D over the transmitted intensity through the Pt foil is $D^2/[D_m^2 \exp(-\mu_{Pt}\rho_{Pt}t)]$, where the density of Pt $\rho_{Pt} = 21.41 \text{ g/cm}^3$, the Pt thickness $t = 50 \text{ }\mu\text{m}$, and the mass absorption coefficient of Pt $\mu_{Pt} = 292 \text{ cm}^2/\text{g}$ at 7.0 keV. This design was found to work well at 7 keV, since for the smallest pinhole used, $D = 3.5 \text{ }\mu\text{m}$, this ratio is 1.8×10^9 . With approximately 3×10^5 photons/s passing through the pinhole, 1.7×10^{-4} photons/s would be transmitted through the foil! It was found later that this design can be further improved by re-orienting the pinhole with respect to the axis of symmetry¹. Finally one should note that one can use slits to limit the sample size instead of pinholes².

4.6 *Demonstration of coherence: Fraunhofer diffraction pattern of a pinhole.*

To demonstrate that a hard X-ray beam generated by a second generation synchrotron source is transversally coherent, one would perform a Young's double-slit experiment. Since the transverse coherence length of synchrotron sources at the sample position is only a few μm , we would have to make two pinholes, separated by a few μm , each having a one μm diameter. Since this is difficult to achieve experimentally³, it is easier to observe the Fraunhofer diffraction pattern of a single pinhole. If the transverse coherence lengths l_x or l_y are too small compared to the pinhole diameter D , then no diffraction pattern would be observed. Otherwise, the Fraunhofer condition

¹Recently, we found that the axis of maximum transmission through the pinholes was not exactly adjusted with the surface normal of the foils. The pinholes were mounted on a goniometer and centered by rocking the angle of incidence of the incoming radiation. We found that the axis of maximum transmission for the 3.5 μm and 7.5 μm pinholes was tilted by 4.3 and 3° respectively with respect to the axis perpendicular to the mount. An increase in flux of a factor 5 was found for the 3.5 μm pinhole. The pinholes were remounted to fix this problem.

²Dr Doug Abernathy has done some recent work on this at ESRF using sharpened Huber slits to observe Fraunhofer diffraction patterns. It seems possible to control these slits accurately and reproducibly.

³The first observation of Fraunhofer diffraction patterns with hard X-rays from a rectangular 25 μm wide slit was made by Mancini and Bilderback[85]. Recently, Ferrer et al. [86] observed a Fraunhofer diffraction pattern of an *effective* slit made by an X-ray mirror. In a more recent experiment at ESRF, Comin et al. also observed Young's double-slit interference fringes at the surface diffraction beamline (bl13) of ESRF, using 4.73 KeV X-rays incident on two 0.5cm grazing incidence mirrors separated by 1 cm, which acted like double slits.

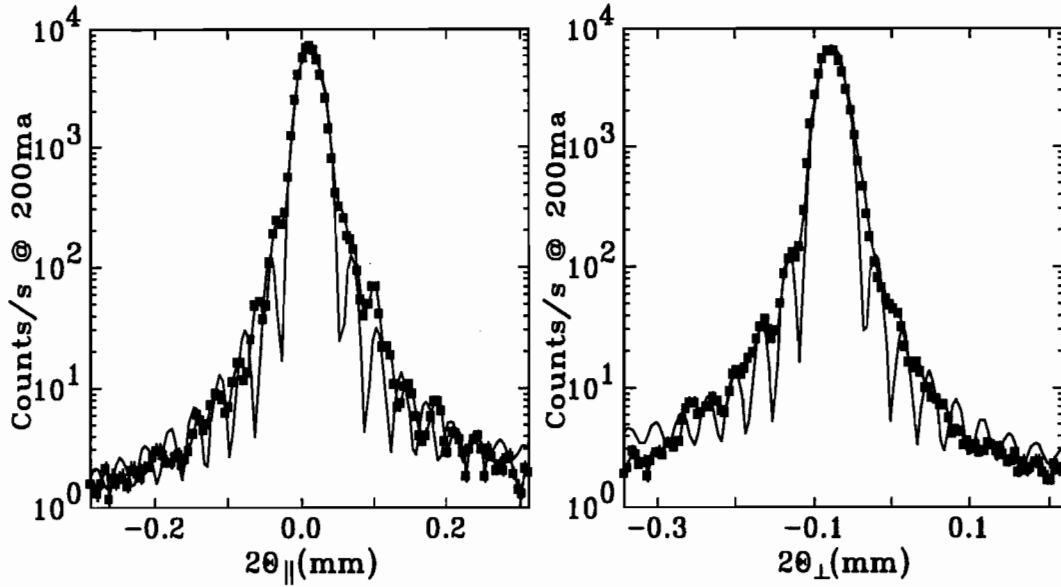


Figure 4.4: Fraunhofer diffraction patterns of a $7.5 \mu\text{m}$ pinhole resolved with a $8.5 \mu\text{m}$ pinhole, placed 1.12 m behind the first pinhole. The experiment is performed with 7 keV X-rays, at a ring current of 200 mA . The pinhole was scanned vertically or along $2\theta_{\parallel}$ (Left). A least-squares fit of the Fraunhofer diffraction pattern of a pinhole to Eq. 4.3, with $D = 5.9 \mu\text{m}$ is shown with a solid line. (Right) A detector scan in the horizontal, i.e. along $2\theta_{\perp}$. The fringe contrast is worst along $2\theta_{\perp}$, and the FWHM of the peak is wider than the least-squares fit with $D = 5.9 \mu\text{m}$. As expected, the fringe contrast is better along $2\theta_{\parallel}$ than along $2\theta_{\perp}$, because the vertical transverse coherence length is 22 times larger than the horizontal one.

is satisfied and fringes would be observable.

Fig 4.4 shows Fraunhofer diffraction patterns observed at NSLS X-25. This was observed with 1.77 \AA X-rays incident on a pinhole with $D = 7.5 \mu\text{m}$, placed 28 m from the source. The X-rays were detected with a scintillator masked by a $8.5 \mu\text{m}$ pinhole placed 1.12 m from the pinhole. Two scans along $2\theta_{\parallel}$ and $2\theta_{\perp}$ are shown. The contrast is excellent, revealing fringes observable over four orders of magnitude.

Recall that the detected intensity of a Fraunhofer diffraction pattern of a circular pinhole, measured by a point detector, is [39]

$$I(r) = \frac{I_0 A^2}{\lambda^2 R_d^2} \frac{4J_1^2\left(\frac{\pi D r}{\lambda R_d}\right)}{\left(\frac{\pi D r}{R_d \lambda}\right)^2}, \quad (4.3)$$

where x and y are respectively the horizontal and vertical displacements from the peak center in the detector plane, R_d is the distance between the detector and the pinhole with $r = \sqrt{x^2 + y^2} \ll R_d$, I_0 is the incident intensity on the pinhole and A is the pinhole area. The factor $A^2/(\lambda R_d)^2$ normalizes the integrated intensity to $\int_0^\infty 2\pi r I(r) dr = I_0 A$. This relation assumes a *plane wave illumination* of the pinhole

generated by a point source placed far away from the first pinhole. The first zero of this function occurs at $r = 1.22\lambda R_d/D$. Its FWHM is

$$FWHM = \frac{1.0288\lambda R_d}{D}. \quad (4.4)$$

The measured FWHM in Fig 4.4 are respectively 0.0298 mm and 0.0374 mm. Using Eq. 4.4 with $R_d = 1.121\text{m}$, one finds $D = 6.9$ and $5.5 \mu\text{m}$, which is in good agreement with the $7.5 \mu\text{m}$ diameter estimated by transmission. A plot of the theoretical Fraunhofer diffraction pattern of a circular pinhole convolved with the detector resolution is shown in both figures. The fit integrates Eq. 4.3 numerically over the detector pinhole area. Six parameters are used: a peak intensity, an input pinhole diameter, a center position, a fixed detector pinhole diameter of $8.5 \mu\text{m}$, a constant background, and a linear slope in the background. For the slice along $2\theta_{\parallel}$, the central fifteen data points are well fit, but the calculated fringes are out of phase with the data. For the slice along $2\theta_{\perp}$, the data are broader than the fit, and the fringe contrast is worse than the fringe contrast along $2\theta_{\parallel}$. The phase shift in the fringes and the asymmetric FWHM could be caused by averaging many horizontal coherence lengths in the pinhole diameter, and by spatial fluctuations on the incident intensity profile (see Fig. 4.7). When this occurs, more complicated forms of the theoretical diffraction must be used, like in section 5.7 of Ref. [39] and in Ref. [87].

We also observed these Fraunhofer diffraction patterns with the CCD detector. Using the parallel detection properties of the CCD and its time resolution, one can get more instantaneous properties of the diffracted beam and can test easily for source stability and motion. If the source moves or some upstream optical element moves, it is easy to track with the detector. This is a big advantage of the CCD over the scanning pinhole assembly used in the previous figure. Fig 4.5 shows the time average of the CCD data using an input pinhole diameter $D = 3.5 \mu\text{m}$ and a distance pinhole-CCD, $R_d = 1.04 \text{ m}$ using 6.9 keV X-rays. The CCD was exposed for two seconds, and thirty six files were averaged. As seen in the two perpendicular slices in the figure, the central 7×7 pixels are reasonably fit by the Fraunhofer diffraction

pattern of a circular pinhole, convolved with the detector's resolution¹ derived in Eq. (3.12). The error bars of the data were calculated using the estimated variance and Eq. (A.14). The fit shown is a non-linear least-squares fit, with a $\chi^2 = 14.4$, $D = 2.57 \mu\text{m}$ and a dark count of 0.25 photons/2sec/pixel. This high value of χ^2 is probably caused by several effects, like a non-circular pinhole², a finite source size which does not satisfy perfectly the Fraunhofer condition of a point source and an approximate resolution function. This fit has a smaller χ^2 than the fits in Fig 4.4, which were an order of magnitude larger. Since the ratio D/l_x is smaller for the $3.5 \mu\text{m}$ pinhole, the Fraunhofer diffraction condition is more closely matched with a smaller pinhole. Finally, each scan of the CCD was fit to the model. Fifty one patterns were collected with a cycling time of 10.4 s. The fit centers were constant to a fraction of a pixel size except in one of the scans where the peak center moved by two pixels ($45 \mu\text{rad}$) in the vertical. This sudden motion was seen in only one of the fifty one scans and seems to be characteristic of the stability at X-25³. This angular motion would correspond to a source motion of $2 \times 22.4 \mu\text{rad} \times 27.8 \text{ m} = 1.2 \text{ mm}$ which is too large for a vertical source motion. It is most likely caused by some motion of the monochromator, which results in an angular shift.

4.7 Incident X-ray beam structure and stability

Fig. 4.6 shows the time fluctuations of the incident beam at X-25 measured by an ion chamber monitor placed before a $3.5 \mu\text{m}$ pinhole. The time fluctuations of the total transmitted count rate measured with a scintillation detector placed behind the pinhole are also shown. The relative fluctuations of the detector and monitor signals are respectively 3.5 and 2 %. The detector signal fluctuations are larger than the monitor signal. Furthermore, the fluctuations in the ion chamber monitor signal

¹The calculated signal is integrated over the area of a pixel. Then it is smeared according to Eq. 3.12.

²One can see that the data are not quite circularly symmetric. Furthermore, two stripes are observed in the tails of the diffraction pattern. These stripes are not clearly seen in the previous figure, but they are easily seen far away from the peak.

³Prof. Steve Dierker mentioned that their group also observed a similar phenomena at X-25 in their small angle scattering data from gold colloids.

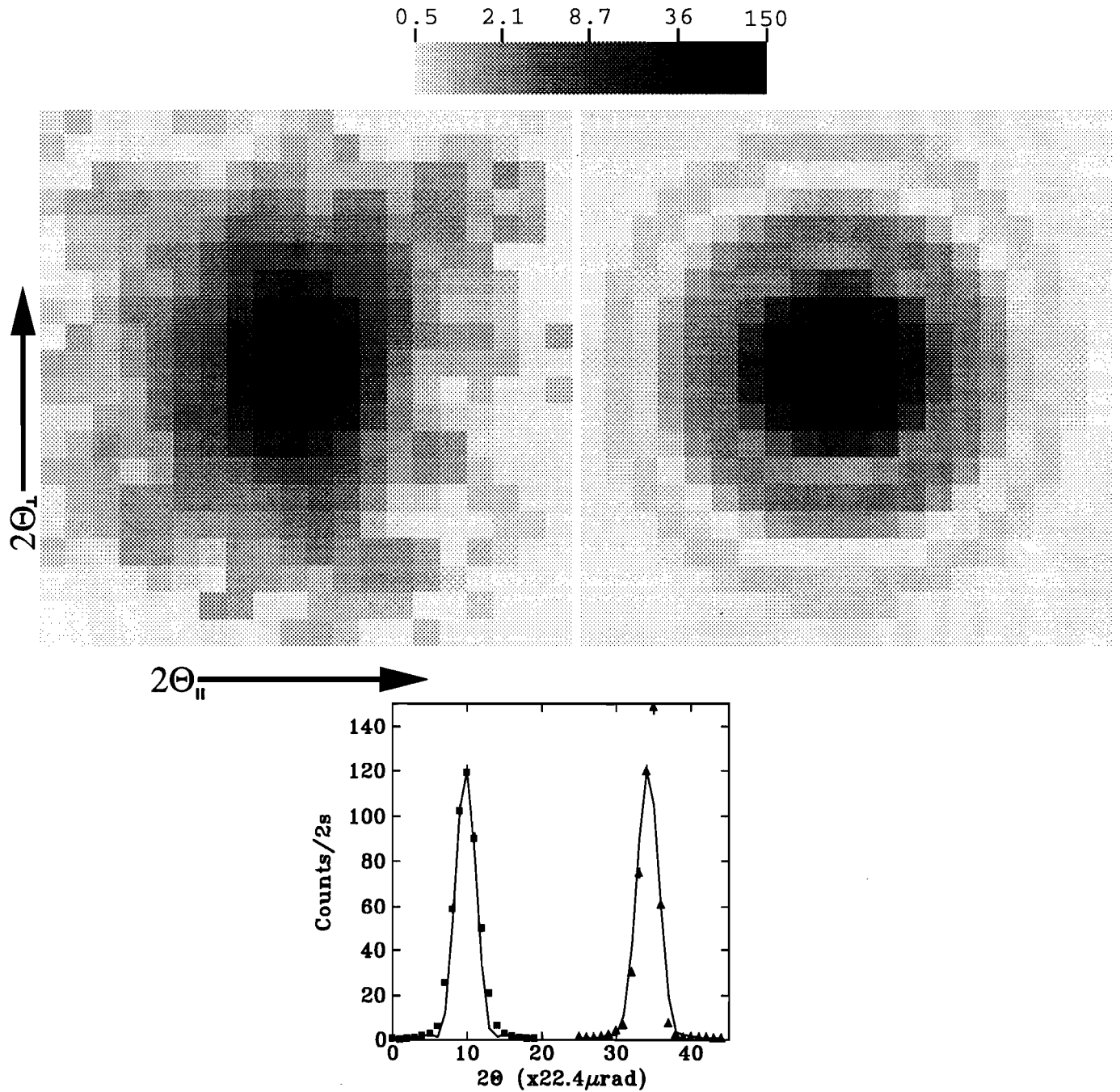


Figure 4.5: A grey scale of the CCD data (top left) for the central 20×20 pixel of the CCD. The grey scale is logarithmic as shown in the legend in photons/2sec/pixel. Each pixel subtends $22.4 \mu\text{rad}$. To the right, a least-square fit to a Fraunhofer diffraction pattern of a circular pinhole convolved with the detector resolution discussed in the text. Below, two perpendicular slices of the data (with squares) and fit (solid line).

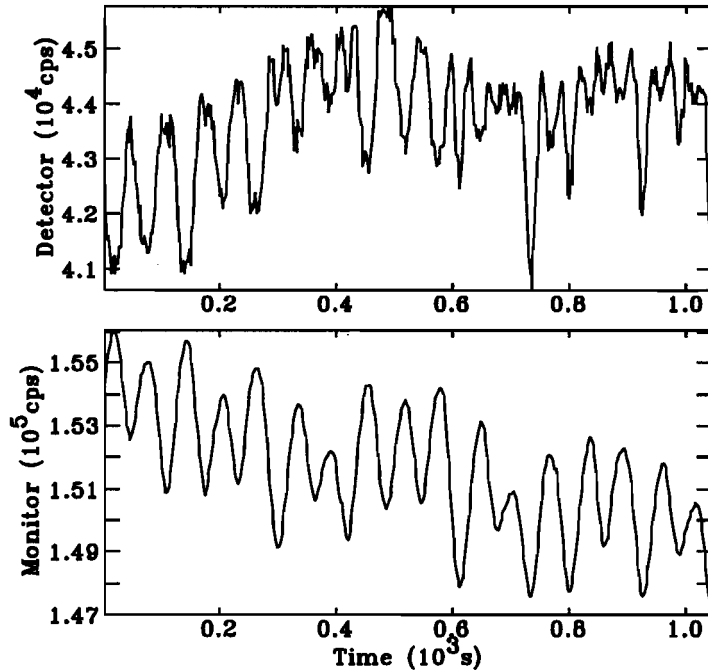


Figure 4.6: (Top) Time fluctuations of the total flux transmitted through a $3.5 \mu\text{m}$ pinhole. The upstream slits were wide open for this measurement. (Bottom) The ion chamber monitor signal at X-25 before the pinhole. Fluctuations with a period of 62.5 s are present in the incident beam and the transmitted beam.

and the transmitted beam through the pinhole in Fig. 4.6 are anti-correlated. This is very likely a sign of angular fluctuations in the incident beam, modified by the transmission through the pinhole. A Fourier analysis¹ of these fluctuations for the monitor reveals a fundamental period of 62.5 s, with some longer time scales with periods of 100 s. The detector signal shows, in addition to the frequencies found in the monitor signal, faster fluctuations with a period of 31.25 s, which is the second harmonic of the fundamental. These fluctuations appeared also in the beam position monitor signal.

Another group has observed incident intensity fluctuations at X-25 at about 25 Hz. Because, the shortest exposure was 120 s, we integrated over much of these fluctuations, reducing the amplitude of the fluctuations.

Fig. 4.7 shows two scans of the spectrometer table revealing some random structure modulating the incident beam at X-25. These length scales are approximately 20 and

¹The power spectrum of the signal was calculated numerically. The power spectrum is the square of the Fourier transform.

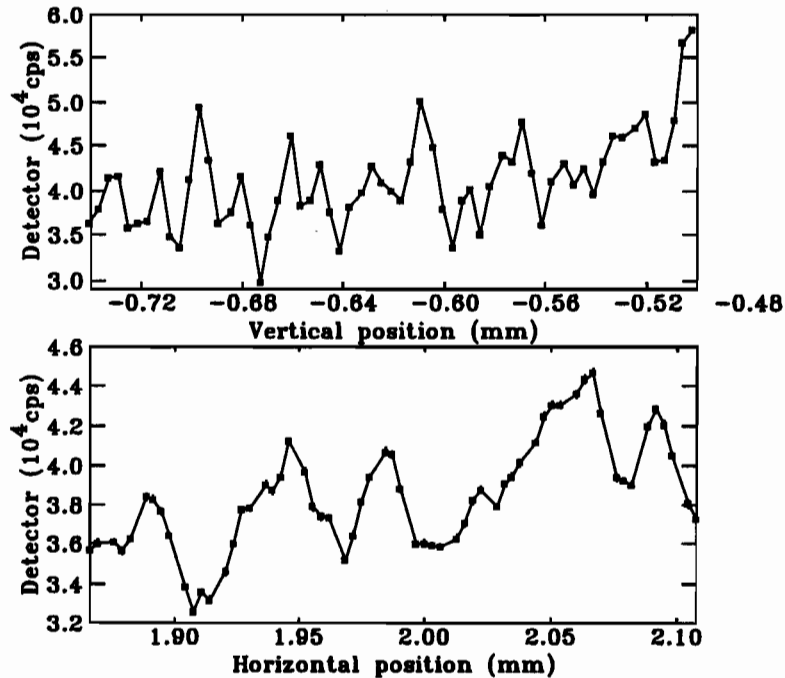


Figure 4.7: The horizontal and vertical structure of the incident beam measured by scanning the spectrometer table perpendicular to the incoming beam direction. The detector was placed behind a $3.5 \mu\text{m}$ pinhole. Scanning the spectrometer table moves the pinhole along the structure modulating the incident beam. Note that the step size is the same for both plots. This structure is narrowest in the vertical.

$40 \mu\text{m}$ in the vertical and horizontal respectively. This spatial structure is time independent. It is believed that the structure is due to either the monochromator crystal or to some Be window upstream of the pinhole. This structure in the incident beam was observed at CHESS, X25 and ESRF¹. During the experiment, the incident collimating pinhole was set on a flat region of this structure.

4.8 Temperature calibration and heat treatment

Fig. 4.8 shows a plot of the integrated intensity over an area of 380×190 pixels, as the sample is disordered from below to above T_c . The critical temperature of the order-disorder transition in Cu_3Au is $T_c = 391 \pm 1 \text{ }^\circ\text{C}$. It compares well with the critical temperature of 390°C found in the literature². Before a quench, the

¹Recently, it was found that the structure in the incident beam at ESRF was due to the small angle scattering from the monochromator Be window. This was observed on a microfocus beamline. They found that the structure observed was imaged from the Be window. By polishing this window, they also showed that the structure disappeared.

²See Warren[26], Chapter 12

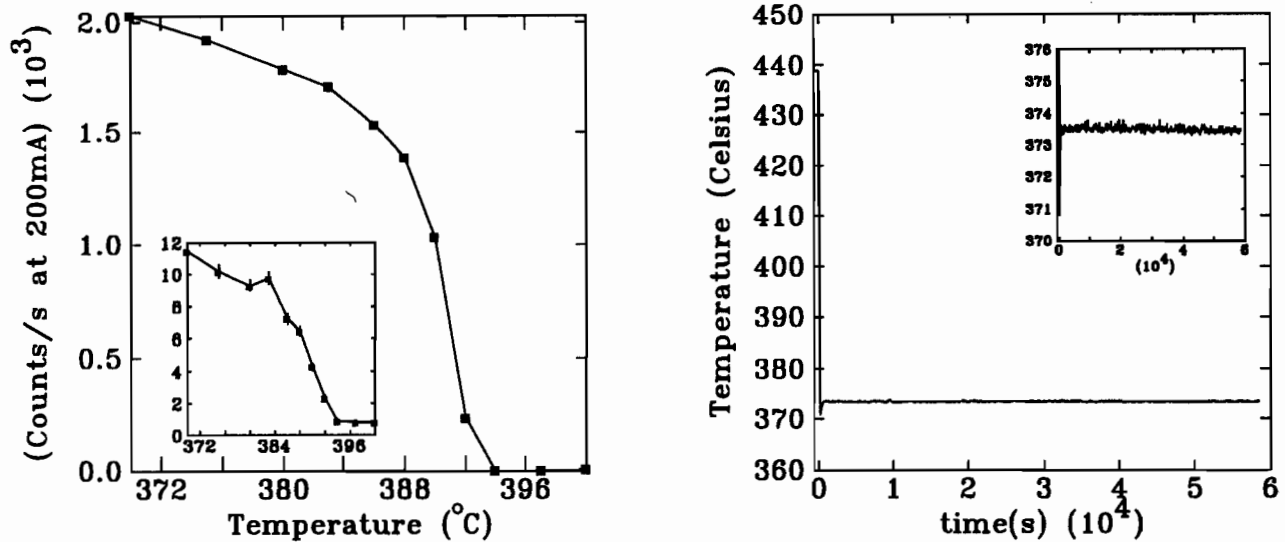


Figure 4.8: Left: Integrated intensity of $S(\vec{q})$ over an area of 380×190 pixels centered on the Cu₃Au (100) reflection versus temperature. The inset is the integrated intensity over the parasitic peak discussed in the next section. Its temperature behavior is the same as the (100) peak. Right: The quench profile for Run 21. The temperature read by the second thermocouple is displayed as a function of time after the quench. The sample was annealed near 440 °C and quenched abruptly to its final temperature. The inset shows that after an initial undershoot of 2.5 °C, the temperature is stable to within a fraction of a degree over sixteen hours.

sample was annealed above T_c to remove any long range order. At X25, the sample was annealed at 440°C and then quenched rapidly to its final temperature. Both quenches reported in this thesis for the X25 experiment were made at the same final set point temperature $T = 370$ °C, or $t = T_c - T = 21$ °C. The temperature after an initial undershoot of approximately 2.5 °C was constant within ± 0.5 °C for 20 hours (See a typical quench profile in Fig. 4.8).

At CHESS, the sample was annealed slightly above T_c and quenched to a final temperature of $t = 22$ °C. After an initial undershoot of 3 °C, the second thermometer drifted up by 5 °C during the 10 hour experiment although the setpoint temperature stayed constant. If this temperature drift is characteristic of the illuminated area, this could affect the kinetics of the ordering process.

4.9 Setting the angle of incidence θ_i

Below T_c , for θ set at the Bragg condition, the structure factor consisted of a narrow peak superimposed on a broad order-disorder peak of Cu₃Au (100). The narrow

component would move across the detector plane by scanning the angle of incidence on the sample. Changing θ_i by an angle Δ moved this peak in 2θ by 2Δ . The integrated intensity in this peak was maximized when θ was set to the Bragg angle, while the broad order-disorder peak became weaker at the Bragg condition. A radial θ - 2θ scan along the (100) had a FWHM of $\Delta\theta = 0.1^\circ$. Furthermore, this peak disappeared above T_c , which implies that it must be related to the order-disorder phase transition in Cu_3Au , and not to something like an oxide peak. Using $dq/q = \tan^{-1}(\theta)\Delta\theta$, with $\theta = 14.54^\circ$, one finds that this scattering could be caused by a surface layer approximately 500 Å thick. In the experiments reported next, the Bragg angle was offset by 0.1° , in order to look only at scattering from the bulk sample. Some fraction of the signal on the (100) is lost because of this offset.

RESULTS

5.1 *Static speckle patterns*

Fig. 5.1 shows an image of a speckle pattern of Cu_3Au , measured with $D = 7.5 \mu\text{m}$. The sample was kept at room temperature where the dynamics is frozen. The data are characterized by three well separated length scales: the speckle size and the domain sizes. It is well known that Cu_3Au superlattice peaks are disks in reciprocal space (See section 2.4). In the far field diffraction plane, regions of high intensity are next to regions of low intensity, with a typical speckle size of l_s , which is on the order of the FWHM of the Fraunhofer diffraction pattern of the pinhole given by [15]

$$l_s \approx \frac{1.0288\lambda R_d}{D}. \quad (5.1)$$

Here $R_d = 1.04 \text{ m}$ is the pinhole-detector distance, $\lambda = 1.797 \text{ \AA}$ and D is the input beam collimator diameter. The speckle angular size is given by a relative change of optical path length equal to λ [15]. Here, l_s is $25 \mu\text{m}$ or approximately a pixel wide. Note also that for a *perfectly coherent* incident beam, the speckle size goes to zero in the limit where the scattering volume goes to infinity. Therefore, it is possible to wash out the contrast if the speckle size becomes smaller than the resolution of the detector. It is important to match the detector resolution with the speckle size.

In the far field diffraction, the speckle pattern adds a random fluctuating envelope to the (100) superlattice peak caused by coherent diffraction from X-rays scattered from different antiphase domains. They are called antiphase domains because type I and II domains walls cause π phase shifts in the scattered light from the (100) since these walls are created by a relative displacement of $(1/2, 0, 1/2)\mathbf{a}$, where \mathbf{a} is the lattice

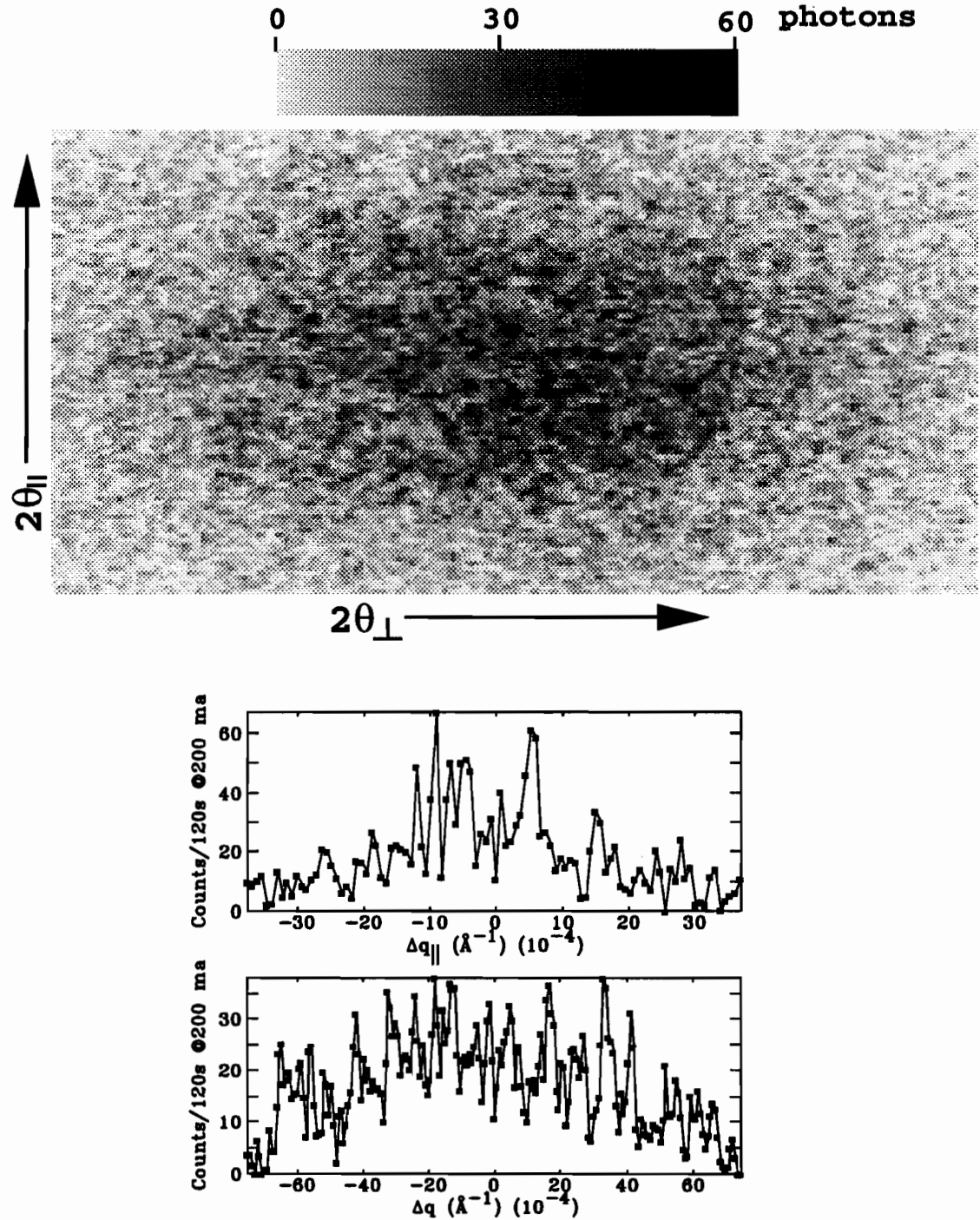


Figure 5.1: A speckle pattern of Cu_3Au (100) measured at room temperature after the sample was ordered for 16 h at 373°C . The scattered intensity in the central 200×100 pixels is displayed using the grey scale legend. The beam was collimated with a $7.5 \mu\text{m}$ pinhole and the pattern was integrated for 2 minutes. The data are scaled for beam intensity decay to a beam current of 200 mA. Below, two slices are shown, one along $2\theta_{\parallel}$ with $\Delta\vec{q} = (0, \Delta q_{\parallel})$ and one along $2\theta_{\perp}$ with $\Delta\vec{q} = (\Delta q_{\perp}, 0)$. The error bars are given by approximately $\sqrt{1.63v^*}$, as shown in Fig 3.6. To reduce the error bars, several scans can be averaged (see Fig 5.2). The spatial fluctuations are clearly above counting statistics.

constant. The superlattice peak characteristic angular size $\Delta \approx \lambda R_d / R_D$, where R_D is the average radius of an antiphase domain in Cu_3Au . In Fig. 5.1, Δ is of the order of 30 to 60 pixels, therefore the average domain size ranges from 1400 to 2800 Å. The optimum condition for observing speckle occurs when Δ is of the order of a few l_s , so that the number of speckles measured by the CCD is of the order of $(D/R_D)^2$. When $R_D > D$, one simply observes the Fraunhofer pattern of the pinhole because the sample has no disorder. This was observed in Ref. [15] on a perfect crystal of Si. If the diffuse scattering is too broad, more speckles are observed, but the scattered intensity is smaller. With current X-ray sources, one must prepare samples carefully to observe speckle. Future third generation synchrotron sources should allow for a greater variety of samples to be studied.

Another characteristic property of speckle is its very large contrast, defined as the ratio of the standard deviation of the spatial fluctuations over the spatial average. The contrast depends on two experimental conditions: the incident beam resolution and the detector resolution. A large number N_s of independent speckles in a detector area reduces the contrast by a factor $1/\sqrt{N_s}$ for a perfectly coherent incident beam. Approximating the speckle area, A_s , by a disk of radius equal to the first zero of the Fraunhofer diffraction pattern of the pinhole,

$$A_s = \pi \left(\frac{1.22\lambda R_d}{D} \right)^2, \quad (5.2)$$

one finds the number of speckles in a detector area A_d

$$N_s = \frac{A_d}{A_s} = \frac{A_d D^2}{\pi (1.22\lambda R_d)^2}. \quad (5.3)$$

Since $N_s \propto D^2$, the contrast is proportional to $1/D$ for a fixed detector area, thus increasing the pinhole diameter reduces the contrast.

The incident beam resolution is related to the degree of coherence of the beam, measured by the ratio of the beam size over the transverse coherence lengths l_x, l_y . Here, the sample size is controlled by the collimating pinhole diameter D . Increasing l_x, l_y or reducing D improves the contrast. A useful parameter for determining the contrast is the number of coherence areas $A_c = l_x l_y$ in the collimating pinhole area

given by

$$N_c = \frac{\pi D^2}{4l_x l_y}. \quad (5.4)$$

The contrast increases as N_c decreases.

To demonstrate these concepts, we performed an experiment which consisted of changing l_x and D independently. The horizontal transverse coherence length l_x was increased by closing the source x-y slits, thus reducing the effective source size d_s (See Fig 2.4). Only l_x was changed because the horizontal source size of synchrotron radiation is typically an order of magnitude larger than the vertical source size, resulting in l_x being the smallest of the two coherence lengths.

Fig. 5.2 shows slices of the speckle pattern for different D and source sizes. This experiment was performed at X-25, with a ring current ranging from 210 to 150 mA. The CCD was oriented at the time with its poor resolution direction along $2\Theta_{\parallel}$. The horizontal source size was reduced by closing the upstream slits which are 10.5 m from the source, from an opening of 2 mm to 0.31 mm. This reduced the incident intensity by approximately 2/3. The CCD was exposed for 30 to 240 s. To improve the counting statistics, many scans were averaged for a total time ranging from 20 minutes to an hour. Slices through the time averages along $2\Theta_{\perp}$ and $2\Theta_{\parallel}$ are shown. As expected theoretically, the speckle pattern spatial fluctuations increase as D is reduced while keeping l_x constant, and are increased when the source size is reduced keeping D constant. The error bars are much smaller than the spatial fluctuations of the signal for all optical conditions. This will be shown later with Fig 5.9. Note that here the peak average count rate is proportional to the pinhole area and slit opening. The contrasts along both scan directions are very similar. Some of the scans along $2\Theta_{\parallel}$ may have less contrast than their respective scans along $2\Theta_{\perp}$ because the CCD resolution is poorer along this direction.

Fig 5.1 and 5.2 show that the contrast and speckle size of the observed speckle pattern are qualitatively consistent with the theoretical properties of speckle. To measure these properties quantitatively, in the next two sections we develop tools which will help to measure the contrast and speckle size of a given speckle pattern.

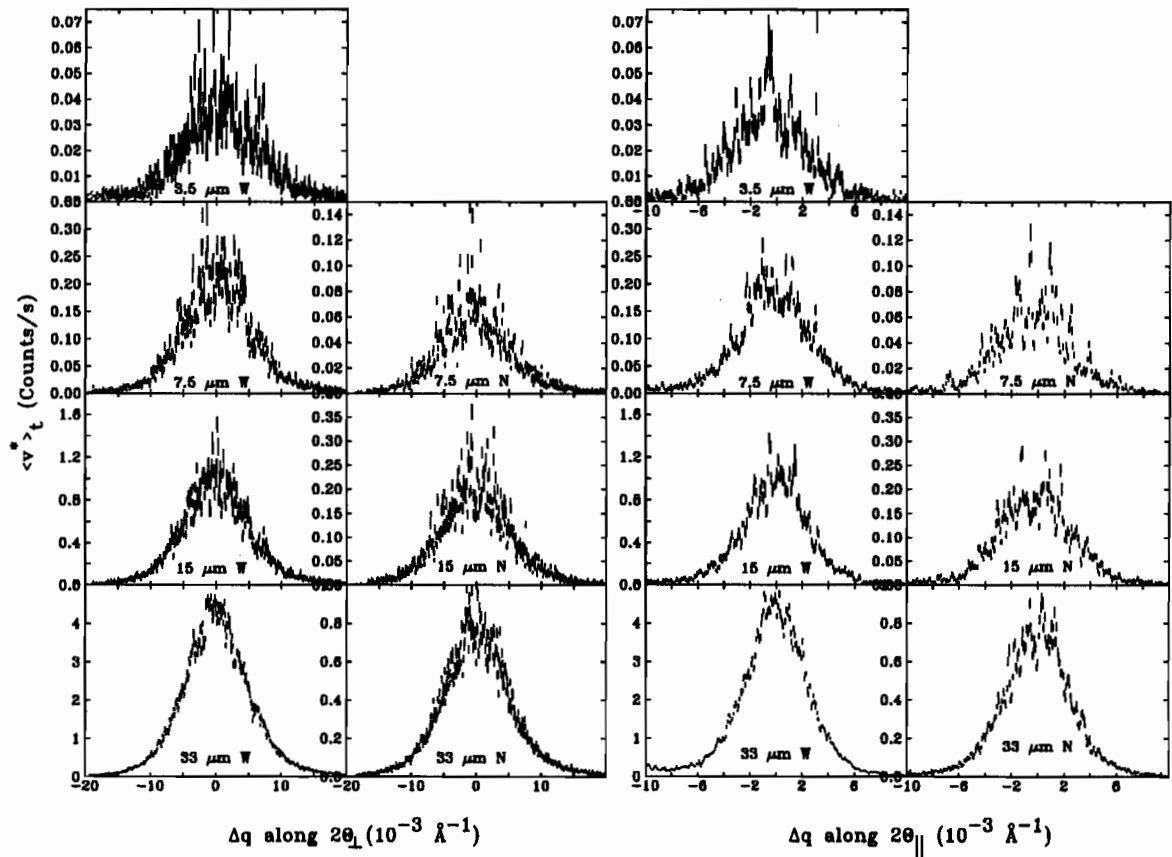


Figure 5.2: Slices along $2\Theta_{\perp}$ and $2\Theta_{\parallel}$ of the time averaged speckle pattern of Cu_3Au (100) at 300 K, where no coarsening dynamics is expected. The labels indicate the pinhole diameter used and status of the upstream slits: narrow (N) or wide (W). The setup with $D = 3.5 \mu\text{m}$ and narrow slits was not measured because of the long integration time needed. The error bars were calculated from Eq. A.14 using the measured variance of N exposures. As discussed in the text, the contrast is reduced when the diameter of the collimating pinhole D is increased at constant incident source size, and is increased by reducing the source size at constant D . Scans along $2\Theta_{\perp}$ and $2\Theta_{\parallel}$ have very similar contrasts.

These tools could not be used as effectively without a two dimensional data set. This is the main advantage of measuring speckle patterns with a CCD. Here, one can calculate different statistical estimators which describe quantitatively the speckle pattern properties. These estimators will have excellent statistics because the CCD records 2.2×10^5 pixel elements simultaneously, compared to one element for a standard detector. For example, Fig 5.1 would have taken 666 hours of valuable synchrotron beam time to record by scanning a scintillation counter over the same area, or 3.3 hours by scanning a $25 \mu\text{m}$ slit in front of the one-dimensional linear diode array discussed earlier in section 3.0.4.

5.1.1 Measuring speckle size

To quantify the three length scales of speckle patterns, we will use a more general form of the spatial correlation introduced earlier in Eq. 3.21. The crosscorrelation function of the scattered X-rays is defined¹ by

$$\Gamma(\vec{\Delta}q, t, \Delta t) \equiv \langle v^*(\vec{q}, t)v^*(\vec{q} + \vec{\Delta}q, t + \Delta t) \rangle_{\vec{q}}. \quad (5.5)$$

The linearized signal v^* , defined in Eq. 3.20, is measured at wavevector \vec{q} and time t , where q_{ij} and t_k are discrete due to the nature of the detection process. The integers i and j are indexes for the rows and columns of the CCD; v^* is integrated from t to $t + \tau$. Let us first understand the autocorrelation function by setting Δt to zero. An image of $\Gamma(\vec{\Delta}q, t, 0)$ is shown in Fig. 5.3 for a typical speckle pattern measured with a $7.5 \mu\text{m}$ pinhole. Two perpendicular slices of Γ are also shown in Fig. 5.4. The autocorrelation consists of two peaks with well separated length scales. One peak has a width of the order of tens of pixels, caused by the envelope of scattering previously discussed. The central peak is related to the speckle pattern convolved with the detector's response autocorrelation. As shown in the inset of Fig. 5.4 and the enlarged central peak area in Fig 5.3, the scattering is well correlated on a distance of 1-2 pixels.

¹It is calculated numerically by $\Gamma(\vec{\Delta}q, t, \Delta t) = \text{fft}^{-1}(\text{fft}(v(t))\text{fft}^*(v(t + dt)))$, where the fft is a spatial Fast Fourier Transform. It can be calculated also directly by evaluating the sums described on page IX. Both methods are equivalent.

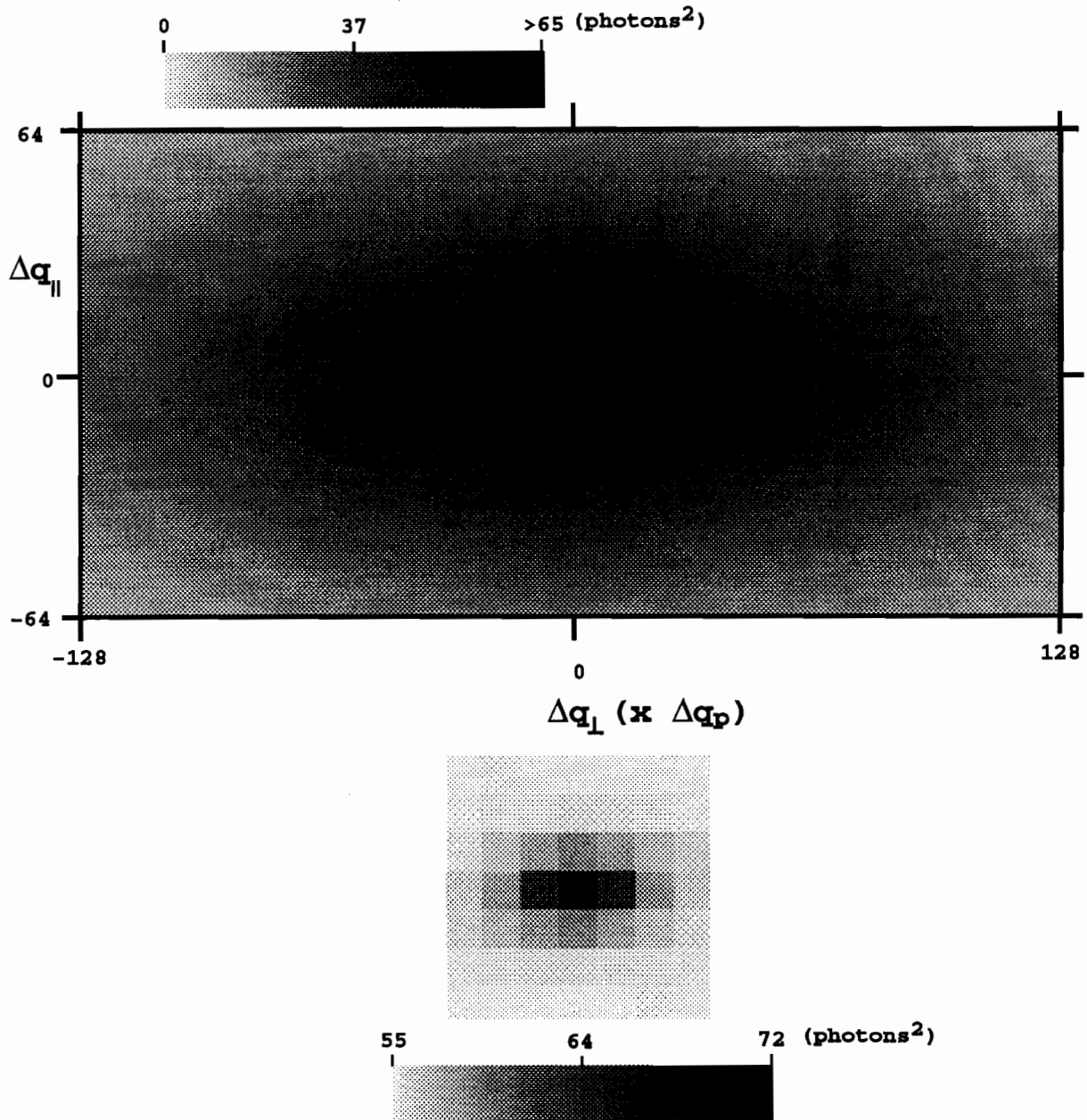


Figure 5.3: A typical autocorrelation function $\Gamma(\vec{\Delta}q, t, 0)$ of the (100) superlattice peak of Cu_3Au . A linear grey scale between 0 and 65 photons² is used for displaying Γ , and a pixel subtends a $\Delta q_p = 7.53 \times 10^{-5} \text{ \AA}$. Below, the central 7×7 pixels of Γ with its color legend. The central peak is related to the speckle size convolved with the detector pixel to pixel correlation.

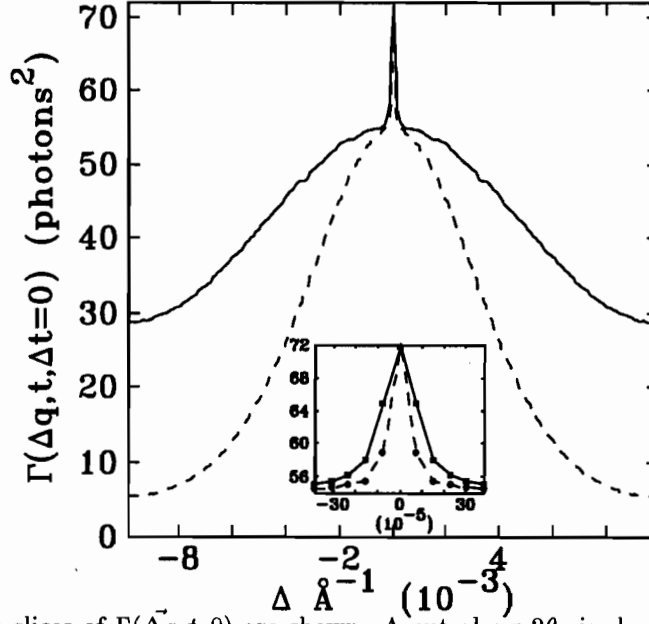


Figure 5.4: Two slices of $\Gamma(\vec{\Delta}q, t, 0)$ are shown. A cut along $2\theta_{\parallel}$ is shown with a dashed line with $\vec{\Delta}q = (0, \Delta)$, and a cut along $2\theta_{\perp}$ with $\vec{\Delta}q = (\Delta, 0)$ is displayed with a solid line. The width of the diffraction pattern is about twice as narrow along $2\theta_{\parallel}$. This difference is explained in section 2.4, where it is shown that the structure factor is pancake-like in reciprocal space. The inset shows the peak near $\Delta q \approx 0$. The width of the peak is narrower along $2\theta_{\parallel}$ because the detector resolution is better in this direction. Note that the autocorrelation is symmetric with respect to the origin by definition.

To understand $\Gamma(\vec{\Delta}q, t, 0)$ quantitatively, let us first illuminate the detector with a spatially uniform source of incoherent X-rays with spatial average $\langle v^* \rangle_{\vec{q}}$. We have shown in section 3.0.5, Fig 3.10, that

$$\Gamma_D(\langle v^* \rangle, \vec{\Delta}q) - \langle v^* \rangle_{\vec{q}}^2 \approx \begin{cases} 1.63 \langle v^* \rangle_{\vec{q}}, & \text{for } \vec{\Delta}q = 0, \\ 0.85 \langle v^* \rangle_{\vec{q}}, & \text{for } \vec{\Delta}q = (\Delta q_p, 0), \\ 0.2 \langle v^* \rangle_{\vec{q}}, & \text{for } \vec{\Delta}q = (0, \Delta q_p), \\ 0.13 \langle v^* \rangle_{\vec{q}}, & \text{for } \vec{\Delta}q = (2\Delta q_p, 0), \\ 0.11 \langle v^* \rangle_{\vec{q}}, & \text{for } \vec{\Delta}q = (\pm \Delta q_s, \pm \Delta q_p), \\ 0 & \text{otherwise.} \end{cases} \quad (5.6)$$

Here Δq_p is the magnitude of the wavevector difference between two nearest neighbor pixels. Using $S_{v^*, \vec{q}}^2 \approx 1.63 \langle v^* \rangle_{\vec{q}}$, it is easy to derive Eq. 5.6 from Eq. 3.21. The detector autocorrelation Γ_D is due to the spreading of the electric charge from a detected photon over several pixels. Fig. 5.5 and 3.10 show slices along q_{\perp} and q_{\parallel} of Γ_D for a spatially uniform detected beam. The CCD has a narrower resolution

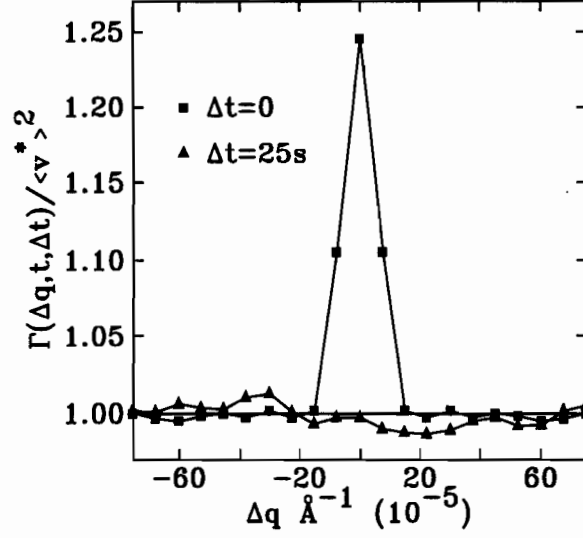


Figure 5.5: With squares, a typical slice of the autocorrelation function $\Gamma_D = \langle v^*(\vec{q}, t)v^*(\vec{q} + \vec{\Delta q}, t + \Delta t) \rangle_{\vec{q}}$ for $\Delta t = 0$ measured by illuminating the detector with spatially uniform incoherent X-rays is shown. Γ_D has been normalized to $\langle v^* \rangle^2$, the square of the spatial average of v^* . The amplitude of the peak is $1 + \frac{S_{\vec{q}, v^*}^2}{\langle v^* \rangle^2}$, where $S_{\vec{q}, v^*}^2$ is the spatial variance of v^* . A slice of the cross correlation function of two successive scans of the CCD detector is also shown with triangles, showing no correlation. When one needs to evaluate the speckle size, the cross correlation function has the advantage of removing the Poisson term in the right hand side of Eq. 5.6.

along the parallel transfer direction, here referred to as q_{\parallel} . This explains why the width of the speckle contribution is different in the q_{\perp} and q_{\parallel} directions in the inset of Fig. 5.4. If the detector is illuminated with a speckle pattern, $\Gamma(\vec{\Delta q}, t, 0)$ will contain a contribution due to the Poisson noise in the measured v^* coupled to the finite resolution of the detector, and one from the high contrast speckle pattern. To measure the speckle contribution, we must subtract this Poisson contribution from the detected correlation function, i.e.

$$\Gamma_s(\vec{\Delta q}, t, 0) = \Gamma(\vec{\Delta q}, t, 0) - \Gamma_D(\langle v^* \rangle_{\vec{q}}, \vec{\Delta q}), \quad (5.7)$$

where Γ_s is the speckle contribution. This treatment can be simplified further if we cross-correlate two successive speckle patterns, by approximating

$$\Gamma_s(\vec{\Delta q}, t, 0) \approx \Gamma(\vec{\Delta q}, t, \Delta t) = \langle v^*(\vec{q}, t)v^*(\vec{q} + \vec{\Delta q}, t + \Delta t) \rangle_{\vec{q}}, \quad (5.8)$$

where Δt is small compared to the time scale of any intensity fluctuations. In our case, this is a valid assumption since the dynamics is frozen for a sample at room temperature. Then the variance term in Eq. 5.6 due to Poisson noise disappears

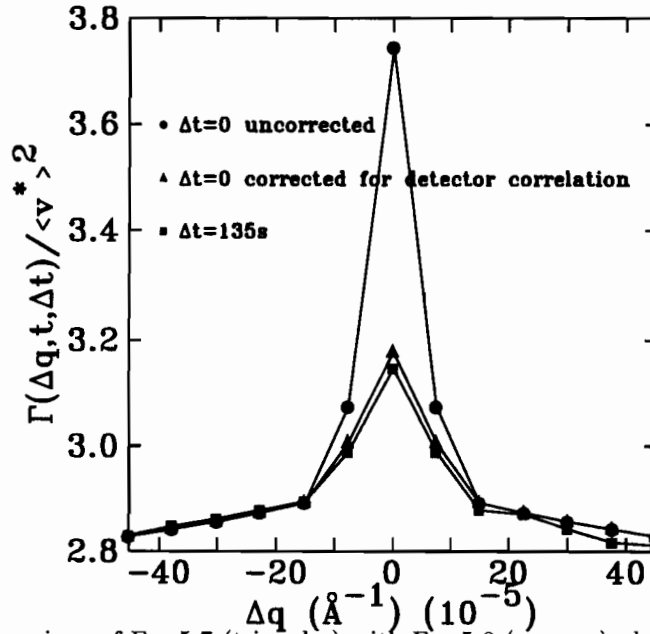


Figure 5.6: Comparison of Eq. 5.7 (triangles) with Eq. 5.8 (squares) along $2\Theta_{\parallel}$ for a static speckle pattern of Cu_3Au . The autocorrelation calculated from Eq. 5.5 is shown for comparison with circles. Note that the speckle pattern remains constant for 135 s since both equations yield the same Γ_s .

because $v^*(\vec{q}, t)$ and $v^*(\vec{q}, t + \Delta t)$ are independent. The treatment is also simpler since we do not need to take into account the Poisson contribution caused by the couplings between neighboring detectors, or pixels.

As shown in Fig 5.5, the cross correlation of two spatially uniform patterns does not show the excess correlation at $\Delta q = 0, \pm 1, \pm 2 \Delta q_p$. There is no memory between different scans of the CCD detector. Furthermore, this tool is quite powerful in detecting any scattered beam motion. Fig. 5.6 shows the equivalence between Eq. 5.7 and Eq. 5.8. This also shows that the speckle pattern is unchanged after 135 s, which is a sign of good mechanical and optical stability of the experimental setup over this time period. Note that the Poisson and detector contribution in Eq. 5.7 could be also taken out by averaging the signal over N independent scans of the detector and then calculating Γ_s with

$$\Gamma_s(\vec{\Delta}q, t, 0) \approx \langle \langle v^*(\vec{q} + \vec{\Delta}q, t) \rangle_t \langle v^*(\vec{q}, t) \rangle_t \rangle_{\vec{q}}. \quad (5.9)$$

In Eq. 5.6, the right hand side would then be divided by N because the error on a time average is reduced by \sqrt{N} , thus reducing the Poisson contribution.

Using Eq. 5.8, we can now estimate the speckle size in Fig. 5.1 and 5.2. If one

assumes a point source illumination of the sample, the speckle size should be inversely proportional to the beam size. Fig 5.7 shows the crosscorrelation of two subsequent speckle patterns shown for different optical conditions. The correlation function was calculated using a window of 256 by 512 pixels which covers most of the data. Two effects are observed. As the pinhole diameter increases, the speckle size is reduced and the autocorrelation function becomes resolution limited. For example, for the wide open slits, the peak along $2\Theta_{\parallel}$ subtends 9 points for the $3.5 \mu\text{m}$ pinhole but only 4 points for the $33 \mu\text{m}$ pinhole. Another indication of the resolution limit is seen for the data with narrow slits, since for $D = 15$ and $33 \mu\text{m}$, the peak is the narrowest along $2\Theta_{\perp}$, the direction of high resolution on the CCD.

Another feature in Fig. 5.7 is the baseline shifts. For example, the crosscorrelation decays from a maximum of 2.9 to 2.6 for $D = 3.5 \mu\text{m}$ (W), but decays from 3.93 to 3.6 for $D = 7.5 \mu\text{m}$ (W). This baseline shift is caused by a change of the FWHM of the (100). This change of FWHM was measured by fitting the data to a two dimensional Gaussian later introduced in Eq. 5.11. It was found that the (100) is wider for smaller pinholes. For example, the fitted widths σ_{\parallel} and σ_{\perp} decrease by 19 % when the input pinhole diameter is increased from $D = 3.5$ to $33 \mu\text{m}$ with wide open upstream slits. It is shown in section A.3 that the maximum of the spatial autocorrelation function for a two dimensional Gaussian representing the incoherent scattering is inversely proportional to the product of the fitted widths σ_{\perp} and σ_{\parallel} . In Fig. 5.8, the baseline of the correlation function, taken as the value of the crosscorrelation function along $2\theta_{\perp}$ after the decay due to speckle, is plotted versus the inverse of the product of the fitted widths. The baseline shift is proportional to $1/(\sigma_{\perp}\sigma_{\parallel})$, in good agreement with the prediction found in Eq. A.35.

This dependence of the FWHM of the Cu_3Au (100) on the pinhole diameter D is very surprising. It is present in both data sets with open and closed upstream source slits. No coarsening dynamics occurred during this experiment since the sample was at 300 K. These measurements were performed with record incident and scattered wavevector resolutions. These measurements are micro-diffraction experiments on

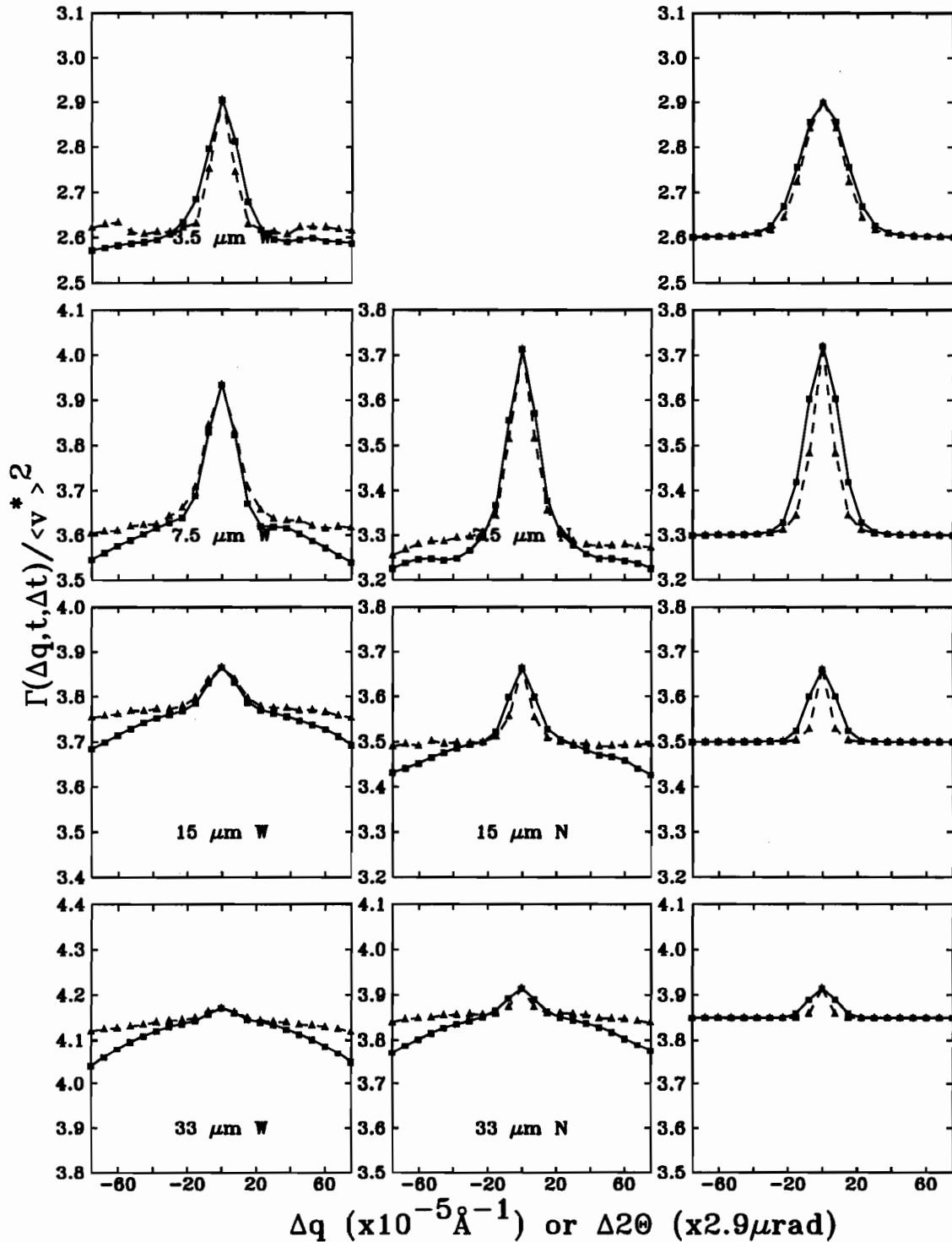


Figure 5.7: The effect of varying the collimating pinhole diameter, D , and the horizontal source size on the speckle size. The solid and dashed curves are respectively slices of the cross-correlation function between two subsequent exposures of the CCD along $2\Theta_{\parallel}$ and $2\Theta_{\perp}$ for wide (first column) and narrow source slits (second column). The speckle size increases as D is reduced for a given slit setting. Far away from $\Delta\vec{q} = 0$, the correlation function decays faster along $2\Theta_{\parallel}$ because the peak is narrower along this direction. The autocorrelation of a Fraunhofer diffraction pattern of a circular pinhole, convolved with the detector resolution is shown in the third column. The peak height and baseline were adjusted to match the values found in the data set with narrow slits along $2\Theta_{\perp}$. The pinhole diameter varies from 3.5 to 33 μm , and slices along $2\Theta_{\perp}$ and $2\Theta_{\parallel}$ are shown respectively with dashed and solid lines. The spatial autocorrelation function of an ideal Fraunhofer diffraction pattern of the pinhole is in good agreement with the observed autocorrelation of speckle patterns for narrow slits.

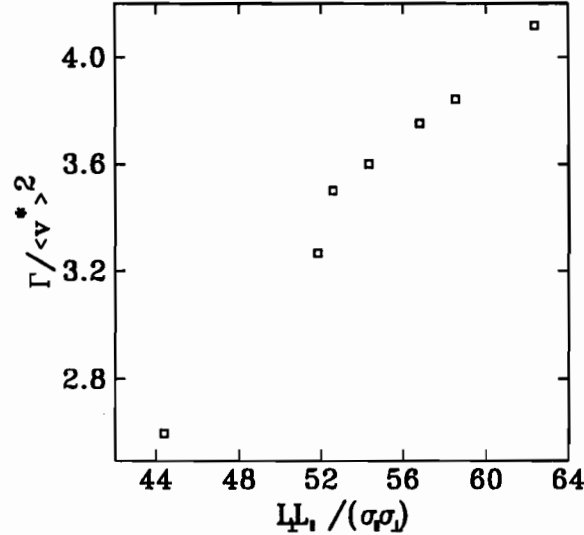


Figure 5.8: The inverse of the product of the fitted widths σ_{\perp} and σ_{\parallel} versus the maximum of the correlation function. L_{\perp} and L_{\parallel} are the dimensions of the rectangle in reciprocal space used to calculate the crosscorrelation function.

very small volumes of Cu_3Au . Since the FWHM decreases with increasing D , we speculate that by illuminating a larger volume of the sample, more large antiphase domains become fully illuminated. Therefore, a larger illuminated volume would better sample the *large domain tail* of the domain size distribution, resulting in a decrease of the average domain size measured by the FWHM of the peak.

This effect is reminiscent of another effect observed in single crystals of Cu_3Au and Fe_3Al . We have observed that by illuminating different parts of the sample with a given pinhole diameter¹, the intensity and FWHM of the superlattice peak varies. To optimize the scattering condition, we move the collimating pinhole over the crystal until a well ordered volume is found.

Since Sutton et al. [15] showed that the speckle size is proportional to the FWHM of the Fraunhofer diffraction pattern of a pinhole (see Eq 5.1), a natural way to understand the behavior of Fig 5.7 is to use the autocorrelation of the diffraction pattern of a pinhole as a theoretical estimate. The third column of plots in Fig. 5.7 shows the expected autocorrelation function of a Fraunhofer diffraction pattern of a circular pinhole, illuminated by a point source placed far away from the pinhole. The diffraction pattern was convolved with the detector resolution discussed in Chapter 3

¹The collimating pinhole can be moved easily using two perpendicular high resolution Klinger motors.

and then autocorrelated. For large D , the speckle size is larger along $2\Theta_{\parallel}$ than $2\Theta_{\perp}$, which implies that the speckle peak becomes resolution limited like the experimental data for narrow slits. The theoretical model better fits the data with narrow slits because the experimental condition is closer to the theoretical assumptions. Some differences between the data and theory are observed for $D = 3.5 \mu\text{m}$, where the measured correlation function for the data with wide open slits decays faster than the model. The measured data are narrower than the model. Perhaps some of this difference is caused by the fact that the Cu_3Au illuminated area is larger than the pinhole area since the sample is nearly outside the near-field diffraction of the $3.5 \mu\text{m}$ pinhole (see section 4.1).

The other noticeable effect is that closing the horizontal slits reduces the FWHM horizontally. For a given diameter D , slices along $2\Theta_{\perp}$ becomes narrower than those along $2\Theta_{\parallel}$. This effect is small but does not depend on the method of calculation. The same result is also obtained using Eq. 5.9 on the data of Fig 5.2, or by cross correlating other sets of subsequent files. This is consistent with the FWHM of the diffraction pattern being input divergence limited when the slits are wide open, to becoming diffraction limited for narrow slits. The horizontal FWHM of the source image in the detector plane for wide slits, Δ_x , is approximately equal to $d_{sx}R_d/R_s$, where the horizontal FWHM of the source $d_{sx} = 0.91 \text{ mm}$ and the distance slit-pinhole $R_s = 17.3 \text{ m}$. Here $\Delta_x = 55$ and $19 \mu\text{m}$ for wide and narrow slits respectively. Adding this geometrical optics effect to the FWHM of the diffraction pattern for a $7.5 \mu\text{m}$ pinhole shown in Eq. 4.4, gives an approximate FWHM of $55 + 24 \mu\text{m}$, and $19 + 24 \mu\text{m}$ for the wide and narrow slits respectively. This predicts a 45 % reduction of the FWHM of the speckle size by closing the horizontal slits. The measured reductions in the FWHM along $2\Theta_{\perp}$ in Fig. 5.2 are 20, 45 and 55 % reductions for the 7.5, 15 and 33 μm pinhole respectively. The difference between the measured and predicted change for the $7.5 \mu\text{m}$ pinhole may be caused by the resolution of the detector which has not been included in the calculation. Note that these effects will be easier to see in future experiments, by choosing a CCD array with finer resolution, or by placing

the detector two or three meters away from the pinhole.

5.1.2 Contrast

We measure the contrast of the speckle pattern by

$$Ct(A, \vec{q}) \equiv \sqrt{\frac{S_{A,v^*}^2(\vec{q}) - \langle S_{t,v^*}^2 \rangle_A}{\langle v^*(\vec{q}, t) \rangle_A^2}}, \quad (5.10)$$

where the spatial variance $S_{A,v^*}^2(\vec{q})$ and mean $\langle v^*(\vec{q}, t) \rangle_A$ are evaluated at a given time, on a small area in q-space, A. The contrast might depend on the size of the area chosen, and on the average \vec{q} vector at the center of A. For an ideal speckle pattern, one expects the contrast to be independent of the reciprocal space position. A very large window would increase the contrast artificially because the peak line shape varies across A. A very small window would poorly sample the spatial fluctuations. For the measurement shown next in Fig 5.9, a rectangular window with a width of 20 pixels along $2\Theta_{\parallel}$ and height of 40 pixels covering approximately 25 % of the Cu_3Au peak FWHM was chosen to match the Cu_3Au peak asymmetry¹. Using Eq. 5.3, with a detector area $A_s = (22.4 \mu\text{m})^2$, one finds that the window chosen includes approximately 30 independent speckles for the $3.5 \mu\text{m}$ pinhole and 2700 for the $33 \mu\text{m}$ one. Thus for a given window size, we expect the standard deviation of the measured contrast for a small pinhole to be larger than for a large pinhole because one samples more independent speckles in the latter experimental condition.

In Eq. 5.10, $S_{t,v^*}^2(\vec{q})$, the variance calculated from a time sequence of measurements at \vec{q} , is a Poisson noise contribution subtracted from S_{A,v^*}^2 . Because we do not expect any dynamics from the sample, S_{t,v^*}^2 is due to counting statistics, incident beam intensity fluctuations and any electronic noise from the detector. With this definition, when the scattering is incoherent and no speckle is present, the contrast goes to zero since the spatial fluctuations should be equal to the spatial average of the time fluctuations in Eq. 5.10.

Fig. 5.9 shows the speckle pattern contrast for various pinhole diameters and two upstream horizontal slit settings shown in Fig 5.2. The contrast increases as D

¹A square window of 20×20 pixels gave similar results.

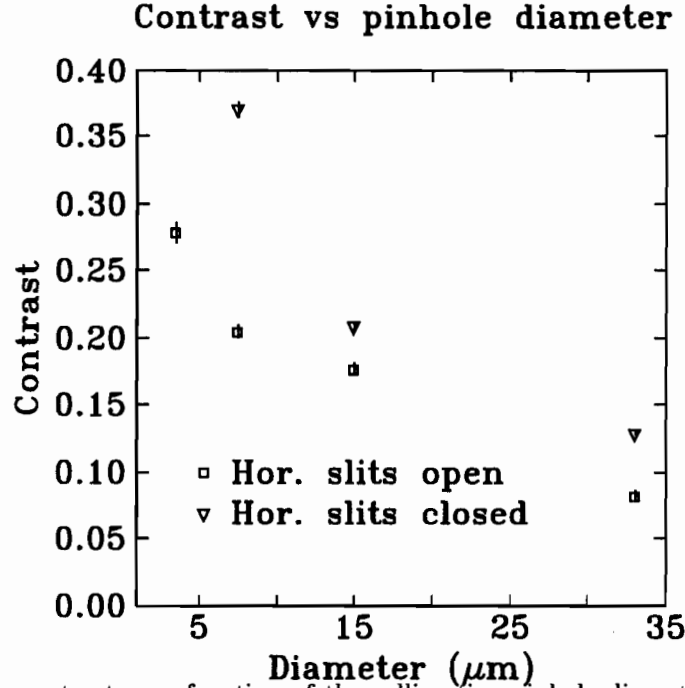


Figure 5.9: The contrast as a function of the collimating pinhole diameter D , as computed from Eq. 5.10. Two data sets are shown for open horizontal slits (2mm) and closed horizontal slits (0.31mm). Closing the horizontal slits increases the contrast for a given D because it increases the horizontal coherence length l_x .

is reduced, and increases as l_x is increased. This is consistent with the statistical properties of speckle. Note also that the contrast in Fig. 5.9 is proportional to the amplitude of the decay of the crosscorrelation function in Fig. 5.7. For example, for $D = 3.5 \mu\text{m}$ (W), the crosscorrelation in Fig. 5.7 decays from a maximum of 2.9 to 2.6, thus $\sqrt{(2.9 - 2.6)/2.6} = 0.34$, which compares reasonably well with a contrast of 0.28 found in Fig. 5.9.

The measured contrast for Cu_3Au seems lower than expected. The contrast for an ideal speckle pattern is one. Let us calculate, for example, the contrast for $D = 7.5 \mu\text{m}$, and closed horizontal slits. At NSLS, the vertical coherence length is much larger than D . The horizontal transverse coherence length is $l_x = \lambda R_s / 2d_s$, where R_s is 17.3 m, $\lambda = 1.797 \text{ \AA}$, and $d_s = 0.31\text{mm}$. Here $l_x = 5 \mu\text{m}$ is smaller than the pinhole diameter D , thus some contrast is lost in the horizontal. One expects the contrast to drop from one to $\approx \sqrt{l_x/D} = 0.82$. In Cu_3Au , the longitudinal coherence condition is satisfied, so no contrast should be lost. Another loss of contrast will be caused by averaging many speckles in a detector area. Using Eq. 5.3, the number

of speckles in the *effective* detector area, assumed to be approximately two pixels along the serial transfer direction and one pixel along the parallel transfer direction of the CCD, using $R_d = 1.04$ m is $N_s = 0.35!$ Thus the speckles are much larger than the detector area. One would expect a contrast of 0.82 for this measurement. The measured contrast is a factor two lower than expected. This is consistent with the results of Fraunhofer diffraction of the pinholes found in Fig. 4.4 and 4.5. For example, the fringe contrast is lower than expected in Fig. 4.5. Some loss of contrast could be due to the longitudinal coherence condition (See Fig. 2.6). For a semi-infinite crystal, a small fraction of the scattered intensity will come from the bulk of the crystal below one X-ray absorption depth. For these X-rays, the longitudinal coherence condition will not be met, thus reducing the contrast. Finally for large pinhole diameters, one would expect the spatial structure on the incident beam in Fig. 4.7 to affect the spatial coherence of the beam.

One should note that the speckle pattern contrast in Fe_3Al ($\frac{1}{2}, \frac{1}{2}, \frac{1}{2}$) is comparable to the one measured in Cu_3Au . We measured recently a contrast of 0.36 for a static speckle pattern of Fe_3Al generated with nearly ideal coherent illumination [88].

5.2 Ordering kinetics of an order-disorder phase transition

The data presented next will cover quenches performed at X25 and CHESS. Two sets of experiments were performed at X25: the so called run 21, obtained with a collimating pinhole diameter $D = 7.5$ μm and an exposure time $\tau = 120$ s, and run 24 obtained with $D = 15$ μm and $\tau = 60$ s. To test the beam stability, we also performed an experiment with the sample at $T = 300$ K, where the domains are frozen using the same parameters as run 21. At CHESS, run 113 was obtained with $D = 7.5$ μm and $\tau = 114$ s. These experimental conditions are summarized in table 5.1.

Fig. 5.10 shows the data for three subsequent times after the quench in run 21. The data are displayed with a linear grey scale between 0 and 35 counts/120s, and scaled to a synchrotron ring current of 200 mA. For $t = 50589$ s, the maximum intensity

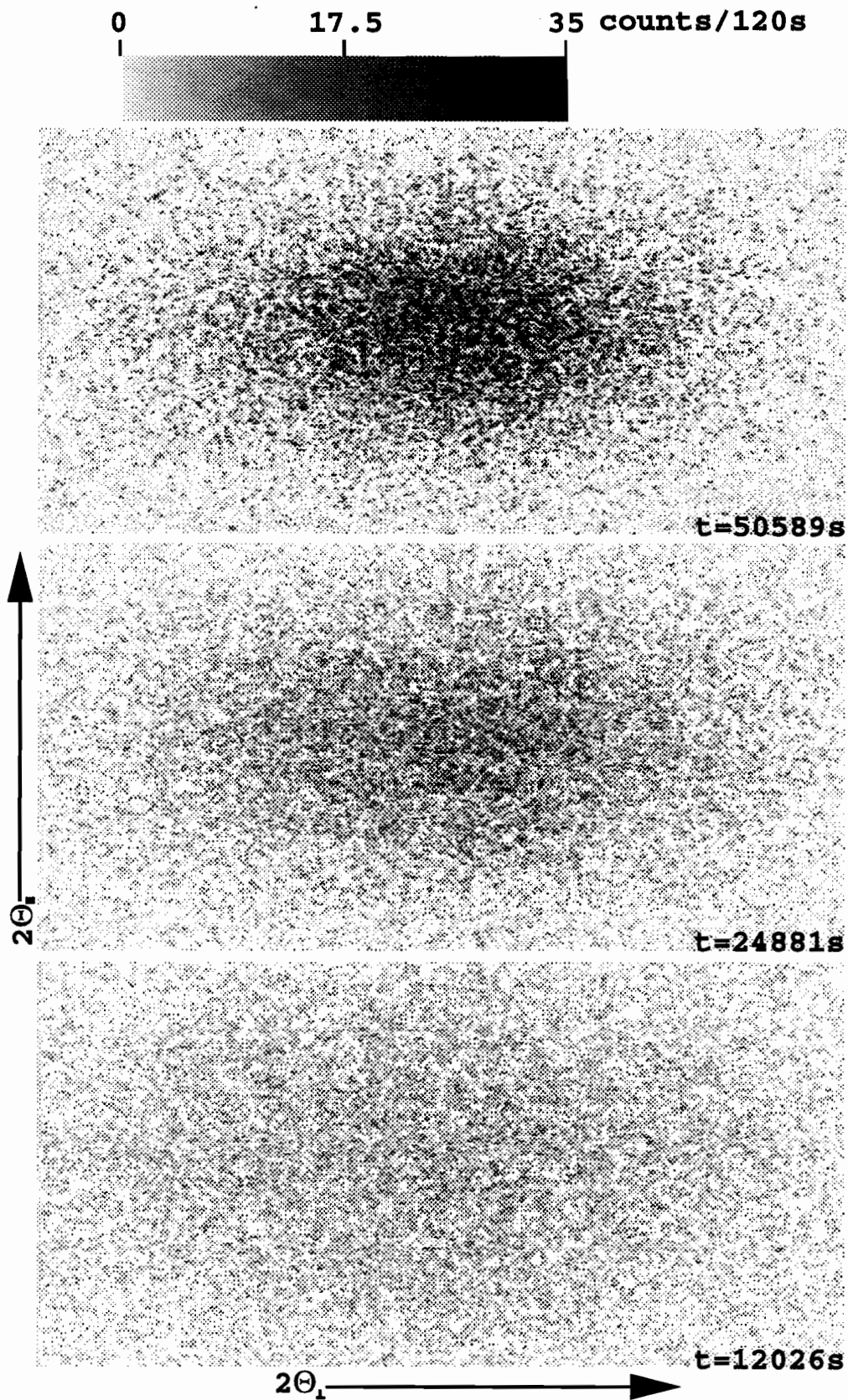


Figure 5.10: $S(\vec{q}, t)$ for $t = 1.2, 2.49, 5.06 \times 10^4$ s after the quench for run 21. The data are displayed with a linear grey scale shown above. The data span a wavevector range from the center of an image of ± 0.0136 and $\pm 0.00678 \text{ \AA}^{-1}$ along $2\theta_{\perp}$ and $2\theta_{\parallel}$ respectively. As the domains grow in time, the superlattice peak intensity increases and the peak becomes narrower in reciprocal space.

Table 5.1: Summary of the experimental parameters for different experiments. The cycling time Δt is the sum of the exposure time τ and the dead time. The experiments at X25 were performed with wide open upstream horizontal slits to optimize the scattered intensity. The contrast dependence on the sample temperature and pinhole diameter is also shown. It was calculated using Eq. 5.10 over a square of 20×20 pixels centered at $\Delta 2\theta_{\perp} = \Delta 2\theta_{\parallel} = 0$. The contrast is temperature independent for the temperatures studied in Cu_3Au .

Experiments	τ (s)	Δt (s)	D (μm)	T (K)	Contrast
Run 22	120	135.3	7.5	300	0.262 ± 0.005
Run 21	120	135.3	7.5	643	0.26 ± 0.01
Run 24	60	75.4	15	643	0.166 ± 0.006
Run 113	114	120.6	7.5	643	0.27 ± 0.01

detected is 78 counts/120s, but less than 2 % of the pixels have a count rate exceeding 35 counts/120s. These pixels are also displayed in black. Slices along $2\theta_{\perp}$ and $2\theta_{\parallel}$ are shown in Fig. 5.11 for these three different times. As expected from the coarsening of domains, the Bragg peak sharpens along $2\theta_{\perp}$ and $2\theta_{\parallel}$, and the peak intensity increases monotonically with increasing time. The solid lines in Fig. 5.11 are least-squares fits to a Gaussian defined by

$$S_f(\vec{q}, t) = I_{max}(t) \exp \left(-\frac{(q_{\perp} - Q_{\perp}(t))^2}{2\sigma_{\perp}^2(t)} - \frac{(q_{\parallel} - Q_{\parallel}(t))^2}{2\sigma_{\parallel}^2(t)} \right), \quad (5.11)$$

where $I_{max}(t)$ is the time dependent fitted peak intensity and $Q_{\perp}(t)$ and $\sigma_{\perp}(t)$ are the fit center and width along $2\theta_{\perp}$. These least-squares fits were performed on an area covering a large fraction of the two-dimensional data set¹. These fits were used to estimate the incoherent structure factor and to give a smooth average of the structure factor which could then be used in the measurements of the time fluctuations. Note that an elliptical average of the structure factor with respect to the center of mass could also have been used to define a local average. We chose the fits because they have no random spatial fluctuations.

¹The two-dimensional data set was fitted using a standard non-linear fitting routine, transforming the data into a one dimensional vector and using the independent coordinate to encode the position of the pixel on the CCD. Typically, a rectangular region of the CCD with 220 by 360 pixels was used along $2\theta_{\parallel}$ and $2\theta_{\perp}$ respectively. The data were equally weighted for the fit. A small region surrounding the parasitic peak was discarded because it dominates the scattering at early times.

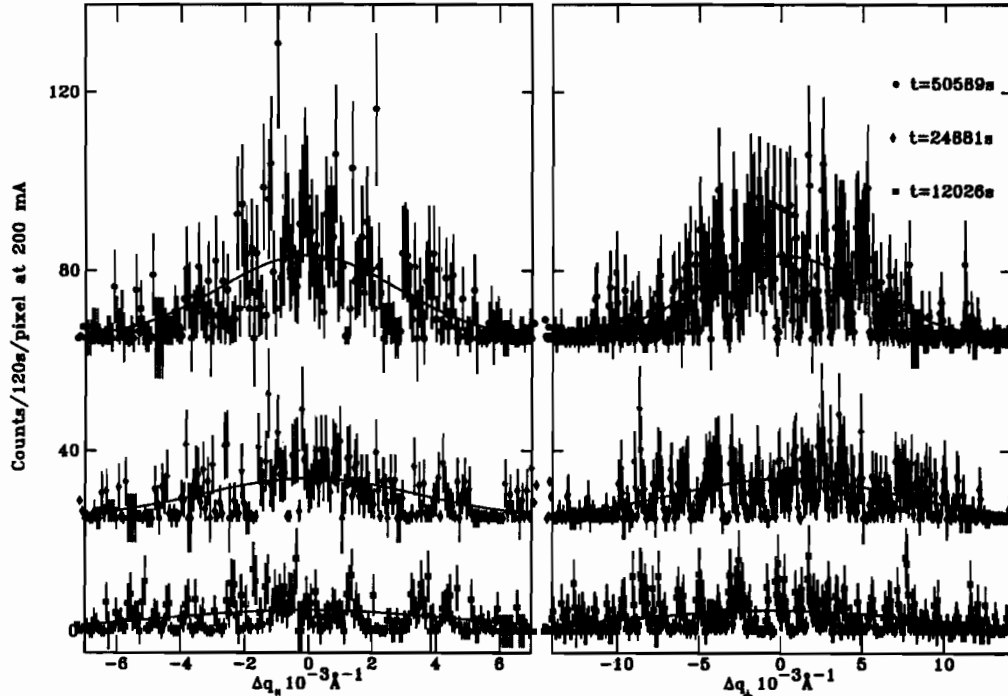


Figure 5.11: Slices of $S(\vec{q}, t)$ along $2\theta_{\perp}$ and $2\theta_{\parallel}$ for the three different times in Fig. 5.10. To distinguish the data sets, a constant of 25 and 65 counts/120s was added to the data at time $t = 24881\text{s}$ and $t = 50589\text{s}$ respectively. The solid lines are least-squares fits introduced in Eq. 5.11. These fits are used as a local average for the spatial and temporal fluctuations.

Fig. 5.12 shows the time dependence of the five fit parameters for the data. The peak intensity I_{max} at the end of run 21 is 88 % of I_{max} for run 22. The peak intensity of run 24 is approximately seven times larger than for run 21, and its calculated integrated intensity is approximately five times larger than run 21 at the same time after the quench. The CHES data are nearly 3.5 times more intense than run 21, and for an identical beam current of 200 mA, run 113 is seven times more intense than run 21. Note that an undulator was used at CHES rather than a wiggler, and that the CHES synchrotron ring energy is twice that of the NSLS ring.

In Fig. 5.12, the time average¹ of the fit center along $2\theta_{\perp}$ is $\langle Q_{\perp} \rangle_t = 209.1 \pm 7.6$, 199.5 ± 0.6 , 198.8 ± 3.4 , and 242.8 ± 2.7 pixels for run 21, 22, 24, 113 respectively. A motion of one pixel is equal to an angular motion of $\approx 22 \mu\text{rad}$. The fit center is most stable for run 22 at $T = 300\text{ K}$. During run 21, Q_{\perp} drifts by twenty pixels, or

¹The early changes in the fit parameters before $t \approx 2000\text{ s}$ were discarded from the time average because the scattering is weak at early times resulting in poorer fits. The error bars quoted are the standard deviation of the fit parameters.

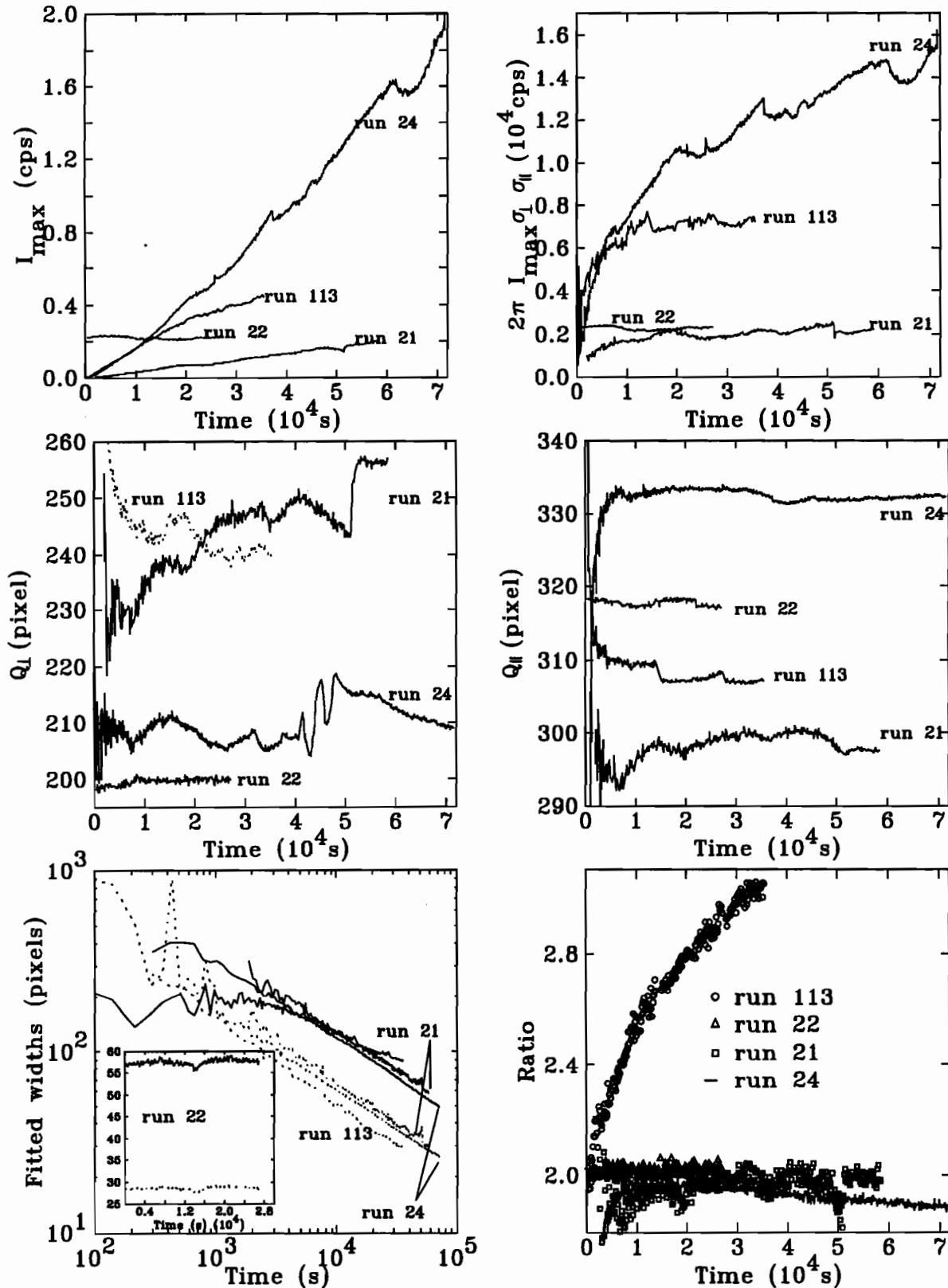


Figure 5.12: (Top left) The fitted peak intensity I_{max} for the experiments at X25 and CHES. The CHES and X25 data were scaled to a ring current of 100 and 200 mA respectively. (Top right) The calculated integrated intensity. (Middle left) The fit center Q_{\perp} . The data for run 24 and run 21 were offset by ten and thirty five for clarity. (Middle right) The fit center Q_{\parallel} . (Bottom left) The fitted widths σ_{\perp} and σ_{\parallel} are shown respectively with solid and dotted lines. The inset shows the widths for run 22 on a linear scale. (Bottom right) The ratio $\sigma_{\perp}/\sigma_{\parallel}$.

approximately 0.4 mrad, while Q_{\perp} changes abruptly after a monochromator tweak at $t = 5.11 \times 10^4$ s. For run 24, some oscillations are seen near $t = 4.1 \times 10^4$ s. These oscillations correlate with the beam position monitor.

The time averages of Q_{\parallel} in Fig. 5.12 are $\langle Q_{\parallel} \rangle_t = 298.2 \pm 1.8$, 317.8 ± 0.4 , 332.3 ± 1.4 , and 308.2 ± 1.4 for runs 21, 22, 24, 113 respectively. It is most stable for run 22. The steps seen in Q_{\parallel} for run 113 are slight motions occurring after a new synchrotron fill at CHESS. The fit center Q_{\parallel} tends to be more stable than Q_{\perp} for all the experiments reported at CHESS and X25. Since $2\theta_{\perp}$ is measured in the horizontal plane, the fact that the motions are greater along $2\theta_{\perp}$ may be due to larger incident beam motion horizontally than vertically¹.

As expected from the domain coarsening in the late time regime, the widths of the (100) in Fig. 5.12 follow a power law in both directions. For run 21, a fit of the widths to a power law, $\sigma(t) \propto t^{-n}$, yields $n = 0.43 \pm 0.01$ and 0.45 ± 0.01 for σ_{\perp} and σ_{\parallel} respectively. For run 24, $\sigma_{\perp} \propto t^{-(0.41 \pm 0.01)}$, and $\sigma_{\parallel} \propto t^{-(0.438 \pm 0.005)}$. The fitted widths along σ_{\perp} are less reliable at early times for runs 21 and 24 because $2\theta_{\perp}$ was aligned on the serial transfer direction of the CCD. The fit becomes poorer at early times because a large fraction of the scattered intensity is outside the detector window, and count rates are low. As seen in Fig. 5.12, the ratio of $\sigma_{\perp}/\sigma_{\parallel}$ is approximately two for the data recorded at X25, and it is weakly time dependent. This weak time dependence implies that the difference in the exponent of the power law for σ_{\perp} and σ_{\parallel} is significant. For run 113, the time dependence of the ratio is caused by a temperature drift of the sample of 5°C over the total time of the experiment².

The expected growth exponent for Cu_3Au is 1/2 [29, 31, 32, 33], thus our measured exponents are slightly below the exponents observed by others. The coarsening dynamics are slower along $2\theta_{\perp}$ for all the experiments performed. Previous work reported the same exponents in both directions. Since this experiment was optimized

¹At X25, it was observed that vertical motion is more constrained than horizontal motion because the two monochromator crystals are set to diffract at a given wavelength and a narrow range of incident angle [50]. A horizontal motion is not affected by such constraints.

²This temperature drift was measured in the second thermocouple used to record the sample temperature (See section 4.8).

to measure intensity fluctuations, and not growth exponents, these differences are not really surprising. It is possible that some residual non-linearities of the detector could slightly change these exponents. These fit parameters along with the contrast discussed next in table 5.1 describe the spatial dependence of the structure factor.

The time dependences of runs 24 and 113 are not shown here because they are quite similar to the ones shown in Fig 5.10 and 5.11 for run 21. Run 113 and run 21 have identical contrast within error (see Table 5.1). The main difference between the data for run 21 and run 24 is a difference in contrast due to the different pinhole diameters used. The contrast is temperature independent within error for runs 21 and 22 since they have the same D . Furthermore, the contrast measured at 300 K in Fig 5.9 using $D = 15 \mu\text{m}$ and wide open horizontal slits is 0.177 ± 0.005 , in agreement with the contrast measured for run 24.

Since very little thermal diffuse scattering is observed in Cu_3Au before a quench at the annealing temperature $T = 440^\circ\text{C}$ ¹, and no thermal diffuse scattering is observed above T_c as shown in Fig. 4.8, the observed contrast must be dominated by the speckle pattern created by domain walls for the observed temperature in Cu_3Au .

Fig. 5.13 shows the time evolution of a single row of the CCD in run 21 along δq_\perp for $\Delta 2\theta_\parallel = 0$. After the quench, speckles appear at fixed Δq_\perp , and their intensity grows monotonically in time. Some speckles can be seen in the figure as early as 1.2×10^4 s and remain present until 5.8×10^4 s, for a total time of over thirteen hours. The monochromator reset occurring near $t = 5.11 \times 10^4$ s affects the speckle pattern. Some speckles disappear, others appear, while some of the most intense remain present. The presence of the speckle over such an extended period was quite surprising initially. We were expecting to see dynamics with much shorter time scales than 10^4 s, as for a typical equilibrium IFS experiment. This difference between equilibrium and non equilibrium will be explained in more detail in the next section.

Fig. 5.14 shows a time series for run 22. This experiment was performed to test the

¹Before a quench, an upper limit for the diffuse scattering at $T = 440^\circ\text{C}$ is 0.2 counts/120s/pixel at 200 mA. This upper limit is on the order of the dark pattern fluctuations.

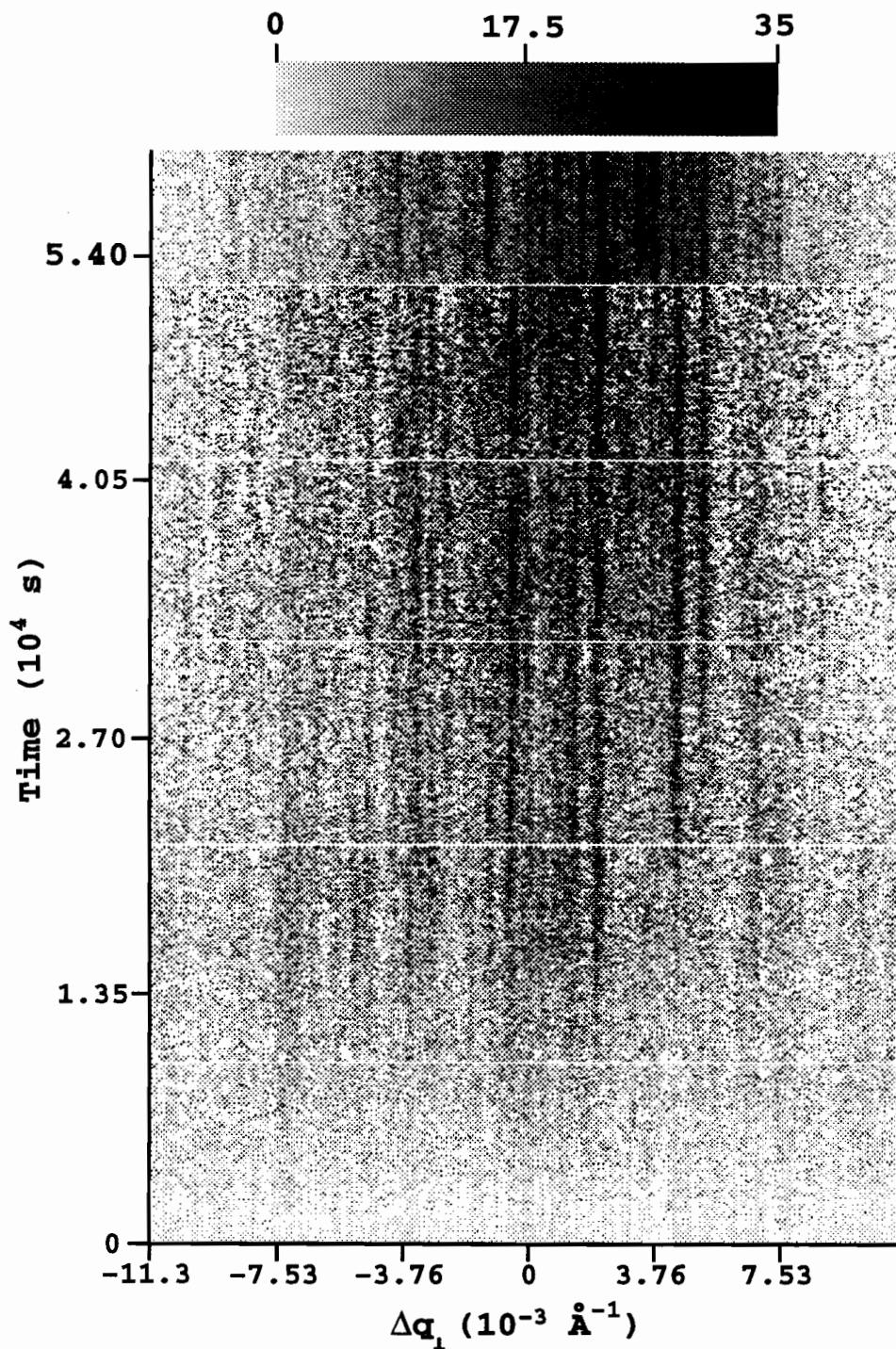


Figure 5.13: Time evolution of a single row with $\Delta 2\theta_{\parallel} = 0$. The grey scale displays the normalized data in counts/2min at 200 mA. The white horizontal lines are measurements of the dark pattern. The graininess on short time scales is caused by intensity fluctuations due to counting statistics. The spatial fluctuations along Δq_{\perp} are speckles. After the quench at $t = 0$ s, speckles appear at fixed wavevectors, and their intensities grow monotonically. During the dark pattern at time $t = 5.11 \times 10^4$ s, the monochromator was reset. After the monochromator reset, many speckles appear and disappear.

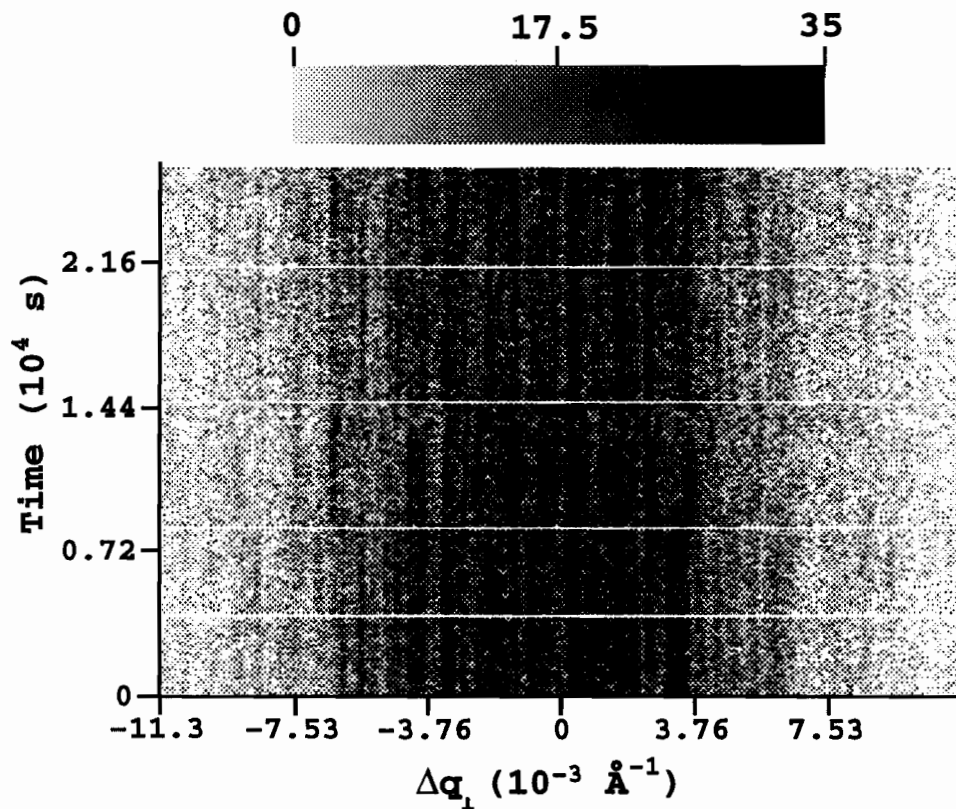


Figure 5.14: Time evolution of a single row with $\Delta 2\theta_{\parallel} = 0$ for run 22. The grey scale displays the normalized data in counts/2min at 200 mA. Most speckles are present over 2.6×10^4 s. Some instability is present near $t = 1.1 \times 10^4$ s. Many speckles change or move around this time. The monochromator was readjusted near $t = 2.16 \times 10^4$ s to reproduce similar conditions as run 21. The effect of the adjustment appears less pronounced than in run 21. Most speckles remain unchanged.

beam stability, since the domain motion is frozen at room temperature. Most of the speckles remain present over seven hours. Some instability occurs near $t = 1.1 \times 10^4$ s. During this time, the sample temperature fluctuated by 2.1°C over 2300s. This temperature change is caused by temperature fluctuations in the laboratory cooling water, which was used to cool the oven. A change of 2.1°C expands the Cu sample post in a direction perpendicular to the scattering plane by $2.2 \mu\text{m}$, which is about 30 % of the pinhole diameter used¹. Thus, this instability could be caused by the effect of this temperature fluctuation on both the oven and on the beamline components. The monochromator was reset at $t = 2.16 \times 10^4$ s. The effect of the monochromator tweak on the speckle pattern appears less pronounced than in run 21. In run 21, we tweaked the monochromator in order to regain some incident intensity because the ratio of beam monitor to synchrotron ring current was dropping rapidly. There was no such drift in run 22.

Fig. 5.15 shows a time series of a row of the CCD with $\Delta 2\theta_{\parallel} = 0$ for run 24. Speckles appear as early as $t = 1.44 \times 10^4$ s and some are still present after 7.1×10^4 s, or 16 hours. An instability occurs around $t = 4.1 \times 10^4$ s and lasts until $t = 4.8 \times 10^4$ s. It correlates with fluctuations of the fit center along $2\theta_{\perp}$ shown in Fig. 5.12. These fluctuations move the fit center by approximately ± 7 pixels, or approximately $\pm 150 \mu\text{rad}$. This instability is caused by instabilities in the beamline, since these time fluctuations are also seen in a beam position monitor. Since the pinhole diameter is twice as large as in run 21, the incident intensity is larger and the relative time fluctuations on time scales of tens of minutes are smaller than in run 21². The spatial fluctuations are reduced because of the smaller contrast observed (see Table 5.1). These two effects result in a smoother image than Fig. 5.13 or Fig. 5.14. Note that we tweaked the monochromator several times during this run, but no effects are noticeable on the time series. It appears that for the data collected at X25, the

¹The Cu sample holder was 6.5 cm high. Using an expansion coefficient of $16.5 \times 10^{-6}/\text{K}$, and the quoted temperature change, one finds a motion of $2.2 \mu\text{m}$.

²A careful analysis comparing the measured variance for a small number of subsequent scans $N \approx 10$ with the calculated variance expected from counting statistics calculated using the calibration curve found in Fig. 3.6 revealed that the short time fluctuations on the order of 25 min are due to Poisson noise and some incident beam fluctuations.

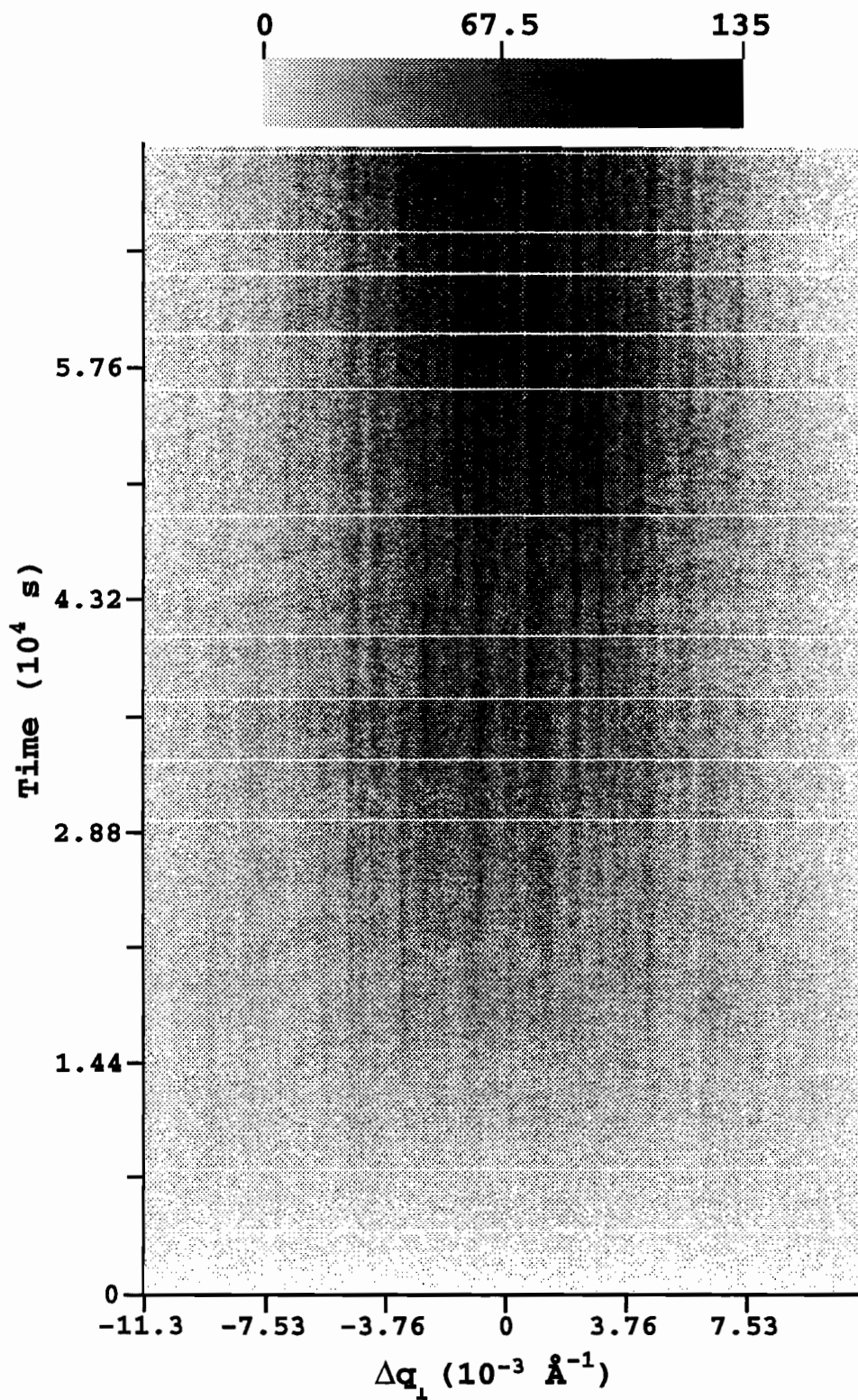


Figure 5.15: A time series of run 24, with $\Delta 2\theta_{\parallel} = 0$ lasting for nearly 20 hours. A linear grey scale from 0 to 135 counts/60s scaled to a maximum synchrotron ring current of 200 mA is used to display the data.

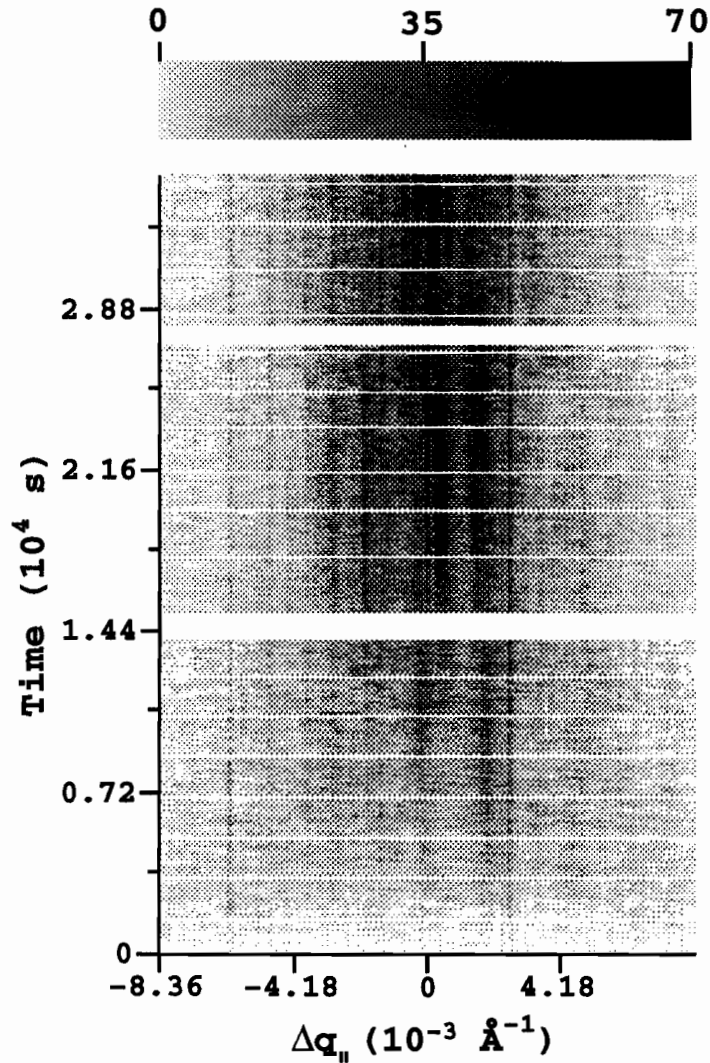


Figure 5.16: A time series of run 113. A single row of the CCD oriented for $\Delta 2\theta_{\perp} = 0$, along $2\theta_{\parallel}$ is shown. Gaps in the data occur during two synchrotron ring fills. Note that the \vec{q} axis orientation of this figure is perpendicular to the previous time series shown.

speckle pattern is almost always unchanged after a monochromator reset.

Fig. 5.16 shows a time series of $S(\vec{q}, t)$ for run 113, along $\vec{q} = (q_{\parallel}, q_{\perp} = 0)$. Speckles appear as early as thirty minutes after the quench, and some of them are still present at $t = 3.4 \times 10^4$ s. The shortest fluctuation time observed in Fig. 5.16 is approximately two hours. There may be signs of faster dynamics on this data set, when compared to the data from runs 21 and 24.

To investigate in more detail the time fluctuations of $S(\vec{q}, t)$, the time dependence of the signal in several pixels is shown next for representative data sets. Fig. 5.17

shows $S(\vec{q}, t)$ vs t for twenty five pixels well separated from each other in Fig. 5.13. The error bars were calculated¹ from the calibration curve in Fig. 3.6, and scaled appropriately to take into account the decay of the synchrotron ring current. The solid line is the fitted intensity $S_f(\vec{q}, t)$ for the given pixels calculated from Eq. 5.11. This measurement is very different from a measurement performed with *incoherent X-rays*, where one expects the fluctuations of the data around the fit to be only due to counting statistics. The time fluctuations of the structure factor with respect to the fit are clearly above the fluctuations due to counting statistics. Note that the signal in each pixel has a *unique* random dynamics. This is what one expects in an IFS experiment. For some pixels, the structure factor remains always above or below the fit. For many pixels, the structure factor crosses $S_f(\vec{q}, t)$, from values lower than S_f , to values higher than S_f at a later time. Fluctuation times range from several thousands of seconds to tens of thousands of seconds. The jump in $S(\vec{q}, t)$ near $t = 5 \times 10^4$ s is due to the monochromator reset. These data are representative of the time fluctuations of $S(\vec{q}, t)$ measured after a quench.

The data in run 22 were taken after run 21 to test the stability of the experiment by scattering from a sample with frozen domain dynamics. The time dependences of twenty five independent pixels in Fig. 5.14 are shown in Fig. 5.18. Apart from a random offset due to the finite contrast, the structure factor fluctuates significantly from the fit. The time fluctuations near 1.1×10^4 s are caused by the instability discussed before. Because of the presence of these time fluctuations when the coarsening dynamics is frozen, the beamline X25 did not have the time stability required at the time of the experiment² to clearly separate intrinsic time fluctuations of $S(\vec{q}, t)$ due to the coarsening dynamics of Cu_3Au , from those caused by beamline instabilities.

¹Given a , the ratio of the monitor count to the monitor count measured for a ring current of 200 mA, the error on the structure factor $S(\vec{q}, t) = av^*(\vec{q}, t)$ is $\sigma_S = \sqrt{\sigma_d^2 + a^2 1.63v^*}$, where σ_d^2 is a dark electronic contribution to the variance measured in a region of the CCD masked by lead, and v^* is the linearized CCD signal. Here σ_S is the standard deviation of $S(\vec{q}, t)$, calculated by a sum of the variances from electronic noise and Poisson noise.

²Since then, much work has been done at X25 to understand the long time stability of beamline X25 [50]. The instabilities seem to be caused by changes in the power loading of the monochromator due to the decay of the synchrotron ring current. Feedback techniques are under consideration to improve the long term stability at X25 [50].

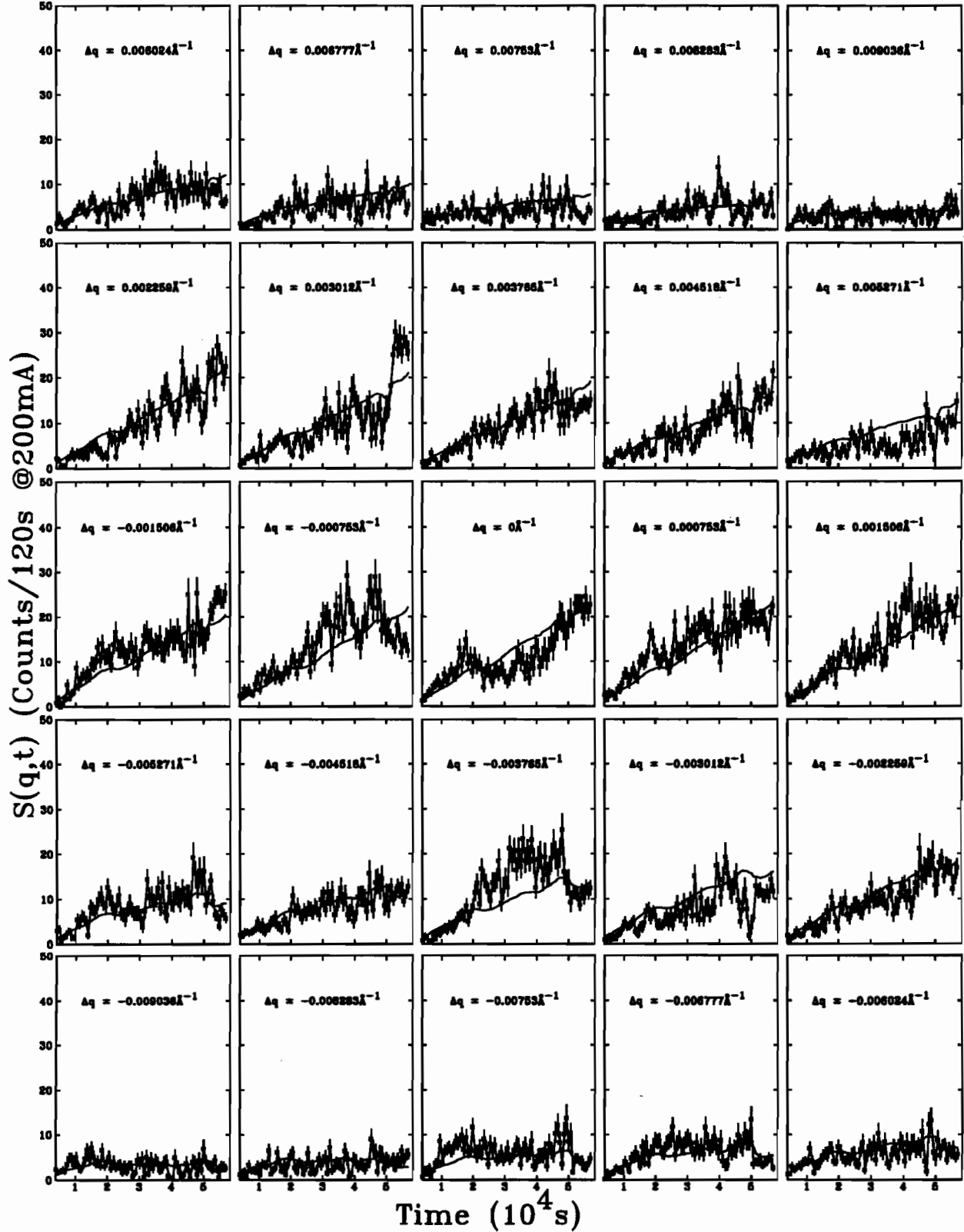


Figure 5.17: Slices of Fig. 5.13 along the time axis for run 21, with $dq_{\parallel} = 0$. Twenty five different pixels are shown, starting from $dq_{\perp} = -9.04 \times 10^{-3} \text{ \AA}^{-1}$ at the lower left corner, to $dq_{\perp} = 9.04 \times 10^{-3} \text{ \AA}^{-1}$ on the top right corner, each separated by $7.53 \times 10^{-4} \text{ \AA}^{-1}$. The solid line is the fitted structure factor for a given pixel. To improve the statistics, the signal was averaged in time by five scans, and in space by summing the signal from two neighboring pixels along $2\theta_{\perp}$. Each pixel behaves differently. Often, the data go from being smaller than the fit to being above it.

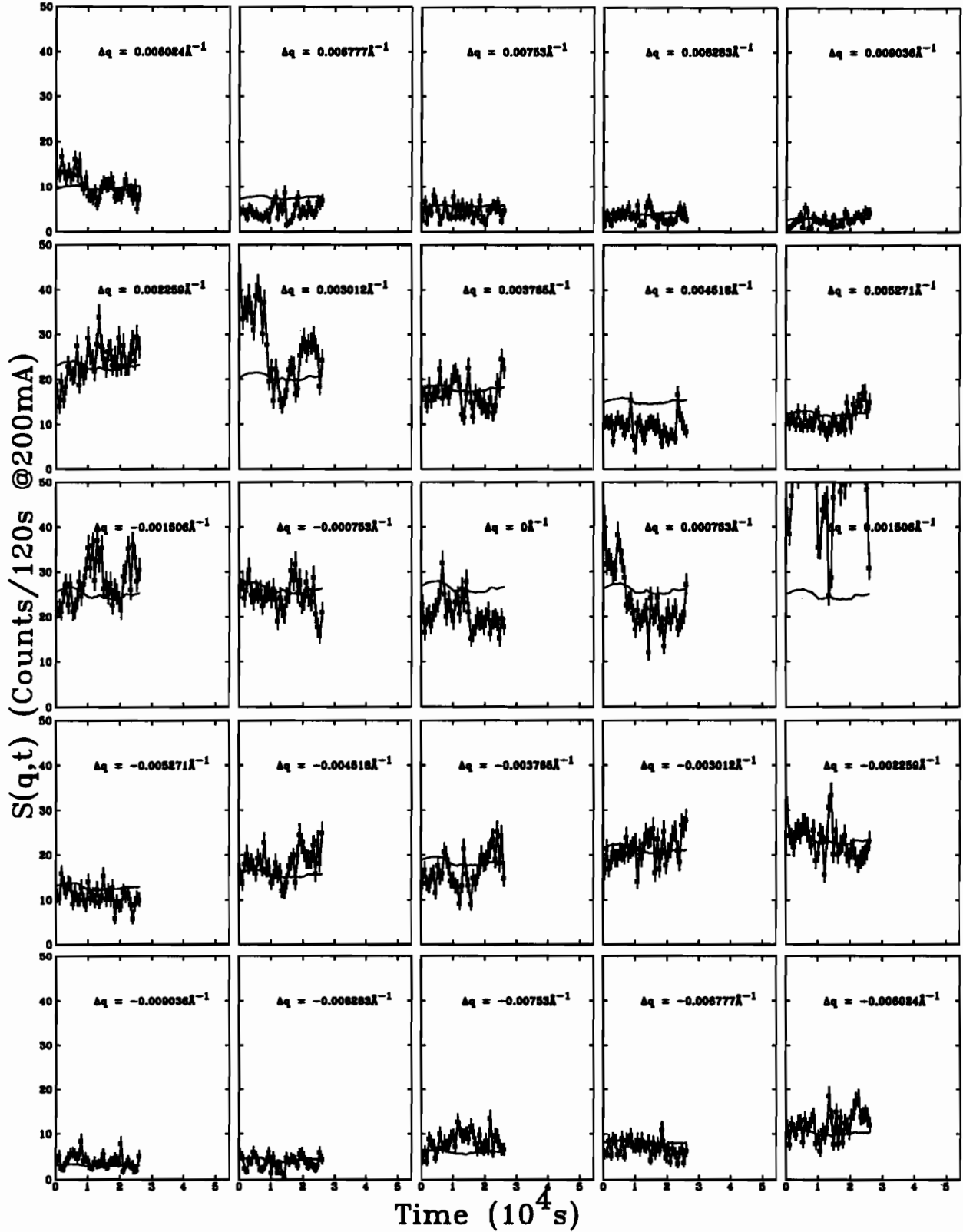


Figure 5.18: Slices along the time axis of Fig. 5.14 in run22, for $dq_{\parallel} = 0$. Twenty five different pixels are shown, starting from $dq_{\perp} = -9.04 \times 10^{-3} \text{ \AA}^{-1}$ at the lower left corner, to $dq_{\perp} = 9.04 \times 10^{-3} \text{ \AA}^{-1}$ on the top right corner, each separated by $7.53 \times 10^{-4} \text{ \AA}^{-1}$. The solid line is the fitted structure factor for a given pixel. To improve the statistics, the signal was averaged in time by five scans, and in space by summing the signal from two neighboring pixels along $2\theta_{\perp}$. Due to some instabilities, the structure factor also fluctuates significantly from the fit.

To conclude this section, we found that the measured spatial contrast for Cu_3Au (100) is temperature independent for the temperatures measured in these experiments. This shows that the speckle pattern is caused by antiphase domains, since the change in thermal diffuse scattering does not affect the contrast.

In all the experiments reported here (see Fig. 5.13–5.16), the dominant speckles appear shortly after the quench at *fixed* \vec{q} , and the intensity of the speckles grows monotonically in time. This is an important aspect of IFS in binary alloys out of thermodynamic equilibrium. After a quench and for a given set of initial conditions, scattering maxima appear at fixed, but random wavevectors. Different fixed wavevectors would be chosen by the system in another quench.

In the coarsening regime, the overall peak intensity of the speckle pattern grows with time, and the peak sharpens as the domains grow. A scaling function estimated by Gaussian least-squares fits of the whole speckle pattern describes well the sharpening of the structure factor. As expected, the widths along $2\theta_{\perp}$ and $2\theta_{\parallel}$ are scaling approximately as $t^{-\frac{1}{2}}$.

Recall that from scaling arguments, the long time behavior of the structure factor $S(\vec{q}, t) \propto R(t)^d f(\vec{q}R(t))$, where f is a scaling function, $R(t) \propto t^{\frac{1}{2}}$ is the average domain size, and $d = 3$ is the dimension of the system. An important feature of the measured speckle pattern is that it *cannot* be rescaled with such a scaling function since the speckles are fixed in reciprocal space, and any scaling function f would move individual speckles towards the center of the Cu_3Au (100) peak. Thus, the presence of speckle explicitly breaks simple scaling of the structure factor which is ubiquitous in phase transitions.

Although this appears surprising, one should recall a few important points about XIFS and scaling. The observation of speckle is a *finite size effect*. Two independent lengths scales are present here: the average domain size and the scattering volume. Strong scattering is observed in the experiment when the average domain size is a small fraction of the sample size. This strong scattering is measured at low wavevectors $\Delta q < 1/R_D$, which corresponds to the large domains. The slow dynamics of large

domains explains why the individual speckles for small wavevectors change slowly in time. Furthermore, scaling in first order phase transitions implies an *ensemble average* over independent quenches or initial conditions. Here, the structure factor is calculated from a single quench! The ensemble average removes the speckles in the structure factor. These facts explain why these observations were never noted before. Note that although the speckle pattern does not follow simple scaling, the average scattering does scale as shown with the Gaussian fits. The power of XIFS is in the measurement of subtle changes of the speckle pattern. We believe that subtle time correlations of the domain structure can be obtained from a single quench on a sample size of a few μm . Much work remains to be done in this direction.

The time fluctuations of the structure factor with respect to a least-squares fit representing the sharpening of the domain distribution are clearly above counting statistics. Unfortunately as seen in Fig. 5.18, the long term stability of the experiment was not sufficient to establish whether these observed fluctuations are intrinsic to the coarsening dynamics or not. The main conclusion of this work is that the amplitude of the time fluctuations of the intensity are small, and that their time scales are very long. As shown in Fig. 2.13 and is well known from light scattering, the amplitude of the fluctuations in thermal equilibrium equals the size of the signal. If such fluctuations would have been present in this non-equilibrium experiment, they would have been easy to measure with the count rates observed.

5.2.1 Numerical Simulations of model A

The behavior described above agrees with the numerical simulation of model A. Fig. 5.19 and 5.20 show the results of a numerical simulation for three different times after a quench at $t = 0$. The parameters of the simulation were the same used in the equilibrium simulation in Eq. 2.29 with $M = -r = w = \kappa = 1.0$, with a Gaussian noise strength $2k_B T M = 0.1$ (see Eq. 2.27). The time interval between two iterations of the simulation was $dt = 0.05$, and the spatial increment $dx = 1$. The system was quenched with a random initial configuration generated with white noise ranging from -0.05 to 0.05 corresponding to the high temperature state. The images on the left

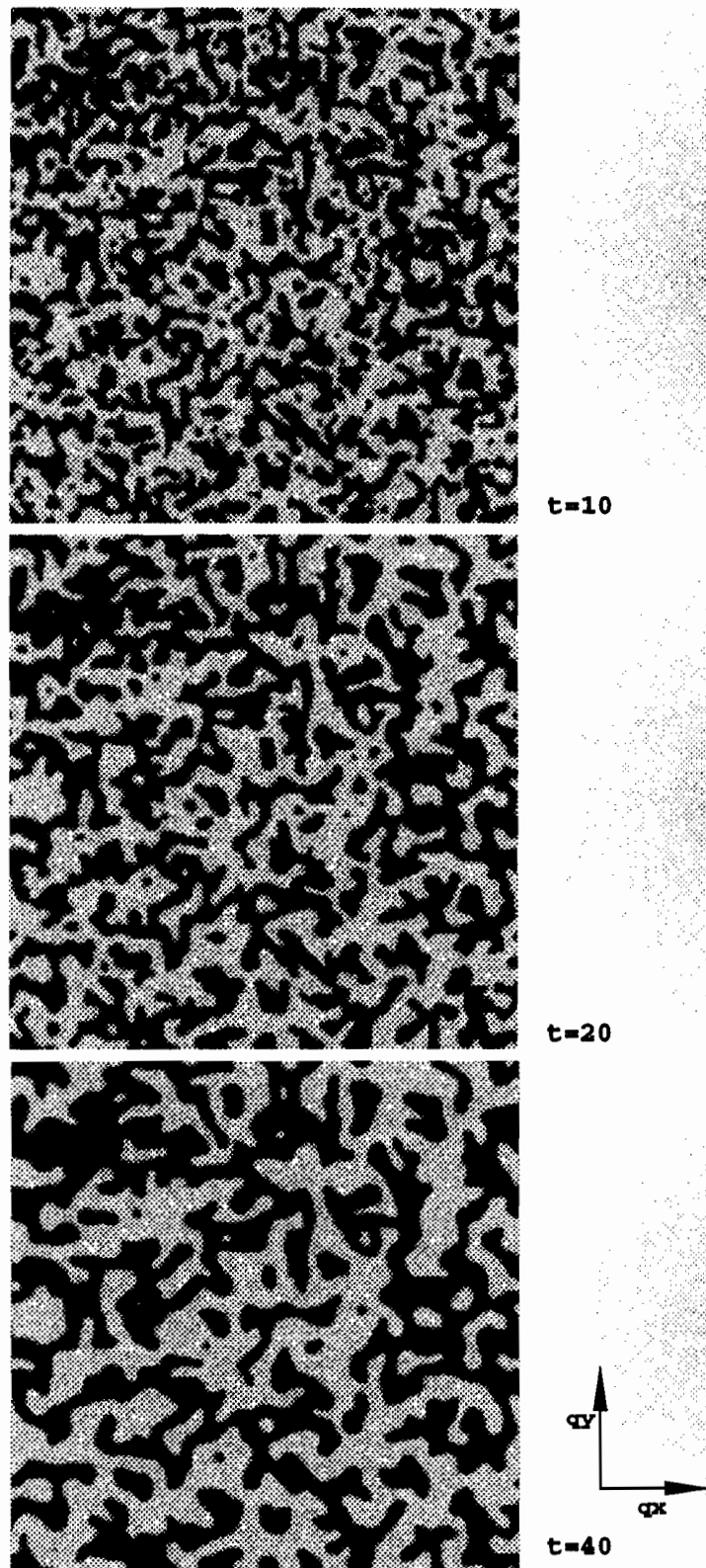


Figure 5.19: The order parameter (left) $\psi(\vec{r}, t)$ and the structure factor $S(\vec{q}, t)$ (right) for three different times t after the quench. A linear grey scale was used to display the order parameter from $\psi = -1.2$ (white) to 1.2 (black), and from 0 to 0.003 for the structure factor. The order parameter spatial dependence is shown for a system of 512×512 . The central 128×128 elements of the structure factor are shown. The central pixel in these images corresponds to $\vec{q} = 0$. Speckle is caused by the coherent diffraction from the random domains shown. As the domains grow, the structure factor sharpens and its intensity increases.

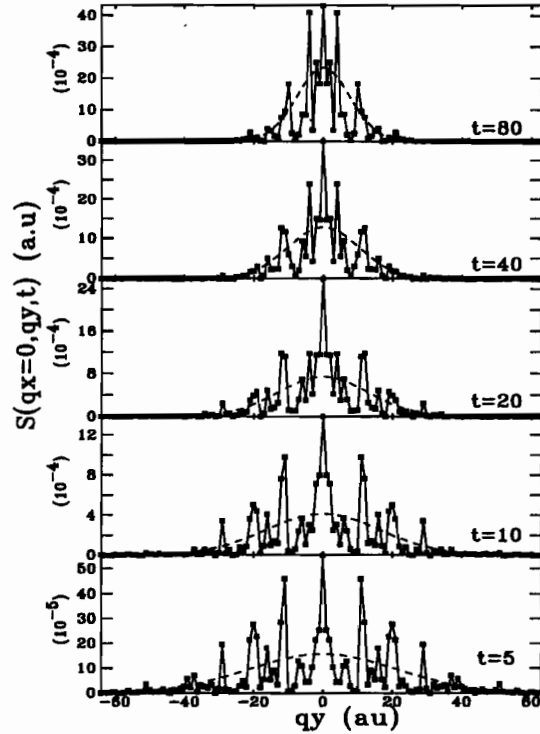


Figure 5.20: Slices of $S(\vec{q}, t)$ for model A, for times $t = 5, 10, 20, 40, 80$ after the quench. The solid line is used as a guide to the eyes. The structure factor grows by a factor 8 and the peak sharpens. Most speckles remain fixed in \vec{q} , and their intensities fluctuate slowly. The dashed lines are fits described in the text.

in Fig. 5.19 show the time dependence of the order parameter for a simulation size of 512×512 . In the coarsening regime for model A, it is well known that a simultaneous rescaling of length and time by factors of two and four respectively yields comparable domain structures [60]. In Fig. 5.19, for example, by rescaling one quarter of the 512×512 system at time $t = 10$ by a factor two, one would find that the domain structure of the rescaled system appears similar to the non-rescaled system at a later time $t = 40$.

On the right of these images, the structure factor calculated from Eq. 2.10 is shown with a linear grey scale. Fig. 5.20 shows slices of $S(\vec{q}, t)$ with $\vec{q} = (0, q_y)$ and time $t = 5, 10, 20, 40, 80$. As observed in our experiments, speckle is present in the simulation. In order to reduce the speckle in the structure factor, most theoretical work performs either averages on an ensemble of independent initial conditions, or on several wavevectors with identical magnitude $|\vec{q}| = q$. By performing these averages, one loses much of the information on the fluctuations of the order parameter during

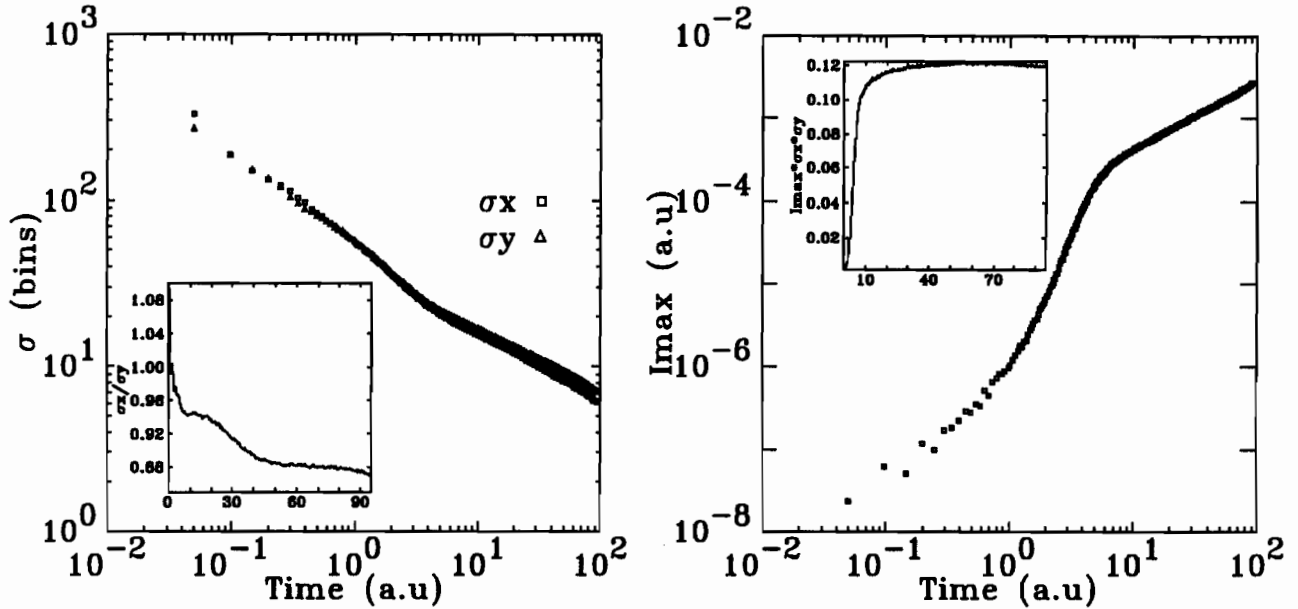


Figure 5.21: (Left) The time dependence of the two perpendicular fitted widths σ_x and σ_y . The widths are measured in units of the wavevector resolution $\Delta q = 2\pi/L$, where L is the system size. The inset shows the time dependence of the ratio of σ_x/σ_y . The ratio of the fitted widths is below unity at late times indicating a slight difference between the exponents of the widths. (Right) The peak intensity, I_{max} . After a transient, the system crosses over to scaling after time $t \approx 7$. The inset shows the integrated intensity for the fit $I_{max}\sigma_x\sigma_y$ vs time.

the quench.

The domain coarsening in Fig. 5.19 and 5.20 is seen by a sharpening of $S(\vec{q}, t)$ and an increase in the intensity of the peak. The dashed line in Fig. 5.20 is a least-squares fit of the structure factor to a Gaussian defined in Eq. 5.11. In analogy with the CCD data, this fit is used to define a local average for the fluctuations.

Fig. 5.21 shows the time dependence of the fit parameters. The center of the fit was fixed at $\vec{q} = 0$. A plot of the fitted widths σ_x and σ_y is shown. A fit of each width to a power law in the coarsening regime, i.e. from $t = 7$ to 95, gives $\sigma_x \propto t^{-0.41}$ and $\sigma_y \propto t^{-0.40}$. This difference is real since the ratio of σ_x/σ_y decreases as t increases (See the inset). It is amusing to note that these power law exponents are similar to the data.

A plot of the fitted peak intensity, I_{max} , is also shown as a function of time after the quench. The peak intensity, after a transient which last until $t \approx 7$, becomes a power law. This is consistent with the coarsening of domains. A fit of the peak intensity from $t = 7$ to 95 gives $I_{max} \propto t^{0.86}$. The inset shows the calculated integrated intensity

of the fitted Gaussian $I_{max}\sigma_x\sigma_y$. It is time dependent in the nucleation regime, but slows down after $t \approx 7$. In the coarsening regime, it is slightly time dependent since the sum of the exponents from the widths and peak intensity does not add up to zero.

The magnitudes of these exponents are significantly lower than the expected exponents for model A. For model A, one expects $\sigma_x \propto t^{-\frac{1}{2}}$, $\sigma_x/\sigma_y = 1$, and $I_{max} \propto t^{\frac{d}{2}}$, with $d = 2$ dimensions. The expected results are obtained from an ensemble average of many quenches with different initial conditions, and the structure factor is circularly averaged. It is well known that one must average several quenches to get adequate statistics for these parameters. These differences in the magnitude of the exponents, and the anisotropy of $S(\vec{q}, t)$ are consistent with the poor sampling of phase space for a single quench.

Fig. 5.22 shows a time series of $S(\vec{q}, t)$ for $\vec{q} = (qx, 0)$. The time dependence is shown here for 100 wavevectors using the grey scale shown. From the definition of the structure factor, the figure is symmetric with respect to the origin $\vec{q} = 0$. Recall that the fluctuation time in equilibrium for model A is $\tau_c = \frac{1}{M(2q^2 - 4r)}$, which ranges from $\tau_c = 0.25$ to 0.08 as shown in Fig. 2.11c. The fluctuations on Fig. 5.22 are several orders of magnitude slower than the equilibrium fluctuations of the short range order. At low momentum transfer, the fluctuation times are much larger than the simulation time shown, but for large qx , fluctuations are observable on time scales ranging from ≈ 2 to 60, which is still much larger than τ_c . This is shown in more detail in Fig. 5.23, where slices for several qx are shown. The solid line is the simulation data, and the dashed line is the Gaussian fit, with parameters shown in Fig. 5.21. The sudden rise and decay of the fit for a given qx gives us a characteristic time for the coarsening dynamics at a given qx . For low qx from 0 to 20, the simulation time is comparable to the coarsening time, but for higher qx , some intensity fluctuations are seen above the fit with time scales of the order of $\Delta t = 20$.

The time correlation of these fluctuations has not been investigated further. More work remains to be done in this area. We urge theorists to investigate the intensity fluctuations of the structure factor without performing *spherical averages*, because it

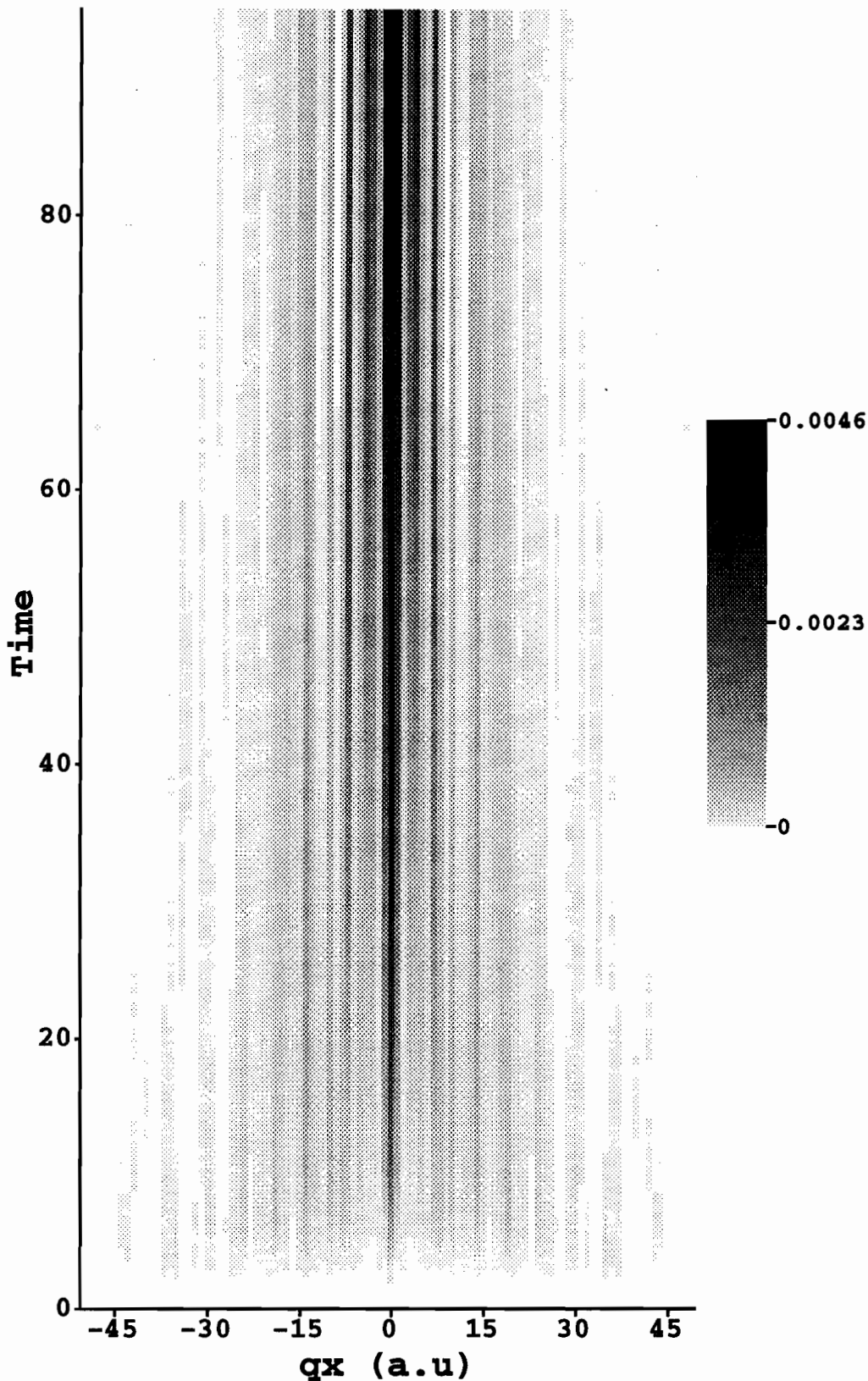


Figure 5.22: A time series of $S(\vec{q}, t)$, for $\vec{q} = (qx, 0)$ after a quench at $t = 0$. The component qx is measured in units of $\Delta q = 2\pi/L$, where $L = 512$ is the system size in Fig. 5.19. Note that a speckle at $qx = 7$ has a wavelength $\lambda = 2\pi/qx = L/7$. The fluctuations of the structure factor for model A are much slower than the equilibrium fluctuations discussed in Chapter 2 because the dominant speckle correspond to the Fourier modes associated with the long wavelength domain structure in the sample. As seen in Fig. 5.19, this overall domain structure changes very slowly.

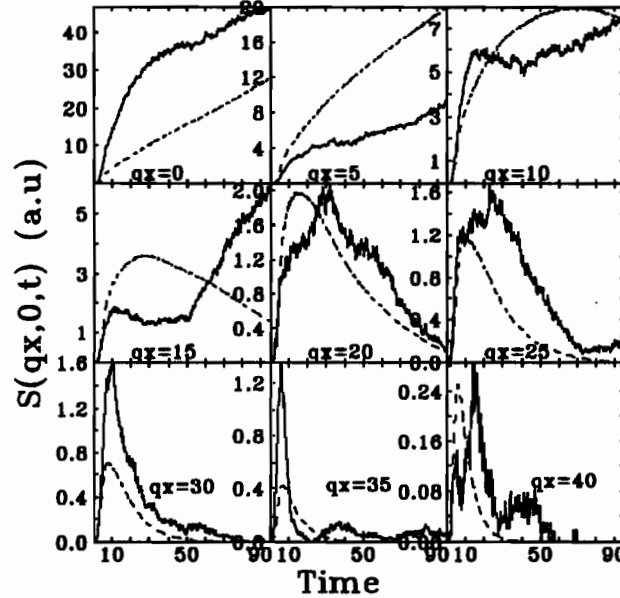


Figure 5.23: $S(\vec{q}, t)$ vs t for several qx ranging from 0 to 40. The solid line is the simulation data, and the dashed line is a least-squares fit to a Gaussian discussed in the text.

is now possible to measure these fluctuations with coherent X-rays! This time correlation function should provide additional information on the dynamics of ordering.

In conclusion, we find that the numerical simulation of model A is in good qualitative agreement with the measurements in Cu_3Au . The simulation shows that the dominant speckles are fixed in reciprocal space and their intensities slowly increase in time. Fig. 5.22 shows that the long-lived speckles correspond to long wavelength fluctuations associated with the domain structure. It is clear from Fig. 5.19 that a large fraction of the overall domain structure correlates with itself at later times. This explains why the time fluctuations of the speckle pattern from Cu_3Au (100) and for the theoretical simulation are much longer than the typical fluctuation times found in equilibrium.

Note that it is not essential to use a detailed model of Cu_3Au with a more physical Hamiltonian to understand the data. The small system size for the simulation (Here 512×512) will always be much smaller than the experimental system (4.4×10^{12} unit cells!)¹. The essential features are present in the simple model shown here. This

¹The illuminated volume in our experiment is $D(\frac{D}{\sin \theta_B})(\mu \sin \theta_B) = D^2 \mu$, where $D = 7.5 \mu\text{m}$ is the collimating pinhole diameter, $\mu = 4.2 \mu\text{m}$ is the absorption length of X-rays in Cu_3Au at 7 keV. Dividing this volume by the lattice cell volume $(3.711 \text{ \AA})^3$, we find that our illuminated volume

slow dynamics of speckle after a quench from the disordered equilibrium phase to the ordered phase will be present in any model and depends only on the presence of an extended domain structure which persists over an extended time. For example, we expect the dynamics of speckle in model B to be even slower than model A, because of the smaller growth exponent in model B ($1/3$ instead of $1/2$).

More theoretical work remains to be done to make some prediction on the time correlation function. Due to long time instabilities in the beamline at X25, these experiments should be performed again at the new third generation sources like ESRF and APS in order to study the detailed time dependence of the speckle pattern. Recently, we have demonstrated that the Troika beamline at ESRF is sufficiently stable to perform IFS on Fe_3Al near its critical point [19]. Because of the small contrast of the time fluctuations of $S(\vec{q}, t)$ in these systems, the increase in coherent flux should allow one to measure more subtle fluctuations of the structure factor.

corresponds to 4.4×10^{12} unit cells.

CONCLUSIONS

We have shown that one can produce a beam of coherent X-rays by *spatially filtering* an incoherent beam of *monochromatic* X-rays to dimensions smaller than its transverse coherence lengths using small pinholes with diameters of a few μm . A second generation synchrotron radiation source like beamline X-25 at NSLS provides a sufficient coherent flux to perform *coherent* X-rays scattering experiments.

When a coherent beam is scattered from a disordered sample, a graininess in the structure factor is observed, called speckle. The speckle pattern is sensitive to the exact arrangement of the atoms in the illuminated volume. If the state of disorder of the sample changes with time, the speckle pattern will fluctuate in time. An analysis of the time correlations of the scattered light at a given wavevector allows a direct measurement of the dynamics of the system, in and out of thermodynamic equilibrium.

This thesis is the first study of the ordering kinetics of first order phase transitions in a classical binary alloy with a *non-conserved order* parameter, using *coherent hard X-rays*. One of the important contributions of this thesis has been to develop techniques to measure the speckle patterns produced by coherent X-ray scattered from a binary alloy with a two-dimensional CCD detector, as well as techniques to analyze these patterns.

In Chapter 3, the development of techniques based on statistical estimators like the mean, variance and spatial correlation function has been essential in our understanding of the noise, quantum efficiency, and spatial resolution of the CCD. The use of spatial correlation functions to measure the resolution of the CCD is an original

contribution [37]. The spatial autocorrelation function of the signal generated by a spatially uniform incident beam is broadened by the spread of the detected electrons to several nearest neighbor pixels. By assuming an identical response for each detected photon, the resolution function can be extracted from the measured correlation function. The spatial extent of the resolution function reduces the spatial or temporal variance of the signal when compared to the variance due to Poisson noise. This effect must be accounted for in the calculation of the quantum efficiency. These techniques can be applied to any typical one and two-dimensional position-sensitive detectors, and can also characterize non-linear detectors.

Section A.2 also contains central and original derivations, which have been used throughout the thesis to calculate error bars of various functions of the estimated average, $\langle V \rangle$, and variance, S_V^2 , of the signal V . We have shown that by combining standard error analysis with the variances and covariance of $\langle V \rangle$ and S_V^2 , one can approximate the standard deviation of several functions of the estimated mean and variance $f(\langle V \rangle, S_V^2)$. We derived, for example, the error on the contrast $\sqrt{S_V^2 / \langle V \rangle^2}$ and on the ratio $S_V^2 / \langle V \rangle$. This ratio of variance over mean is an important quantity which can be used to calibrate a detector, or to determine whether or not the observed time fluctuations of the signal are above the fluctuations expected from counting statistics.

The development of the detector characterization techniques was based on spatial correlation functions introduced to measure the speckle size of Cu_3Au speckle patterns. Using spatial correlation functions, it was shown that this detector has a sufficient spatial resolution to measure speckle patterns of Cu_3Au (100). The speckle pattern properties were studied by changing the horizontal transverse coherence length, and the illuminated sample area. The speckle size was measured by the width at small displacements of the spatial crosscorrelation function of two subsequent scans of the CCD. The speckle width is reduced when the illuminated sample area is increased, until the speckle size is comparable to the resolution of the CCD. Then the widths become resolution limited. Increasing the horizontal coherence length reduced

the speckle size horizontally. Because the CCD resolution is anisotropic and broader than one pixel, and because the beam is partially coherent, the effect of different optical conditions requires subtle analysis. A theoretical model based on the autocorrelation function of the Fraunhofer diffraction pattern of the pinhole convolved with the detector resolution is in good agreement with the observations. Some difference is seen between the model and the data for the smallest pinhole $D = 3.5 \mu\text{m}$. Perhaps this indicates that the illuminated sample area is larger than the pinhole area, since the sample is placed at the limit of the near-field diffraction of the pinhole. Note that these effects should be easier to resolve if the angular resolution of the detector is improved, whether by choosing a detector with finer spatial resolution, or placing the detector further away.

The contrast of the speckle pattern was also measured by subtracting the expected Poisson noise contribution from the spatial fluctuations. The contrast is reduced as expected when the input beam diameter increases, and when the upstream source size is increased. The measured contrast is smaller than expected. We discussed some of the possible causes for this difference earlier.

These measurements of the contrast and speckle size are major contributions of this thesis. It is the first *detailed quantitative* analysis of X-ray speckle. The measurements on static speckle from Cu_3Au agree well with the well known properties of speckle. Because the CCD detector can measure thousands of independent speckles simultaneously, the contrast and autocorrelation functions can be measured quite accurately. The calculation algorithm are also simple to implement. This work has some applications in microscopy, like atomic force and electron microscopy. For example, it is straightforward to measure the average domain size in an image with the autocorrelation function.

We measured the time fluctuations of the structure factor for the (100) superlattice reflection of Cu_3Au after a quench from the disordered phase to the ordered phase. Soon after the quench, speckles appear at fixed positions in reciprocal space. Their intensities grow like the average scattering from antiphase domains. The overall

sharpening of the structure factor and the increase in peak intensity can be measured by least-squares fits of the whole speckle pattern. The widths and peak intensity of the Gaussian fits follow power laws, as expected from the coarsening of domains.

The approach we took to study the time fluctuations is to look at the time fluctuations with respect to a time-dependent growing average, provided by two-dimensional fits. By studying the statistics of the relative fluctuations with respect to the fit, one can test whether these fluctuations are above counting statistics or not. The interested reader will find some of our experience gained in analyzing the time fluctuations in equilibrium and out of equilibrium compiled in section A.4. For the X-25 data, the time fluctuations on a time scale of one half hour are within the expected fluctuations due to Poisson noise of the detected photons and incident intensity fluctuations, thus the speckles are constant over this time scale within fluctuations due to counting statistics. Intrinsic fluctuations with larger time scales due to the coarsening dynamics cannot easily be separated from fluctuations caused by beamline instabilities at present.

The amplitude of the time fluctuations of the data is small, and consistent with theory. As opposed to an IFS experiment performed in thermal equilibrium (see Fig. 2.13), the relative amplitude of these fluctuations is much smaller than 100 % and the fluctuation times are long. This makes quantitative analysis particularly difficult because of the limited count rate and the beamline instabilities. If the amplitude of these fluctuations had been larger, the time fluctuations would have been more easily measured. We believe that the small size of the fluctuations is an important property of the speckle patterns generated by the non-equilibrium growth which produced the domain structure.

This observation is qualitatively consistent with a numerical simulation of model A. After the quench, speckles appear at fixed \vec{q} , and their dynamics are slow. This observation is consistent with the simple picture that the speckle pattern is dominated by the scattering from large domains which slowly grow at the expense of small domains. This dynamics makes the small domains disappear, leaving the macroscopic

domain arrangement over the sample size changing slowly with time (see Fig. 5.19). Fourier modes representing the domain structure changes only slowly because the macroscopic domain structure correlates with itself for long times.

The last conclusion of this thesis is that individual speckles remain *fixed* in reciprocal space after the quench. This observation violates simple minded scaling in the experimental data and the numerical simulation. Although the speckle pattern does not scale, the overall scattering sharpens as expected for scaling. This persistence of speckle seems to be a general property of the structure factor of non-equilibrium growth measured with coherent light, for both conserved and non-conserved order parameters. These experiments started out as a way to test some of the ideas of Grant and Roland [36]. There is good reason to believe that these types of measurements will lead to a deeper understanding of this type of phenomena, but much work still need to be done. This XIFS work has also generated a lot of interest in the visible IFS community, and many experiments are underway to study non-equilibrium phenomena.

To measure the time fluctuations in more detail, longer experiments with higher incident coherent flux are planned in the future. A factor of 100-1000 in intensity is accessible by using the new undulator facilities such as the ESRF or the APS. This increase in flux would allow to reduce the error bars in Fig. 5.17 by a factor of more than ten, and enables smaller changes of the structure factor to be measured. As demonstrated recently [19], these beamlines are also more stable in terms of beam intensity and position. Ideally, one should also look for systems with faster intrinsic dynamics than Cu_3Au , and samples which scatter isotropically¹.

Improvements in detecting scheme are also achievable. For example, very low noise two dimensional gas detectors with nearly unit quantum efficiency (a factor 4 larger than the detector used in this experiment) are under development at the ESRF, and should be operational within the next year. These detectors allow measurements

¹For example, although an Fe_3Al sample scatters less than a Cu_3Au one due to smaller scattering contrast, it scatters isotropically in $2\Theta_{\parallel}$ and $2\Theta_{\perp}$, making it possible to ensemble average correlation functions with the same $|\vec{q}|$. This should improve the statistics of the correlation function and allow for the measurement of the wavevector dependence of the correlation function [89].

of the time arrival of each photon, and have very low dark noise. Similarly, CCD performance can be improved by using low noise detectors, with a CCD chip having a larger depletion layer. A larger depletion layer is found in EEV chips, for example [90], and this increases the quantum efficiency for hard X-rays. At 7 keV, the EEV chip has a quantum efficiency of 50 %, which is a factor two better than the chip used here. Another approach with CCDs is to couple the array optically with an X-ray sensitive phosphor which greatly enhances the quantum efficiency but reduces the CCD resolution. By placing such a detector a few meters away, the resolution should be sufficient to resolve speckle patterns. A completely different approach with CCDs should be used when the count rates are low. For low count rates, it is possible to detect single photons events. This removes most of the electronic noise in the data, and in principle allow subpixel spatial resolution!

These measurements are some of the first results using this newly developed scattering technique. As a feasibility experiment, our measurements on Cu_3Au were a success! We demonstrated that the experiment can be performed, and pointed out some of the major problems encountered on second generation synchrotron sources. These results have important applications in the design of the next generation of beamlines optimized to produce coherent X-rays. These measurements are also exciting because they give new insights on the dynamics of phase transitions not available before. Beside our IFS results, the simple example of coherent X-ray scattering from an isolated edge dislocation was given in Chapter 2. This proposed experiment is already feasible with existing sources.

Coherent X-ray scattering will be a powerful technique at the newly commissioned third generation synchrotron sources, and many group are developing strong scientific programs in this field. Because the coherence lengths of synchrotron radiation are on the order of the microstructure of many materials, coherent X-rays will be a tool of choice to investigate disorder in these materials.

APPENDICES

A.1 Some useful probability distributions

A Poisson distribution is discrete. The probability of measuring n events is

$$P(n) = \frac{\mu^n e^{-\mu}}{n!}. \quad (\text{A.1})$$

The mean and the variance are μ . Higher central moments are $\overline{(x - \mu)^3} = \mu$, and $\overline{(x - \mu)^4} = 3\mu^2 + \mu$.

A Gaussian distribution is continuous, with probability density

$$\rho(x) = \frac{1}{\sqrt{2\pi}\sigma} \exp\left[-\frac{(x - \mu)^2}{2\sigma^2}\right]. \quad (\text{A.2})$$

The mean is μ and the variance is σ^2 . Higher moments are $\overline{(x - \mu)^3} = 0$ and $\overline{(x - \mu)^4} = 3\sigma^4$.

A chi-square random variable is given by

$$\chi^2 = \sum_{i=1}^M (y_i - \bar{y}_i)^2. \quad (\text{A.3})$$

It is the sum of the squares of M Gaussian random variable y_i , with average \bar{y}_i and standard deviation σ . The probability density of this random variable is

$$\rho(\chi^2) = (\sqrt{2}\sigma)^{-M} (\chi^2)^{M/2-1} \exp\left(-\frac{\chi^2}{2\sigma^2}\right) / \Gamma(M/2). \quad (\text{A.4})$$

The average is $M\sigma^2$ and the variance $2M\sigma^4$, with a contrast $\sqrt{2/M}$.

The chi-square distribution is the probability distribution followed by speckle statistics for $M=2$. For speckle, the scattered intensity $I = \text{Re}\{E\}^2 + \text{Im}\{E\}^2$, i.e. the sum of the squares of the real and imaginary part of the Gaussian scattered electric field E . Here the electric field is linearly polarized. For $M = 2$, Eq. A.4 is an exponential with average $\bar{I} = 2\sigma^2$ and standard deviation $\sigma_I = 2\sigma^2$. The fluctuations of the scattered intensity are as large as the mean!

When a detector averages several speckles because its area integrates over many speckles, Eq. A.4 is also the distribution which *approximately* describes the scattered intensity I . The probability density of the scattered intensity is

$$p(I) = \left(\frac{N_s}{\bar{I}}\right)^{N_s} I^{N_s-1} \exp\left(-\frac{N_s I}{\bar{I}}\right) / \Gamma(N_s), \quad (\text{A.5})$$

where N_s is the number of independent speckle in the detector area, or the ratio of the detector area over the speckle area introduced in Eq. 5.3, and \bar{I} is the average intensity. This is known as the gamma probability density [39]. For $N_s = 1$, it reduces to the exponential distribution we derived earlier in Eq. 2.34. Its average is \bar{I} and its variance is $\frac{\bar{I}^2}{N_s}$, so that the contrast $\frac{\sigma}{\bar{I}} = \frac{1}{\sqrt{N_s}}$.

A.2 Error analysis

One often wants to evaluate the uncertainty in the estimated average $\langle x \rangle$ and variance S^2 of a random variable X , with theoretical mean μ and variance σ^2 . Assuming that the probability density $\rho(x)$ of the random variable X is stationary, the true mean and variance of $\rho(x)$ are defined by

$$\bar{x} = \int_{-\infty}^{\infty} x\rho(x)dx = \mu, \text{ and} \quad (\text{A.6})$$

$$\overline{(x - \mu)^2} = \int_{-\infty}^{\infty} (x - \mu)^2\rho(x)dx = \sigma^2, \quad (\text{A.7})$$

with $\int_{-\infty}^{\infty} \rho(x)dx = 1$. The discussion below is limited to distributions with finite μ and σ^2 . The statistical estimators of the mean $\langle x \rangle$ and variance S^2 are defined by

$$\langle x \rangle = \frac{1}{N} \sum_{i=1}^N x_i, \text{ and} \quad (\text{A.8})$$

$$S^2 = \frac{1}{N-1} \sum_{i=1}^N (x_i - \langle x \rangle)^2, \quad (\text{A.9})$$

where x_i is a measured outcome of the random variable X , chosen from the same probability distribution $\rho(x)$. The estimators $\langle x \rangle$ and S^2 are unbiased estimators of the mean and variance and on average are equal to μ and σ^2 . The uncertainties in these statistical estimators depend on the number of random events observed, N . For small N , the fluctuations in the measured or estimated value are comparable to the expected value. Therefore, its dependence on N must be well characterized.

The uncertainty on the mean is well known and goes as $\sqrt{\sigma^2/N}$ [64]. For a Gaussian distribution, the uncertainty on the variance is $\sqrt{2/(N-1)\sigma^2}$ [64]. In section A.2.1, we derive a general relation for the uncertainty of the estimated variance, and apply it to the Poisson distribution. In error propagation analysis, one may want to evaluate the uncertainty in a function of the mean and variance $f(\langle x \rangle, S^2)$ as required in section 3.0.3. To evaluate the error in f , one uses the uncertainty in $\langle x \rangle$ and S^2 , and needs to know the covariance between $\langle x \rangle$ and S^2 . A general expression for this covariance is derived in section A.2.2, and a derivation for Eq. (3.7) is shown in section A.2.3 and A.2.4.

A.2.1 Uncertainty in the measured mean and variance

It is important to note that $\langle x \rangle$ and S^2 are themselves random variables since they are functions of several random variables. A useful estimator of the uncertainty of these new random variables is their standard deviations $\sigma_{\langle x \rangle}$ and σ_{S^2} defined in Ref. [64] by

$$\sigma_{\langle x \rangle}^2 = \overline{\langle x \rangle^2} - \langle \overline{\langle x \rangle} \rangle^2, \text{ and} \quad (\text{A.10})$$

$$\sigma_{S^2}^2 = \overline{S^4} - \overline{S^2}^2, \quad (\text{A.11})$$

where the horizontal line refers to an average over the joint probability distribution of the random variable $\langle x \rangle$, a function of N random variables x_i , i.e. $\overline{\langle x \rangle} \equiv \int \langle x \rangle(x_1, \dots, x_N) \rho(x_1, \dots, x_N) dx_1 \dots dx_N$. $\sigma_{\langle x \rangle}$ and σ_{S^2} are the standard deviations of the probability densities of $\langle x \rangle$ and S^2 . The N dependence in Eq. (A.10-A.11) is not explicitly written in order to keep the notation simple. From Eq. (A.8), recalling that $\bar{x}_i = \mu$, it is easy to show that $\overline{\langle x \rangle} = \mu$. In order to simplify the algebra below, we introduce a new variable $y_i = x_i - \mu$, so that $\bar{y}_i = 0$ and $\overline{y_i^2} = \sigma^2$. One can now rewrite Eq. (A.10), using Eq. (A.8) and square it to get

$$\sigma_{\langle x \rangle}^2 = \frac{1}{N^2} \sum_{i,j=1}^N \overline{y_i y_j}. \quad (\text{A.12})$$

Assuming that each y_i is independent, i.e.

$$\overline{y_i y_j} = \delta_{ij} \sigma^2, \quad (\text{A.13})$$

where δ_{ij} is a Kronecker delta, and replacing Eq. (A.13) in Eq. (A.12), one gets

$$\sigma_{\langle x \rangle}^2 = \frac{\sigma^2}{N}, \quad (\text{A.14})$$

which is a well known result valid for any N , and any probability distribution with finite mean and variance, given that no correlation exists between the x_i 's. This result states that the probability density of $\langle x \rangle$, $\rho(\langle x \rangle)$, is narrower than $\rho(x)$ by a factor $\sqrt{\frac{1}{N}}$.

In Eq. (A.11), the $\overline{S^2}$ term can be evaluated by substituting x_i by y_i and replacing Eq. (A.8) into Eq. (A.9). Then, one finds

$$S^2 = \frac{1}{N-1} \left(\sum_{i=1}^N y_i^2 - \frac{1}{N} \sum_{i,j=1}^N y_i y_j \right). \quad (\text{A.15})$$

Taking averages on both sides of Eq. (A.15), and evaluating the sums with Eq. (A.13), one finds $\overline{S^2} = \sigma^2$, as stated before. The $N-1$ denominator comes from the fact that there is one less degree of freedom used to evaluate the mean. Taking the square of Eq. (A.15), and taking averages on the right and left hand side of the equation, one finds

$$\overline{S^4} = \frac{1}{(N-1)^2} \left(\sum_{i,j=1}^N \overline{y_i^2 y_j^2} - \frac{2}{N} \sum_{i,j,k=1}^N \overline{y_i^2 y_j y_k} + \frac{1}{N^2} \sum_{i,j,k,l=1}^N \overline{y_i y_j y_k y_l} \right). \quad (\text{A.16})$$

Evaluating the averages recalling that $\overline{y_i} = 0$ and $\overline{y_i y_j} = \delta_{ij} \sigma^2$, one finds

$$\overline{y_i^2 y_j^2} = \begin{cases} \overline{y^4}, & \text{for } i = j, \quad N \text{ terms,} \\ \sigma^4, & \text{for } i \neq j, \quad N(N-1) \text{ terms,} \end{cases} \quad (\text{A.17})$$

$$\overline{y_i^2 y_j y_k} = \begin{cases} \overline{y^4}, & \text{for } i = j = k, \quad N \text{ terms,} \\ \sigma^4, & \text{for } i \neq j = k, \quad N(N-1) \text{ terms,} \\ 0, & \text{otherwise,} \end{cases} \quad (\text{A.18})$$

$$\overline{y_i y_j y_k y_l} = \begin{cases} \overline{y^4}, & \text{for } i = j = k = l, \quad N \text{ terms,} \\ \sigma^4, & \text{for } i = j \neq k = l, \quad 3N(N-1) \text{ terms,} \\ 0, & \text{otherwise.} \end{cases} \quad (\text{A.19})$$

Here, the n th order central moment is defined by $\overline{y^n} \equiv \int y^n \rho(y) dy$. Using Eq. (A.17-A.19) to evaluate the sums in Eq. (A.16), and replacing Eq. (A.16) into Eq. (A.11), one finds

$$\sigma_{S^2}^2 = \frac{\overline{y^4}(N-1) + \sigma^4(3-N)}{N(N-1)}. \quad (\text{A.20})$$

This result depends on the fourth order central moment of the distribution, $\overline{y^4}$, and the standard deviation, σ . For a Gaussian distribution, (see section A.1) $\overline{y^4} = 3\sigma^4$ and Eq. (A.20) gives as expected $\sigma_{S^2}^2 = \frac{2}{N-1}\sigma^4$. For a Poisson distribution on the other hand, $\overline{y^4} = 3\mu^2 + \mu$ which yields

$$\sigma_{S^2}^2 = \frac{2}{N-1}\mu^2 + \frac{\mu}{N}. \quad (\text{A.21})$$

Note that for $\mu < 1$, the second term is an important correction and a Gaussian approximation would underestimate the error on the variance. For large means, Eq. (A.21) becomes identical to the error for a Gaussian with variance equal to the mean, as expected since the Poisson distribution crosses over to such a Gaussian for large means. Finally, note that since in general $\rho(S^2)$ is not Gaussian, one cannot easily quantify the confidence limits of S^2 , but can nevertheless calculate its variance.

A.2.2 Correlation of the sample mean and variance

One might think that there is no correlation between the estimator of the mean $\langle x \rangle$ and the estimator of the variance S^2 . The independence of the estimated mean and variance is discussed in several statistical books for Gaussian distributions [73, 64]. The measure of correlation between the measured mean and variance, the covariance, is defined as

$$\begin{aligned} \text{cov}(\langle x \rangle, S^2) &= \overline{(\langle x \rangle - \mu)(S^2 - \sigma^2)} = \overline{\langle y \rangle S^2} \\ &= \frac{1}{N(N-1)} \left(\sum_{i,j=1}^N \overline{y_i y_j^2} - \frac{1}{N} \sum_{i,j,k=1}^N \overline{y_i y_j y_k} \right), \end{aligned} \quad (\text{A.22})$$

since $\overline{\langle y \rangle \sigma^2} = 0$. Evaluating the averages as in Eq. (A.17-A.19), one finds

$$\overline{y_i y_j y_k} = \begin{cases} \overline{y^3}, & \text{for } i = j = k, \quad N \text{ terms,} \\ 0, & \text{otherwise.} \end{cases} \quad (\text{A.23})$$

The same results holds for $\overline{y_i y_j^2}$. Replacing those in Eq. (A.22) and simplifying, one gets

$$\text{cov}(\langle x \rangle, S^2) = \frac{\overline{y^3}}{N}, \quad (\text{A.24})$$

where $\overline{y^3}$ is the 3rd order central moment of the distribution. Thus, the covariance depends on N , and on how symmetric with respect to the mean is the probability distributed. The estimated mean and variance are independent only as N goes to infinity, or if $\overline{y^3} = 0$. For a Gaussian distribution, the covariance is zero because odd powers of the central moments are zero. For a Poisson distribution, $\overline{y^3} = \mu$ (see Appendix A.1) and

$$\text{cov}(\langle x \rangle, S^2) = \frac{\mu}{N}. \quad (\text{A.25})$$

A.2.3 Evaluation of the error on a function of S^2 and $\langle x \rangle$

From standard error propagation analysis [73], one can readily calculate the uncertainty of a function $f(\langle x \rangle, S^2) = \frac{S^2}{\langle x \rangle}$. It is given by

$$\frac{\sigma_f^2}{f^2} \approx \frac{\sigma_{S^2}^2}{S^2} + \frac{\sigma_{\langle x \rangle}^2}{\langle x \rangle^2} - \frac{2\text{cov}(S^2, \langle x \rangle)}{\langle x \rangle S^2}, \quad (\text{A.26})$$

where the terms on the right hand side have been calculated above. The approximate sign comes from the fact that σ_f is derived from a first order Taylor expansion of f around its average. Replacing the uncertainties and covariance derived previously for a Poisson distributed random variable X in Eq. (A.14), (A.21), (A.25), one finds

$$\frac{\sigma_f^2}{f^2} \approx \frac{2}{N-1}. \quad (\text{A.27})$$

The result is independent of the mean μ . By averaging N independent measurements, one can measure f accurately. On the other hand, if the signal is Gaussian distributed, the covariance term in Eq. (A.26) would be zero, and one gets $\frac{\sigma_f^2}{f^2} \approx \frac{2}{N-1} + \frac{\sigma^2}{\mu^2 N}$. Depending on the mean and variance of the distribution, the second term may be important.

A.2.4 Including electronic noise for an X-ray detector

For an X-ray detector, Eq. (A.27) is not sufficient to estimate the errors on k , defined in Eq. (3.5), because for weak signals, the electronic noise will contribute significantly to σ_k . V_e , the dark electronic noise, increases the relative error on the time averaged mean $\langle V \rangle_t$ and variance $S_{t,V}^2$ when the contribution from the detected photons approaches zero. To find σ_k , the standard deviation of k , we can simply replace in Eq. (A.26) $\langle x \rangle$ by $\langle V \rangle_t$, and S^2 by $S_{t,V}^2 - \sigma_{V_e}^2$, where $\sigma_{V_e}^2$ is the theoretical variance of the electronic noise probability distribution. Then the first term of Eq. (A.26) can be rewritten as

$$\frac{\sigma_{S_{t,V}^2 - \sigma_{V_e}^2}^2}{(S_{t,V}^2 - \sigma_{V_e}^2)^2} = \frac{\sigma_{k^2 S_{n_d}^2} + \sigma_{S_{V_e}^2}^2}{(S_{t,V}^2 - \sigma_{V_e}^2)^2}$$

$$= \frac{2}{N-1} + \frac{1}{Nn_d} + \frac{2\sigma_{V_e}^4}{(N-1)(S_{t,V}^2 - \sigma_{V_e}^2)^2}. \quad (\text{A.28})$$

To obtain this relationship, we used the equation $\sigma_{S_{t,V}^2 - \sigma_{V_e}^2}^2 = \sigma_{S_{t,V}^2}^2$ and Eq. (3.3), and assuming that V_e follows Gaussian statistics. The first two terms are the detected photon contributions which are included in Eq. (A.27), and the last term is due to an error on the evaluation of the dark variance. Next, we can evaluate the second term of Eq. (A.26) using Eq. (3.3),

$$\begin{aligned} \frac{\sigma_{\langle V \rangle_t}^2}{\langle V \rangle_t^2} &= \frac{k^2 \sigma_{n_d}^2 + \sigma_{V_e}^2}{N \langle V \rangle_t^2} + \frac{\sigma_{V_e}^2}{N_d \langle V \rangle_t^2} \\ &= \frac{1}{Nn_d} + \frac{\sigma_{V_e}^2}{\langle V \rangle_t^2} \left(\frac{1}{N} + \frac{1}{N_d} \right), \end{aligned} \quad (\text{A.29})$$

where n_d and $\langle V \rangle_t$ are the hypothesized means of the number of detected photons and of the detector signal, while $\sigma_{n_d}^2$ and $\sigma_{V_e}^2$ are the theoretical variances of n_d and of the dark electronic noise. The first term in this equation comes from the statistics of the detected photons and is already included in Eq. (A.27). The second term explains the increased uncertainty in k for small signals due to the electronic noise. The third term is due to the statistical error in the measurement of the dark pattern subtracted from V , where N_d scans are averaged without X-rays. To minimize the error, one should choose $N_d = N$. Finally, the last term in Eq. (A.26) is unchanged from the Poisson case because the dark signal and the detected photon signal are not correlated. Collecting terms, we find

$$\frac{\sigma_k^2}{k^2} \approx \frac{2}{N-1} \left(1 + \frac{\sigma_{V_e}^4}{(S_{t,V}^2 - \sigma_{V_e}^2)^2} \right) + \frac{\sigma_{V_e}^2}{\langle V \rangle_t^2} \left(\frac{1}{N} + \frac{1}{N_d} \right). \quad (\text{A.30})$$

It is therefore easier to measure k when $\langle V \rangle_t^2$ and $S_{t,V}^2$ are much larger than $\sigma_{V_e}^2$. To evaluate σ_k for a given experiment, one would replace $\sigma_{V_e}^2$, $S_{t,V}^2$ and $\langle V \rangle_t$ by the experimentally measured values S_{t,V_e}^2 , $S_{t,V}^2$ and $\langle V \rangle_t$.

Note that the error analysis approach developed above can be extended to other problems, such as the evaluation of the error on the measured contrast in optics if the signal is not Gaussian distributed. It is also useful to estimate the errors in our coherent X-ray experiments.

For example, the error on the measured contrast for the time-averaged scattered intensity in section 2.6.2 is derived with the same technique. In section 2.6.2, the contrast is defined by

$$Ct = \frac{\sqrt{S^2}}{\langle x \rangle}. \quad (\text{A.31})$$

Neglecting the term for the correlation between the estimated mean and variance, it is easy to show that the error on the contrast

$$\frac{\sigma_{Ct}}{Ct} \approx \sqrt{\frac{\sigma_{S^2}^2}{4S^2} + \frac{\sigma_{\langle x \rangle}^2}{\langle x \rangle^2}} \approx \sqrt{\frac{1}{2(N-1)} + \frac{Ct^2}{N}}. \quad (\text{A.32})$$

Here, the error on the estimated variance σ_{S^2} was approximated by the error for Gaussian statistics.

A.3 Derivation of the autocorrelation function for a Gaussian

If one assumes that the structure factor is a smoothly varying function of \vec{q} , one can understand quantitatively the \vec{q} dependence of the crosscorrelation function (see Eq. 5.5) which is caused by the presence of antiphase domains.

Let us study the autocorrelation function by choosing $dt = 0$ in Eq. 5.5. For the two dimensional Gaussian function defined in Eq. 5.11, one can show that its spatial autocorrelation function calculated by a two dimensional integral over a rectangle in reciprocal space with edges $L_{\perp} \times L_{\parallel}$ is

$$\begin{aligned} \langle v^*(\vec{q}, t) v^*(\vec{q} + \vec{d}\vec{q}, t) \rangle_{\vec{q}} &= \frac{\pi \sigma_{\perp} \sigma_{\parallel} I_{max}^2}{4 L_{\perp} L_{\parallel}} \exp\left(\frac{-dq_{\perp}^2}{4\sigma_{\perp}^2}\right) \exp\left(\frac{-dq_{\parallel}^2}{4\sigma_{\parallel}^2}\right) \left[\operatorname{erf}\left(\frac{L_{\parallel} + dq_{\parallel}}{2\sigma_{\parallel}}\right) + \operatorname{erf}\left(\frac{L_{\parallel} - dq_{\parallel}}{2\sigma_{\parallel}}\right) \right] \\ &\times \left[\operatorname{erf}\left(\frac{L_{\perp} + dq_{\perp}}{2\sigma_{\perp}}\right) + \operatorname{erf}\left(\frac{L_{\perp} - dq_{\perp}}{2\sigma_{\perp}}\right) \right], \end{aligned} \quad (\text{A.33})$$

where I_{max} is the peak intensity, and σ_{\perp} is the Gaussian width along $2\theta_{\perp}$. The error functions are present because of the finite size of L_{\perp} and L_{\parallel} . For a small displacement with $|dq_{\perp}| \ll L_{\perp}$ and $|dq_{\parallel}| \ll L_{\parallel}$, the autocorrelation in Eq. A.33 is also approximately a two dimensional Gaussian with width along $2\theta_{\perp}$ equal to $\sqrt{2}\sigma_{\perp}$.

In Fig. 5.5–5.7, the autocorrelation is normalized by the square of the spatial average. For a two dimensional Gaussian, the spatial average of the linearized signal is

$$\langle v^* \rangle_{\vec{q}} = \frac{2\pi \sigma_{\perp} \sigma_{\parallel} I_{max}}{L_{\perp} L_{\parallel}} \operatorname{erf}\left(\frac{L_{\perp}}{2\sqrt{2}\sigma_{\perp}}\right) \operatorname{erf}\left(\frac{L_{\parallel}}{2\sqrt{2}\sigma_{\parallel}}\right). \quad (\text{A.34})$$

Thus the normalized autocorrelation function for small displacement $|dq_{\perp}| \ll L_{\perp}$ and $|dq_{\parallel}| \ll L_{\parallel}$ is approximately

$$\frac{\langle v^*(\vec{q}, t) v^*(\vec{q} + \vec{d}\vec{q}, t) \rangle_{\vec{q}}}{\langle v^* \rangle_{\vec{q}}^2} \propto \frac{L_{\perp} L_{\parallel}}{16\pi \sigma_{\perp} \sigma_{\parallel}} \exp\left(\frac{-dq_{\perp}^2}{4\sigma_{\perp}^2}\right) \exp\left(\frac{-dq_{\parallel}^2}{4\sigma_{\parallel}^2}\right). \quad (\text{A.35})$$

Note that the maximum of the normalized autocorrelation is inversely proportional to the product of the widths $\sigma_{\perp} \sigma_{\parallel}$.

A.4 Tools for time fluctuations analysis

Here are some of the tools that might be useful for simple analysis of time fluctuations for XIFS in systems in thermal equilibrium and out of equilibrium. In equilibrium, to make sure that the time fluctuations are larger than the fluctuations due to counting statistics and electronic noise, one can measure the fluctuations of the structure factor

with respect to its long time average, and compare these fluctuations to those caused by Poisson noise. We define the ratio of these two quantities as

$$R(\vec{q}, t) = \frac{S_{t,S}^2(\vec{q})}{\langle S(\vec{q}, t) \rangle_t}, \quad (\text{A.36})$$

where $S_{t,S}^2$ is the variance and $\langle S(\vec{q}, t) \rangle_t$ the time average of the structure factor $S(\vec{q}, t)$ measured from a sequence of N measurements. In deriving Eq. A.36, the detector is assumed to have unit quantum efficiency and a spatial resolution much smaller than the speckle size. With such a detector, the expected variance from Poisson noise is simply equal to the time average $\langle S(\vec{q}, t) \rangle_t$. Note that we have already derived this equation earlier since this is simply the equation for k in Eq. 3.5 for a detector without electronic noise! If the fluctuations are only caused by Poisson noise, $R = 1$, and its error bars are given by Eq. A.27. A ratio greater than unity implies that the fluctuations are significantly larger than fluctuations due to counting statistics.

In an intensity fluctuation spectroscopy experiment, one wants to know what is the standard deviation of the structure factor corrected for trivial fluctuations due to counting statistics¹. This standard deviation of $S(\vec{q}, t)$, $\sigma_{t,S}$ is simply

$$\sigma_{t,S}(\vec{q}) = \sqrt{(R(\vec{q}) - 1) \langle S(\vec{q}, t) \rangle_t}. \quad (\text{A.37})$$

Therefore, the relative fluctuation of the structure factor is simply the ratio of Eq. A.37 over the time average $\langle S(\vec{q}, t) \rangle_t$ equal to

$$\frac{\sigma_{t,S}(\vec{q})}{\langle S(\vec{q}, t) \rangle_t} = \sqrt{\frac{R(\vec{q}) - 1}{\langle S(\vec{q}, t) \rangle_t}}. \quad (\text{A.38})$$

If the ratio $R(\vec{q}) = 1.1$ and the time average of the structure factor is 10 counts, then the relative rms fluctuation of the signal with respect to its time average is $\sqrt{0.1/10} = 10\%$.

Out of equilibrium, since the time average of $S(\vec{q}, t)$ changes in time, Eq. A.36 must be modified to take this into account. We have found it useful to measure the fluctuations of the speckle pattern with respect to two dimensional least-squares fit of the whole speckle pattern. A natural variable to study fluctuations is

$$\eta(\vec{q}, t) = \frac{S(\vec{q}, t)}{S_f(\vec{q}, t)} - 1. \quad (\text{A.39})$$

Here η is the relative difference between the structure factor $S(\vec{q}, t)$, and the fit $S_f(\vec{q}, t)$. Assuming for simplicity that the detector is ideal, the expected standard deviation of η is

$$\sigma_\eta = \frac{\sqrt{S(\vec{q}, t)}}{S_f(\vec{q}, t)}. \quad (\text{A.40})$$

¹An excellent introduction on the subject can be found in Chapter 9 of Goodman [39].

To calculate whether the fluctuations of $\eta(\vec{q}, t)$ are above its expected error bars, we define the ratio

$$R_\eta(\vec{q}) = \frac{S_{t,\eta}^2(\vec{q})}{\langle \sigma_\eta^2(\vec{q}, t) \rangle_t}. \quad (\text{A.41})$$

Here the variance of η , $S_{t,\eta}^2$, and the time average of the calculated variance σ_η^2 , $\langle \sigma_\eta^2(\vec{q}, t) \rangle_t$, can be calculated from N subsequent measurements. The ratio $R_\eta(\vec{q}, t)$ is a two dimensional array in our measurements.

BIBLIOGRAPHY

- [1] Edited by D. Cornuéjols. Annual report 1993. Technical report, European Synchrotron Radiation Facility, BP 220 F-38043 Grenoble France, 1994.
- [2] Editors: S.L. Hulbert and N.M. Lazarz. Annual report 1992. Technical Report BNL 52317, National Synchrotron Light Source, 1993.
- [3] K. Exner. *Sitzungsber. Kaiserl. Akad. Wiss. (Wien)*, 76:522, 1877.
- [4] K. Exner. *Wiedemanns. Ann. Phys.*, 9:239, 1880.
- [5] M. von Laue. *Sitzungsber. Akad. Wiss. (Berlin)*, 44:1144, 1914.
- [6] J.C. Dainty, editor. *Laser Speckle and Related Phenomena*. Springer-Verlag, Berlin, New York, second edition, 1984.
- [7] R. Alben, G.S. Cargill, III, and J. Wenzel. Anisotropy of structural models for amorphous materials. *Phys. Rev. B*, 13:835–842, 1972.
- [8] A. Garg and D. Levine. Speckle in the diffraction patterns of Hendricks-Teller and icosahedral glass models. *Phys. Rev. Lett.*, 60:2160, 1988.
- [9] Anupam Garg and Dov Levine. Garg and Levine reply. *Phys. Rev. Lett.*, 63:1439, 1989.
- [10] K.F. Ludwig, Jr. Comment on “Speckle in the diffraction patterns of Hendricks-Teller and icosahedral glass models”. *Phys. Rev. Lett.*, 61:1526, 1988.
- [11] X.B. Kan and J.L. Robertson. Comment on “Speckle in the diffraction patterns of Hendricks-Teller and icosahedral glass models”. *Phys. Rev. Lett.*, 63:1438, 1989.
- [12] B. J. Berne and R. Pecora. *Dynamic Light Scattering*. John Wiley & Sons, Inc., New York, 1976.
- [13] B. Chu. *Laser Light Scattering: Basic Principles and Practice*. Academic Press, Boston, Toronto, second edition, 1991.
- [14] S.B. Dierker. X-ray photon correlation spectroscopy at the NSLS. Technical report, National Synchrotron Light Source, Brookhaven National Laboratory, Upton, NY, 11973, 1995. (July Newsletter).
- [15] M. Sutton, S.G.J Mochrie, T. Greytak, S.E. Nagler, L.E. Berman, G.A. Held, and G.B Stephenson. Observation of speckle by diffraction with coherent X-rays. *Nature*, 352:608, 1991.

- [16] Z.H. Cai, B. Lai, W.B. Yun, and I. McNulty. Observation of X-ray speckle by coherent scattering at grazing incidence. *Phys. Rev. Lett.*, 73:82–85, 1994.
- [17] I.K. Robinson, R. Pindak, R.M. Fleming, S.B. Dierker, K. Ploog, G. Grübel, D.L. Abernathy, and J. Als-Nielsen. Observation and explanation of one-dimensional x-ray speckle patterns from synthetic multilayers. *Phys. Rev. B*, 52:9917–9924, 1995.
- [18] R. Pindak, R.M. Fleming, I.K. Robinson, and S.B. Dierker. The effect of the longitudinal coherence length on the crossover from incoherent to coherent diffraction. Annual Report BNL 52317, National Synchrotron Light Source, 1993. p382.
- [19] S. Brauer, G.B. Stephenson, M. Sutton, R. Brüning, E. Dufresne, S.G.J. Mochrie, G. Grübel, J. Als-Nielsen, and D.L. Abernathy. X-ray intensity fluctuation spectroscopy observations of critical dynamics in Fe₃Al. *Phys. Rev. Lett.*, 74:2010–2013, 1995.
- [20] F. Bley, F. Livet, J.C. Leroux, J.P. Simon, D. Abernathy, J. Als-Nielsen, G. Gruebel, G. Vignaud, G. Dolino, J.F. Legrand, D. Camel, N. Menguy, and M. Papoular. High q-resolution x-ray diffraction of ordered fe-al single crystals. *Acta Cryst. A*, 51:746–753, 1995.
- [21] M. Sutton, S.G.J Mochrie, T. Greytak, S.E. Nagler, L.E. Berman, G.A. Held, and G.B Stephenson. Intensity fluctuation spectroscopy using coherent X-ray. Annual Report BNL 52317, National Synchrotron Light Source, 1991. p293.
- [22] S.B. Dierker, R. Pindak, R.M. Fleming, I.K. Robinson, and L. Berman. X-ray photon correlation spectroscopy study of Brownian motion of gold colloids in glycerol. *Phys. Rev. Lett.*, 75:449–452, 1995.
- [23] B. Chu, Q.-C. Ying, F.-J. Yey, A. Patkowski, W. Steffen, and E.W. Fisher. An X-ray photon correlation experiment. *Langmuir*, 11:1419–1421, 1995.
- [24] M.W. Kim, A.J. Schwartz, and W.I Goldberg. Evidence for the influence of hydrodynamics in a phase-separating fluid. *Phys. Rev. Lett.*, 41:657–660, 1978.
- [25] E. Dufresne, R. Brüning, M. Sutton, G.B Stephenson, B.G. Rodricks, C. Thompson, and S.E. Nagler. Intensity fluctuation spectroscopy using coherent X-ray. Annual Report BNL 52317, National Synchrotron Light Source, 1993. p381.
- [26] B.E. Warren. *X-Ray Diffraction*. Dover Publications, Inc., New York, 1990.
- [27] John M. Cowley. *Diffraction Physics*. North-Holland, Amsterdam, 2nd edition, 1981.
- [28] T. Hashimoto, K. Nishimura, and Y. Takeuchi. Dynamics of transitional ordering process in Cu₃Au alloy from disordered state to ordered state. *J. Phys. Soc. Jpn.*, 45:1127–1135, 1978.

- [29] Y. Noda, S. Nishihara, and Y. Yamada. Critical behavior and scaling law in ordering process of the first order phase transition in Cu_3Au alloy. *J. Phys. Soc. Jpn.*, 53:4241–4249, 1984.
- [30] K.F. Ludwig, Jr., G.B. Stephenson, J.L. Jordan-Sweet, J. Mainville, Y.S. Yang, and M. Sutton. Nucleated and continuous ordering in Cu_3Au . *Phys. Rev. Lett.*, 61:1859, 1988.
- [31] R.F. Shannon, Jr., C.R. Harkless, and S.E. Nagler. Effect of extra Cu on ordering kinetics in thin films of Cu_3Au . *Phys. Rev. B*, 38:9327, 1988.
- [32] R.F. Shannon, Jr., S.E. Nagler, C.R. Harkless, and R. M. Nicklow. Time-resolved X-ray scattering study of ordering kinetics in bulk single-crystal Cu_3Au . *Phys. Rev. B*, 46:40–53, 1992.
- [33] S.E. Nagler, R.F. Shannon, Jr., C.R. Harkless, and M.A. Singh. Time-resolved X-ray scattering study of ordering and coarsening in Cu_3Au . *Phys. Rev. Lett.*, 61:718–721, 1988.
- [34] J.D. Gunton, M. San Miguel, and P.S. Sahni. The dynamics of first-order phase transitions. In C. Domb and J.L. Lebowitz, editors, *Phase Transitions and Critical Phenomena*, volume 8, pages 267–467. Academic Press, London, 1983.
- [35] A.J. Bray. Theory of phase ordering kinetics. *Advances in Physics*, 43:357–459, 1994.
- [36] C. Roland and M. Grant. Lack of self-averaging, multiscaling, and $1/f$ noise in the kinetics of domain growth. *Phys. Rev. Lett.*, 63:551–554, 1989.
- [37] E. Dufresne, R. Brüning, M. Sutton, G.B. Stephenson, and B. Rodricks. A statistical technique for characterizing X-ray position-sensitive detectors. *Nucl. Inst. and Meth. A*, 364:380–393, 1995.
- [38] M. Born and E. Wolf. *Principles of Optics*. Pergamon, Oxford, 1970.
- [39] J.W. Goodman. *Statistical Optics*. John Wiley & Sons, Inc., New York, first edition, 1985.
- [40] Giorgio Margaritondo. *Introduction to Synchrotron Radiation*. Oxford University Press, New York, 1988.
- [41] A. G. Michette and C.J. Buckley, editors. *X-Ray Science and technology*. Institute of Physics Publishing, Bristol and Philadelphia, 1993.
- [42] C. Kittel. *Introduction to Solid State Physics*. John Wiley & Sons, New York, sixth edition, 1986.
- [43] D. Vaughan. X-ray data booklet. Technical Information Department, Lawrence Berkeley Laboratory, Berkeley, California 94720, 1986.

- [44] S. Brauer, G.B. Stephenson, and M. Sutton. Perfect crystals in the asymmetric Bragg geometry as optical elements for coherent X-ray beams. *J. Synch. Rad.*, 2:163–173, 1995.
- [45] X-M. Zhu, H. Zabel, I.K. Robinson, E. Vlieg, J.A. Dura, and C.P. Flynn. Surface-induced heterophase fluctuation. *Phys. Rev. Lett.*, 65:2692, 1990.
- [46] H. Dosch, L. Måiländer, H. Reichert, and J. Peisl. Long-range order near the $\text{Cu}_3\text{Au}(001)$ surface by evanescent X-ray scattering. *Phys. Rev. B*, 43:13172–13186, 1991.
- [47] H. Reichert, P.J. Eng, H. Dosch, and I.K. Robinson. Thermodynamics of surface segregation profiles at $\text{Cu}_3\text{Au}(001)$ resolved by X-ray scattering. *Phys. Rev. Lett.*, 74:2006, 1995.
- [48] B.D. Butler and J.B. Cohen. The structure of Cu_3Au above the critical temperature. *J. Appl. Phys.*, 65:2214, 1989.
- [49] P.N. Pusey. Statistical properties of scattered radiation. In H.Z. Cummins and E.R. Pike, editors, *Photon Correlation Spectroscopy and Velocimetry*, page 45. Plenum, New York, 1977.
- [50] L.E. Berman. Preserving the high source brightness with X-ray beam line optics. *Rev. Sci. Instrum.*, 66:2041–2047, 1995.
- [51] G. Grübel, D. Abernathy, G.B. Stephenson, S. Brauer, I. McNulty, S.G.J. Mochrie, B. McClain, A. Sandy, M. Sutton, E. Dufresne, I.K. Robinson, R. Fleming, R. Pindak, and S. Dierker. Intensity fluctuation spectroscopy using coherent X-rays. Technical report, ESRF, March 1995. (ESRF Newsletter).
- [52] S. Brauer, G. B. Stephenson, M. Sutton, S.G.J. Mochrie, R.M. Fleming, R. Pindak, I.K. Robinson, G. Grübel, J. Als-Nielsen, and D.L. Abernathy. Asymmetrically cut crystals as optical elements for highly collimated X-ray beams. *Rev. Sci. Instrum.*, 66:1506–1509, 1995.
- [53] B.L. Henke, E.M. Gullikson, and J.C. Davis. Low-energy X-ray interaction coefficients: Photoabsorption, scattering, and reflection. *Atomic Data and Nuclear Data Tables*, 54(2), 1993.
- [54] Massimo Altarelli. Physics with third generation synchrotron sources. *Phys. Scripta*, T55:9–13, 1994.
- [55] Nuclear Data Center, online database at Brookhaven National Laboratory. Telnet to bnlnd2.dne.bnl.gov, username `nndc`, search the X-ray absorption database.
- [56] J.W. Christian. *The Theory of Transformations in Metals and Alloys Part I. Equilibrium and General Kinetic Theory*. Pergamon Press, New York, 2nd edition, 1975.

- [57] Qun Shen, C.C. Umbach, B. Weselak, and J. M. Blakely. X-ray diffraction from a coherently illuminated Si(001) grating surface. *Phys. Rev. B*, 48:17967, 1993.
- [58] S. Tanaka, C.C. Umbach, Q. Shen, and J. M. Blakely. Atomic diffusion and strain measurement on Si grating structures by X-ray diffraction. In *MRS Spring 95 Proceedings*, 1995.
- [59] P.C. Hohenberg and B.I. Halperin. Theory of dynamic critical phenomena. *Rev. Mod. Phys.*, 49:435, 1977.
- [60] Ken Elder. Langevin simulations of nonequilibrium phenomena. *Computers in Physics*, 7(1):27-33, 1993.
- [61] B. Morin, K.R. Elder, and M. Grant. Theory for quenches from ordered states in nonconserved systems. *Phys. Rev. B*, 47:2487-2492, 1993.
- [62] W. H. Press, S. A. Teukolsky, W. T. Vetterling, and B. P. Flannery. *Numerical Recipes in C*. Cambridge University Press, Cambridge, second edition, 1992.
- [63] R. Srinivasan. *Some Statistical Applications in X-ray Crystallography*. Pergamon Press, Oxford, New York, 1st edition, 1975.
- [64] B.R. Frieden. *Probability, Statistical Optics and Data Testing*. Springer-Verlag, New York, second edition, 1991.
- [65] C. Roland. *Growth and Scaling in First-Order Phase Transitions*. PhD thesis, McGill University, 1989.
- [66] S. Brauer, J.O. Ström-Olsen, M. Sutton, Y.S. Yang, A. Zaluska, G.B. Stephenson, and U. Köster. In situ X-ray studies of rapid crystallization of amorphous NiZr₂. *Phys. Rev. B*, 45:7704, 1992.
- [67] Byungwoo Park, G. Brian Stephenson, Samuel M. Allen, and Karl F. Ludwig, Jr. The development of fluctuations into domains during ordering in Fe₃Al. *Phys. Rev. Lett.*, 68:1742, 1992.
- [68] R. Clarke, W. Dos Passos, W. Lowe, B.G. Rodricks, and C. Brizard. Real-time X-ray studies of strain kinetics in In_xGa_{1-x}As quantum wells structures. *Phys. Rev. Lett.*, 66:317, 1991.
- [69] R.C. Jones. Quantum efficiency of detectors for visible and infrared radiation. *Adv. Electron. Electron Phys.*, 11:87, 1959.
- [70] Steven S. Vogt, Robert G. Tull, and Philip Keaton. Self-scanned photodiode array: High performance operation in high dispersion astronomical spectrophotometry. *Appl. Optics*, 17:574-591, 1978.

- [71] G. B. Stephenson. Early-stage phase separation in amorphous solids: a time resolved SAX study. Technical Report Report 82/05, Stanford Synchrotron Radiation Laboratory, 1982. p140.
- [72] James R. Janesick, Kenneth P. Klaasen, and Tom Elliott. Charge-coupled-device charge-collection efficiency and the photon-transfer technique. *Optical Engineering*, 26:972–980, 1987.
- [73] William R. Leo. *Techniques for Nuclear and Particle Physics Experiments*. Springer-Verlag, New York, 1987.
- [74] Jacques Mainville. *A Time Resolved X-Ray Study of Spinodal Decomposition in Aluminium Zinc*. PhD thesis, McGill University, 1992.
- [75] L.N. Koppel. Direct X-ray response of self-scanning photodiode arrays. *Adv. X-ray Anal*, 19:587, 1976.
- [76] Brian Rodricks and Christine Brizard. Programmable CCD imaging system for synchrotron radiation studies. *Nucl. Inst. and Meth. A*, 311:613–619, 1992.
- [77] Christine Brizard and Brian Rodricks. Programmable CCD imaging system for synchrotron radiation studies. *Rev. Sci. Instrum.*, 63:802–805, 1992.
- [78] Brian Rodricks, Roy Clarke, Robert Smither, and Alain Fontaine. A virtual phase CCD detector for synchrotron radiation application. *Rev. Sci. Instrum.*, 60:2586–2591, 1989.
- [79] Roy Clarke, Brian Rodricks, and Robert Smither. Virtual phase CCD X-ray detectors. *Rev. Sci. Instrum.*, 60:2280–2283, 1989.
- [80] L.E. Berman, J.B. Hastings, T. Oversluizen, and M. Woodle. Optical design and performance of the X25 hybrid wiggler beam line at the national synchrotron light source. *Rev. Sci. Instrum.*, 63:428–432, 1992.
- [81] G. Decker, J. Galayda, L. Solomon, and M. Kitamura. Magnetic measurements on insertion devices at NSLS. *Rev. Sci. Instrum.*, 60:1845, 1989.
- [82] G.O. Reynold, J.B. DeVelis, G.B. Parent, Jr., and B.J. Thompson. *The New Physical Optics Notebook: Tutorials in Fourier Optics*. SPIE Optical Engineering Press, Washington, New York, 1989.
- [83] D. Shu, B. Rodricks, J. Barraza, T. Sanchez, and T.M Kuzay. The APS X-ray undulator photon beam position monitor and tests at CHESS and NSLS. *Nucl. Inst. and Meth. A*, 319:56–62, 1992.
- [84] E.D. Johnson, Anne-Marie Fauchet, and X. Zhang. Correlation of photon beam motion with vacuum chamber cooling on the NSLS X-ray ring. *Rev. Sci. Instrum.*, 63:513–518, 1992.

- [85] D.C. Mancini and D.H. Bilderback. X-ray mirror surfaces evaluated by an X-ray topographical technique. *Nucl. Inst. and Meth.*, 208:263–272, 1983.
- [86] S. Ferrer, F. Comin, A. Santoni, V. Etgens, X. Torrelles, and V. Formoso. X-ray Fraunhofer diffraction from a mirror at grazing angles. *Nucl. Inst. and Meth. B*, 100:536–539, 1995.
- [87] R.A. Shore, B.J. Thompson, and R.E. Whitney. Diffraction by apertures illuminated with partially coherent light. *J. Opt. Soc. Am.*, 56:733–738, 1966.
- [88] E. Dufresne, M. Sutton, G.B. Stephenson, S. Brauer, I. McNulty, S.G.J. Mochrie, G. Grübel, and D.L. Abernathy. X-ray intensity fluctuation spectroscopy observations of critical dynamics in Fe₃Al. Preliminary Report, June 1995.
- [89] A.P.Y. Wong and P. Wiltzius. Dynamic light scattering with a CCD. *Rev. Sci. Instrum.*, 64:2547–2549, 1993.
- [90] K.J. McCarty and A. Wells. Measurements and simulations of X-ray quantum efficiency and energy resolution of large area CCDs between 0.3 and 10keV. *SPIE. EUV, X-ray, and Gamma-Ray Instrumentation for Astronomy III*, 1743:211–222, 1992.